Inductance Effects in Two-Dimensional Arrays of Josephson Junctions

by

Enrique Trías

B.S. , University of Miami, (1993)

Submitted to the Department of Electrical Engineering and Computer Science
in partial fulfillment of the requirements for the degree of

Master of Science

at the

MASSACHUSETTS INSTITUTE OF TECHNOLOGY

June 1995

Author .....
Department of Electrical Engineering and Computer Science
May 19, 1995

Certified by .....
Terry P. Orlando
Professor of Electrical Engineering
Thesis Supervisor

Accepted by .....
Frederic R. Morgenthaler
Chairman, Departmental Committee on Graduate Students

Inductance Effects in Two-Dimensional Arrays of Josephson Junctions

by

Enrique Trías

Submitted to the Department of Electrical Engineering and Computer Science
on May 19, 1995, in partial fulfillment of the
requirements for the degree of
Master of Science

Abstract

Measurements and numerical studies of the self-induced magnetic field effects of two-dimensional niobium Josephson junction arrays have been performed. Experiments focus on the dc electrical properties of these arrays and can be classified into four regimes: the superconducting state, flow-flow regime, the row-switching state, and novel resonance steps. We find that self-field effects can be modeled accurately with the inclusion of all the cell-to-cell interactions in the array.

In the superconducting state, an increase of the depinning current occurs when the penetration depth in the array, is of the order of one or less. There is also evidence for a destruction of commensurate vortex states in the arrays as the depinning current becomes almost independent of the applied magnetic field.

In the flux-flow regime, vortices can be modeled as massive particles due to the capacitive energy of the junctions. Self-field effects change the array flux-flow dynamics by effectively decreasing the vortex mass.

When a row is switched, all of its junctions oscillate in a coherent fashion at the temperature dependent gap frequency and the vortex-as-a-particle phenomenological picture can no longer be used. This intra-row phase-locking is due to flux quantization and appears very robust with regards to self-fields. However, phase-locking between rows, inter-row phase-locking, is reduced with strong self-fields. It was also found that row-switching ordering appears to have some symmetry even in the presence of disorder.

At a certain temperature, a transition from row-switched states to a resonant step occurs. This novel step is independent of temperature and seems to depend on both self-fields and the horizontal junctions for its dynamics.

Thesis Supervisor: Terry P. Orlando
Title: Professor of Electrical Engineering

Acknowledgments

First, I thank Dr. Herre van der Zant, whose guidance, advice, and knowledge were instrumental in the evolution of my research. I also thank Professor Terry P. Orlando for his valuable suggestions, and theoretical insights that form a large part of this thesis. I would also like to acknowledge Professor Steven Strogatz for the many useful discussions.

The samples were fabricated at IBM, MIT Lincoln Laboratory and Hypres with the help of many individuals. I specially thank Jay Sage of MIT Lincoln Laboratory for allowing me to use their mask layout design tools. Support of the National Science Foundation through a graduate fellowship and an NSF grant is gratefully acknowledged.

I am also grateful for both the contributions and friendship of my fellow graduate students. In particular, I thank Joel Phillips for providing his numerical simulation code and answering my questions. I am also indebted to Dave Carter, Amy Duwel, Mauricio Barahona, and Shinya Watanabe.

Finally, I thank my family and friends for their love and support. Special thanks must go to my closest friend, Tricia Skarzynski, for her patience and understanding. I appreciate the encouragement of my brothers Fernando and Ramón, my parents, my grandmother, and specially my grandfather who always challenged and inspired me to learn.

Contents

List of Figures

List of Tables

Chapter 1

Introduction

Josephson junctions are natural dc to ac converters. They are highly tunable oscillators that can reach frequencies in the terahertz range. Also, due to their nonlinear properties they can be used as sensitive detectors and mixers of electromagnetic waves.

Therefore a substantial effort has been spent on using Josephson junctions for oscillators, mixers, detectors, and parametric amplifiers in the millimeter and submillimeter range. However Josephson device technology has yet to produce a marketable product, mostly for the following reasons:

1. Josephson junctions need very low temperatures to operate.
2. A single junction has low voltage (mV) and power levels (nW).
3. It is difficult to impedance match a junction ($\sim 1\,\Omega$) to conventional microwave devices ($\sim 50\,\Omega$).
4. High susceptibility to electrical shocks and thermally induced processes increase the linewidths ($\sim$ MHz).

The first two factors are fundamental. They follow from the very small energy gaps in superconducting materials. The last two are technologically dependent. In the past several years, several solutions have been proposed:

1. The advent of high temperature superconductors and small-scale refrigeration

units make it feasible to design into a single small package the superconducting electronics and necessary cooling micro-machinery in the near future [15].

2. An array of Josephson junctions working coherently could raise the operational voltages (1V) and power (μW) to useful levels.

3. Arrays combined with superconducting microwave microstrips may improve impedance matching.

4. Again, arrays of Josephson junctions are less vulnerable to noise than single elements. Linewidths can be reduced to the 10 Khz range.

Therefore, coherent arrays would overcome many of the technological limitations of single junction rf devices.

In particular, two-dimensional arrays of Josephson junctions are of importance because by phase-locking, they overcome the problems of low impedances and power when using single junctions. For example, an array with N_x cells perpendicular to the current direction and N_y parallel, the phase-locking of the array implies the power delivered to a load scales with $N_y(N_x + 1)$ and, at the same time, the linewidth with $1/N_y(N_x + 1)$ [40]. Coherent emission and power levels in the microwatt range have been detected [2] in niobium arrays with 9 by 10 cells. In that paper it was suggested that the 2D array itself might provide a mechanism for phase locking through quasi-long-range interactions between its junctions.

Generally speaking, the delivered power is proportional to the critical current I_c so that the demand of high power stipulates the use of junctions with large critical currents. High critical currents, however, may destroy the internal locking mechanism in the arrays [27, 8]. In 2D arrays, the penetration depth for perpendicular applied magnetic fields, $\lambda_\perp$, is inversely proportional to I_c. A small $\lambda_\perp$ weakens the range of the vortex interactions thereby reducing the the ability of the whole array to mutually phase-lock. Clearly, an engineering compromise must be made for optimal performance.

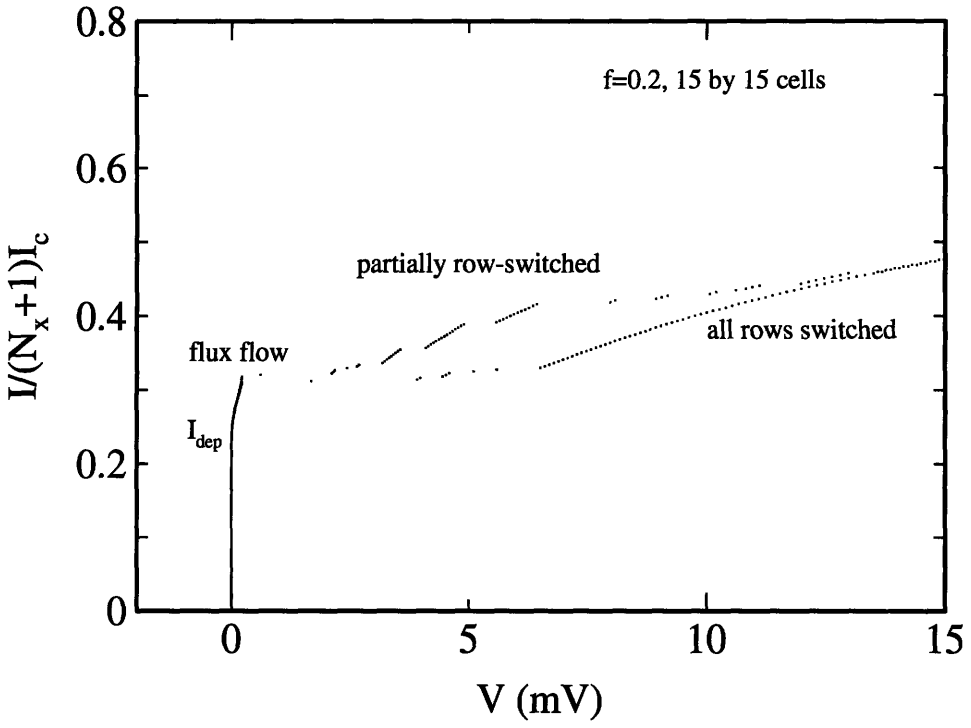

Figure 1-1: Typical I–V , indicating the depinning current, flux-flow region, partially row-switched, and fully row-switched states. The data was taken at 7.4 K with $\lambda_\perp = 0.73$ and $\beta_c = 46$.

1.1 Overview of Thesis

Although the effects of self-fields have been calculated for various array properties, there have been no detailed measurements of these effects. This thesis, presents an experimental and numerical study of the inductance effects on the electrical properties of square two-dimensional Josephson arrays. The experiments will focus on resistance and dc current-voltage (I–V) characteristics as a function of applied magnetic fields and temperature. However, the resulting richness in the dc I–V reflects the complex dynamics of the junctions. We find that these inductance effects are important in practical niobium arrays that have $\lambda_\perp \sim 1$ and that these effects can be modeled well by numerical simulation that take into account the mutual inductive interactions between every cell of the array.

A typical I–V is shown in Fig. 1-1. There are three distinct regions in the I–V : a superconducting state at zero voltage, a flux-flow region, and a row-switched region.

Chapter 2 provides the necessary background and theoretical modeling needed to describe arrays of Josephson junctions.

Chapter 3 will discuss the depinning current, I_{dep}, that indicates the onset of the flux-flow region. We will show how $\lambda_\perp$ affects the cell-to-cell energy barrier of an array. This barrier is directly related to vortex pinning. We also show that strong self-fields prevent the formation of a commensurate vortex lattice with the array.

Chapter 4 will study the flux-flow region and develop phenomenological theory of its magnetic field and temperature dependence. In this region a vortex can be viewed as a particle with an extent of $\lambda_\perp$. Its electrical energy can be interpreted as its mass and the array can be modeled as a viscous media. We find that strong self-fields reduce the equivalent viscosity of the array.

Chapter 5 will present measurements and simulations of the row-switched states as well as a novel resonance step. In this regime vortices can no longer be viewed as particles. Instead rows of junctions phase-lock and behave coherently. We find that strong self-fields affect the strength of phase-locking between rows.

Finally, Chapter 6 will provide a brief summary and future direction of research.

Chapter 2

Background

This chapter will present the basic concepts needed to understand the physics of Josephson junction arrays. It will also explain how the arrays can be modeled and simulated.

2.1 One junction preliminaries

A Josephson junction consists of two superconducting electrodes that are coupled through a thin barrier. If these superconducting electrodes are smaller than the London penetration depth, λ_L, then the supercurrent in the electrode can be described by a macroscopic wavefunction $n^{1/2}e^{i\theta}$, where n represents the total number of superconducting electrons. These superconducting electrons consist of two electrons, Cooper pairs, bounded, with an energy of 2Δ, through phonon interactions of the atomic lattice. When the barrier is thin enough, the wavefunctions of the electrodes can overlap and Cooper pair tunneling can occur [22]. It is this tunneling of the supercurrent, the Josephson effect, that forms the basis for most superconducting devices.

For insulating barriers, junction behavior can be modeled accurately by a supercurrent channel, a geometric capacitance and quasiparticle tunneling conductance. Fig. 2-1 shows the equivalent circuit of this type of Josephson junction. This RCSJ model describes the state of the junction with a phase ϕ and resulting constitutive

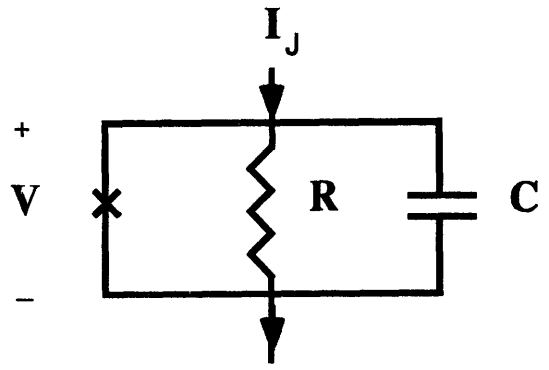

Figure 2-1: Equivalent circuit for a Josephson junction with an insulating barrier.

relations

$$I = I_c \sin\phi + \frac{V}{R_e} + C\dot{V} \tag{2.1}$$

and a voltage phase relation [22]

$$\dot{\phi} = \frac{2\pi}{\Phi_0} V. \tag{2.2}$$

Since ϕ is a measurable quantity it must be gauge invariant. Imposing this condition yields

$$\phi = \theta_1 - \theta_2 - \frac{2\pi}{\Phi_0} \int_1^2 \vec{A}(r,t) \cdot d\vec{l} \tag{2.3}$$

where the θ's are the macroscopic phases of the supercurrent wavefunction in the top and bottom electrodes of the junction and $\vec{A}(r,t)$ is the magnetic vector potential. The quantity ϕ is usually referred to as the gauge-invariant phase of the junction.

Electrons not bound as Cooper pairs are called quasiparticles. In general they can be created either by temperature or by an induced voltage. If the voltage is greater than the gap voltage, $V_g = 2\Delta/e$, then very few Cooper pairs remain bounded and the quasiparticle tunneling conductance, $1/R_e$, is described by the normal state conductance of the junction, $1/R_n$. When the voltage is lower than the gap, thermal excitations induce most of the Cooper pair breaking. In this regime $1/R_e$ is described by a temperature dependent subgap conductance $G_{sg}(T)/R_n$.

A Josephson element can also be viewed as a parametric inductor. Taking the

time derivative of Josephson channel equation

$$\frac{d}{dt}I = \frac{d}{dt}(I_c \sin\phi)\frac{d\phi}{dt} \tag{2.4}$$

and substituting in the voltage phase relation, we find

$$\frac{d}{dt}I = \frac{2\pi I_c}{\Phi_0 \cos\phi}V. \tag{2.5}$$

This is the constitutive relation of an inductor and the coefficient in front of the voltage is the reciprocal of an equivalent inductor that is dependent on the phase of the junction. The parametric inductor is equal to $L_J = L_{J0}\cos\phi$, where $L_{J0} = \Phi_0/(2\pi I_c)$.

It is common to re-normalize the above equations. From the current conservation of the RCSJ model, Eq. 2.1,

$$I = \sin\phi + V + \beta_c\dot{V} \tag{2.6}$$

and the voltage phase relation becomes

$$\dot{\phi} = V, \tag{2.7}$$

where V has been normalized by I_cR_n, I by I_c, and the overdot represents differentiation with respect to $\omega_J t$, with $\omega_J = R_n/L_{J0}$. The effective voltage dependent conductance, $G(V)$, has been set to one. This is a reasonable approximation, since most of the presented measurements are done close to the critical temperature and hence the subgap resistance is equal to the normal state resistance of the junctions. The coefficient β_c is equal to $R_nC\omega_J$ and is referred to as the Stewart-McCumber parameter. It is the ratio of the two characteristic time constants in the system and can be interpreted as a measure of the importance of the capacitance.

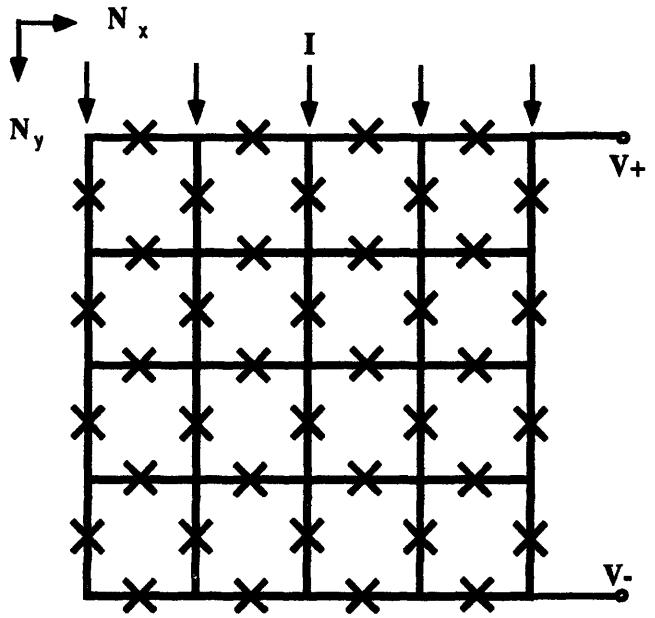

Figure 2-2: Schematic showing the circuit diagram for the square arrays.

2.2 Arrays of junctions

In this section, we will use basic concepts of network theory to derive the governing equations of a two-dimensional array of Josephson junctions. The typical schematic circuit is shown in Fig. 2-2. The elements with crosses, the branches, represent Josephson junctions, and are arranged as a two-dimensional square grid. The intersection of the junctions, the nodes, represent superconducting islands. There are N_x cells, or meshes, in the horizontal direction and N_y cells in the vertical direction.

In this thesis, we will only consider devices of this square geometry. We will also only consider arrays that have uniform current injection at every node on the top of the array and uniform current extraction at the nodes of the bottom.

Any circuit can be described topologically by its oriented graph. In turn, an oriented graph can be characterized by three types of quantities: node, mesh, and branch values. We will denote mesh quantities by a superscript m. All of our meshes are square and they contain four branches, or segments. These will be denoted by superscript b while the node variables will be denoted by a superscript n. Figure 2-3 shows the different quantities with respect to the shown coordinate system and

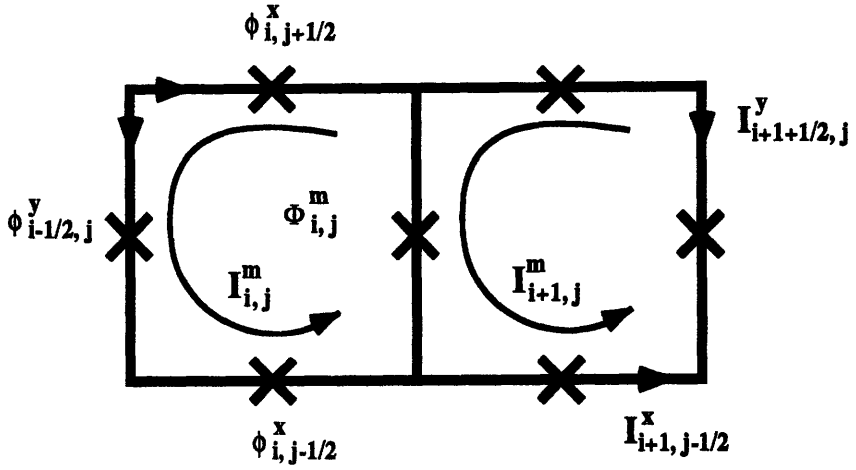

Figure 2-3: Schematic describing the different variables used to analyze the square arrays.

orientations.

These mesh, branch, and node variables are related by discrete operators M and A. It is common to characterize M as a loop sum operator and A as a node sum operator. To get a basic idea of how these operators can be used we can rewrite the traditional Kirchhoff's laws: the loop sum of branch voltages equals zero

$$MV^b = 0, \tag{2.8}$$

and the sum of branch currents at a node is zeros

$$AI^b = 0. \tag{2.9}$$

It can also be shown [6] that the mesh, node, and branch quantities are related by

$$M^T I^m = I^b \quad \text{and} \quad \mathrm{A^T V^n = V^b}. \tag{2.10}$$

In our arrays we will use mesh quantities for the flux within a cell and the mesh current. The branch quantities will be the voltage, gauge invariant phase ϕ, and branch current; the node quantities will be the node voltages and the phase, θ, of the order parameter at a superconducting electrode.

We can generalize the definition of the gauge invariant phase, Eq. 2.3,

$$\phi_{i+\frac{1}{2},j} = A^T\theta_{i,j} - \frac{2\pi}{\Phi_0}\Phi^b_{i+\frac{1}{2},j+\frac{1}{2}} \tag{2.11}$$

where Φ^b is a vector containing all the line integrals of the vector potential and is referred to as the partial flux of a branch [29].

Also, if we inject a current, I_{ext}, at a node ij, we can extend Kirchhoff's current law by noting that the sum of all the branch currents at the node will no longer be zero, but equal to the external current,

$$AI^b_{ij} = I_{ext}. \tag{2.12}$$

This equation represents the nodal boundary conditions of the array.

We can use the constitutive relations of our Josephson branch elements, the RCSJ model of Eq. 2.6 and Eq. 2.7, and the boundary conditions of the circuit, Eq. 2.12 to derive the nodal equation for the superconducting island phases. Combining them and generalizing to a vector form, we have

$$A\left[\sin\left(A^T\theta - \frac{2\pi}{\Phi_0}\Phi^b\right) + A^T\dot{\theta} - \frac{2\pi}{\Phi_0}\dot{\Phi}^b + \vec{\beta}_c\left(A^T\ddot{\theta} - \frac{2\pi}{\Phi_0}\ddot{\Phi}^b\right)\right] = \frac{I_s}{I_c}. \tag{2.13}$$

Here $\vec{\beta}_c$ is a matrix describing the capacitive coupling in the array. The diagonal entries correspond to the coupling between nearest neighbor nodes. The off-diagonal elements are the next nearest-neighbor capacitances, and so on. In this thesis, we neglect all other capacitances except nearest-neighbors and $\vec{\beta}_c$ reduces to a scalar value of the usual Stewart-McCumber parameter. The column vector I_s describes the effect of the injected external currents at every node of the array. For uniform injection at the top of the array and uniform extraction at the bottom, I_s will have I_{ext}'s at all of the top nodes where current is being injected and $-I_{ext}$'s at the bottom nodes where the current is being extracted.

Since our equations are gauge invariant we are free to choose a Coulomb gauge such that $A\Phi^b = 0$ [8]. The governing equation for θ becomes

$$A \sin\left(A^T\theta - \frac{2\pi}{\Phi_0}\Phi^b\right) + AA^T\dot{\theta} + \beta_c AA^T\ddot{\theta} = \frac{I_s}{I_c} \tag{2.14}$$

Only differences of node quantities, θ, appear in the above equation. This is a direct consequence of the non-physical nature of the phase of the supercurrent wavefunction at the electrodes. Any constant can be added to the column vector θ and result in exactly the same dynamical equation. Hence, this equation does not uniquely determine θ and mathematically, it can be shown that AA^T is singular. In order to resolve the problem, it is common in circuit analysis to ground one of the nodes. In effect, we set one of the phases to zero and treat it as our reference. Thereby, all the node phases can be determined in terms of this reference.

Though the nodal equations, Eq. 2.14, is always valid for the appropriate gauge, it is most useful when the self-induced magnetic fields can be neglected so that the flux is fully determined by the applied field. In this case the time derivatives of the flux vanish and one can choose any other convenient gauge. It is common to choose a Landau gauge such that $\vec{A}(r,t) = Hx\vec{y}$ so that Φ^b vanishes along the $\hat{x}$-direction and is equal to Hpx along the $\hat{y}$-direction.

If the effects of self-fields cannot be neglected, as is the case in Nb arrays, it is possible to develop a dynamical equation for the flux, Φ^m. Starting from Maxwell's equations and the principle of superposition, the total flux in a mesh can be decomposed into the applied flux and the flux induced by the currents flowing in the branches:

$$\Phi^m = M\Phi^b = \Phi_{ext} + \Phi_{induced}. \tag{2.15}$$

Here the induced and externally applied parts of the flux are both mesh variables. The term $M\Phi^b$ is the sum of all the partial fluxes and it is equivalent to summing the the vector potential around a loop. Therefore, $M\Phi^b$ is equal to the enclosed flux [29].

To calculate the induced fields it is necessary to determine the inductance interactions in the array. These inductance interaction can be characterized in terms of induced flux of the array mesh currents. For a circuit consisting of many closed

meshes

$$\Phi = L^m I^m, \tag{2.16}$$

where L^m is a square matrix that describes the inductive interaction between all the meshes in a circuit. Since all meshes can be decomposed into branches, it is possible to construct the induced flux by summing the contributions of each branch. Though the partial fluxes due to the branches are a useful abstractions, the real physical quantity is the flux in a mesh. Mathematically, it can be shown [29] that

$$\Phi_{induced} = M L^b I^b. \tag{2.17}$$

The M operator must sum over all of the branches that compose the mesh and L^b is a matrix describing the pair-wise inductive coupling of branches.

When dealing with any circuit, sources always present a problem because they are not easily described by a lumped element. In our Josephson arrays, it is possible to close the current sources so that an injecting branch on a top node is matched by an extracting branch on a bottom node of the array and therefore the current sources can be described as meshes. However, in the actual experiment the source loop is closed through a variety of instruments and filters. To model the precise inductance interaction between the array meshes and the source meshes would be very difficult. However, the coupling between between the source meshes and the array meshes is much weaker than the coupling between the interior array meshes and so is usually neglected.

By neglecting the inductance due to the source meshes, we can no longer use Eq. 2.16, since the source meshes have no inductance associated with them. Instead it is convenient to use the branch formulation of defined flux, Eq. 2.17. However, care must be taken to define the branch currents carefully.

We have already shown that the current injection can be expressed in terms of current conservation at the nodes. It is also possible to formulate the current injection boundary condition in terms of these mesh sources. One can think of the source

meshes at the boundaries so that

$$M^T I^m + I_s = I^b \tag{2.18}$$

Since I^m does not include the currents of the sources, it cannot fully describe the branch currents of the system. I_s is a vector that adjusts the operation of multiplying by M so that the branch currents at the edges are calculated correctly. Rewriting I_s in component form for the special case of uniform current injection, we find

$$\begin{aligned} I^s_{1,j} &= K I_{ext} \\ I^s_{i,1} &= (i-K) I_{ext} \\ I^s_{i,N_y} &= (i-K) I_{ext} \\ I^s_{N_x,j} &= ((N_x+1)-K) I_{ext} \end{aligned} \tag{2.19}$$

where I_{ext} is the uniformly injected branch current at a node, K is some arbitrary constant and i goes from 1 to N_x. In essence, the branch current along an edge will be the difference of the interior mesh current and the source current.

As noted, it is possible to construct a different I_s in terms of nodal current conservation while still utilizing Eq. 2.18. In fact, the I_s vector then has I_{ext} for every vertical junction in the array. In a two-dimensional system without horizontal cross-junctions, this is the more convenient form of expressing the boundary conditions.

We can factor out the self inductance term from the branch inductance matrix in Eq. 2.17 and normalize the current by I_c to get the defining equation for the induced flux in terms of the array parameters,

$$2\pi \frac{\Phi_{induced}}{\Phi_0} = \frac{1}{\lambda_\perp} M L^b I^b. \tag{2.20}$$

Here $\lambda_\perp = L_J/\mu_0 p$ and represents the characteristic length of which fields and currents decay in the array. As a consequence, $\lambda_\perp$ can be also be viewed as the extent of a vortex. Also, L^b is now normalized by $\mu_0 p$.

Combining Eq. 2.20 and Eq. 2.18 gives

$$\frac{1}{\lambda_\perp} L^m I^m + \frac{1}{\lambda_\perp} M L^b I_s = 2\pi \frac{\Phi^m}{\Phi_0} - 2\pi f \tag{2.21}$$

where $f = \Phi_{ext}/\Phi_0$ and L^m is the mesh inductance matrix, ML^bM^T. The parameter f is referred to as the frustration. If we neglect the induced field, the array is at the lowest energy state when all the phases are at zero. When there is an applied field, the array can no longer reach the minimum energy and it is said to be frustrated hence the name frustration. The ML^bI_s term is not due to the flux of the sources, but rather to the correct calculation of the branch current along an edge. The branch current of a mesh at the boundary of the array will be the difference of the mesh current and the source mesh, so the flux due to this branch will have a component with I_s.

To piece all of the above equations into a governing equation of the flux, we need to take the loop sum of the voltage phase relation

$$V^b = \dot{\phi}. \tag{2.22}$$

So that

$$MV^b = M(A^T\dot{\theta} - \frac{2\pi}{\Phi_0}\dot{\Phi}^b) \tag{2.23}$$

but θ is multi-valued so $MA^T\theta = 2\pi n$. Since n is just an integer, it is independent of time, and

$$MV^b = -M\dot{\Phi}^b = -\dot{\Phi}^m. \tag{2.24}$$

Multiplying Eq. 2.18 by M and substituting Eq. 2.6 for I^b

$$MM^TI^m = M\sin(A^T\theta - \frac{2\pi}{\Phi_0}\Phi^b) - \dot{\Phi}^m - \beta_c\ddot{\Phi}^m + MI_s. \tag{2.25}$$

This equation along with the governing equation for the θ's, Eq. 2.21, and the definition of the flux, Eq. 2.20, describe the dynamics of a square Josephson junction array.

However, this formulation is not very attractive from an analytical or numerical standpoint due to the complicated argument of the sine term.

These governing equations have been studied in several limiting cases. It is common to take the overdamped limit where $\beta_c = 0$. In particular, $\lambda_\perp = \infty$ has been extensively studied. From Eq. 2.15, $\Phi^m = \Phi_{ext}$ and hence there is no dynamical equation for the flux since it is fully determined by the applied flux. The only equation needed to describe the system is the nodal equation for the supercurrent phase on the islands, Eq. 2.14. We can further simplify the problem by choosing a more convenient gauge such as the Landau gauge.

For finite $\lambda_\perp$ it is also possible to describe the system in terms of the gauge invariant phase [25] by noting that

$$\begin{aligned} M\phi &= MA^T\theta - M(\frac{2\pi}{\Phi_0}\Phi^b) \\ &= 2\pi n - \frac{2\pi}{\Phi_0}\Phi^m \end{aligned} \tag{2.26}$$

This is the famous flux quantization condition of a loop of Josephson junctions. Since the only measurable quantities depend on $\sin\phi$ and $\dot{\phi}$ one can try to redefine the phases such that the $2\pi n$ is absorbed in the equation. A solution for a new set of phases, ψ, such that $M\psi = M\phi - 2\pi n$ would effectively absorb the constant $2\pi n$ values. Mathematically, a set ψ's can be found if there is at least one junction at the boundary. From this fact, it follows that the dynamical equations are Φ_0 periodic and we can set n to zero without loss of generality. Physically, if there was not a junction at the boundary, there would be a superconducting loop and the enclosed flux would still be quantized but the dynamics would no longer be Φ_0 periodic. Instead, the number of enclosed flux would become a topological constraint on the system.

To get the governing equations of the gauge invariant phase, we make use of the mesh boundary condition, Eq. 2.18, and the RCSJ model. We find that

$$M^T I^m = \sin\phi + \dot{\phi} + \beta_c\ddot{\phi} - \frac{I_s}{I_c} \tag{2.27}$$

and from the definition of the flux, Eq. 2.21, and flux quantization, Eq. 2.26,

$$-\frac{1}{\lambda_\perp}(L^m I^m + M L^b I_s) = M\phi + 2\pi f. \tag{2.28}$$

In constructing the I_s vector for the mesh boundary condition and uniform current injection, Eqs. 2.19, we need to choose a value for the arbitrary constant K. If we use the self-consistent formulation with the full inductance matrix, then the dynamics are independent of this reference value. However, if we truncate the inductance matrix, then it is important for the external current meshes to be antisymmetric so that the induced fields of the external meshes have a maximum at the edges and decay toward the center, as in any superconducting material. In effect, we choose the K such that the center source mesh is equal to zero.

2.3 Continuum limit

Having described the formalism needed to model Josephson circuits, we can now derive continuum approximations in order to more fully understands the physics of these square arrays. We will find that in certain regimes the dynamics of the two-dimensional circuits can described in terms of flux transport and that the basic unit is a Josephson array vortex.

2.3.1 Continuum operators

First we will determine what the operators A and M look like for a continuous approximation. A discrete operator with a finite basis is analogous to a continuous operator plus boundary conditions. For instance, a discrete gradient operator has built-in Neumann or Dirichlet boundary equations that would have to be specified separately in a continuous approach.

We will treat the boundaries in the following section. For now, we ignore them in order to get the equivalent continuous operator of A and M.

For some node ij, the node sum operator, A, can be written in component form

as

$$AI^b_{i,j} = I^b_{i-\frac{1}{2},j} - I^b_{i+\frac{1}{2},j} + I^b_{i,j-\frac{1}{2}} - I^b_{i,j+\frac{1}{2}}. \tag{2.29}$$

All our equations, including the definition of $\lambda_\perp$ are already normalized to the lattice constant p so we can change the coordinates to continuous variable by using $\Delta x = 1/N_x$ and $\Delta y = 1/N_y$ and therefore approximate the discrete operator by

$$AI^b_{ij} \approx I_y(y) - I_y(y + \Delta y) + I_x(x) - I_x(x + \Delta x). \tag{2.30}$$

In the continuum limit, we get

$$AI^b_{ij} \approx -\Delta y \frac{dI_y}{dy} - \Delta x \frac{dI_x}{dx}. \tag{2.31}$$

If we let $N_x = N_y = N$ then

$$AI^b_{ij} \approx -\frac{1}{N} \nabla \cdot I \tag{2.32}$$

where I is a vector describing the current flow in $\hat{x}$ and $\hat{y}$ direction.

Similarly

$$A^T \theta^n \approx -\frac{1}{N} \nabla \theta(x, y) \tag{2.33}$$

where θ is a scalar function describes the phase of the order parameter at some coordinate (x, y). Hence the combination $AA^T\theta$ is simply the Laplacian of θ.

A similar analysis can be made for the loop sum operator M:

$$M\phi \approx \frac{1}{N} \nabla \times \phi \tag{2.34}$$

$$M^T I^m \approx \frac{1}{N} \nabla \times I \tag{2.35}$$

where

$$\phi = \begin{pmatrix} \phi^x(x, y) \\ \phi^y(x, y) \\ 0 \end{pmatrix} \quad \text{and} \quad \mathrm{I} = \begin{pmatrix} 0 \\ 0 \\ I^m(x, y) \end{pmatrix} \tag{2.36}$$

and the combinations of the M operator are

$$M^T M\phi \approx \frac{1}{N^2}\nabla \times \nabla \times \phi \tag{2.37}$$

$$MM^T I^m \approx \frac{1}{N^2}\nabla^2 I^m. \tag{2.38}$$

The continuous variable I^m describes the circulating current in the array, while ϕ describes the phase differences along the $\hat{x}$ and $\hat{y}$ directions.

2.3.2 The equations

The discrete equations contain an inductance matrix that is difficult to work with in a continuous limit. Therefore, as a first approximation we will diagonalize the mesh inductance matrix. This is equivalent to studying only self-induced fields because the flux in a mesh is fully characterized by its circulating current. From Eq. 2.15 and the flux quantization condition

$$I^m = -\lambda_\perp(M\phi + 2\pi f) \tag{2.39}$$

and substituting into the governing equation of the gauge invariant phase, Eq. 2.27, we can evaluate the discrete expression that describes the array when only self-inductances are considered

$$-\lambda_\perp(M^T M\phi + M^T(2\pi f)) = \sin\phi + \dot{\phi} + \beta_c\ddot{\phi}. \tag{2.40}$$

The term $M^T(2\pi f)$ is zero everywhere but at the boundaries, so that the continuous equation becomes [21]

$$-\frac{\lambda_\perp}{N^2}\nabla \times \nabla \times \phi = \sin\phi + \dot{\phi} + \beta_c\ddot{\phi} \tag{2.41}$$

subject to the boundary conditions

$$\nabla \times \phi|_{bound} = 2\pi f \tag{2.42}$$

In this self-inductance limit it is customary to use $\Lambda^2 = \lambda_\perp$. To derive these equations we have ignored the external current drive. They can be included, as in the discrete case, by Neumann boundary conditions at the edges.

It is constructive to show that the continuous equation reduces in the one dimensional limit to the Sine-Gordon equation, SGE, that describes the dynamics of a long one-dimensional Josephson junction. Let

$$\phi = \begin{pmatrix} 0 \\ \phi^y(x) \\ 0 \end{pmatrix}. \tag{2.43}$$

In a one dimensional limit, the phase will only depend on x and time, and will be directed in the $\hat{y}$-direction.

Therefore, $-\nabla \times \nabla \times \phi = \partial_{xx}\phi$ and Eq. 2.41 reduces to

$$\left(\frac{\Lambda}{N}\right)^2 \frac{\partial^2}{\partial x^2}\phi = \sin\phi + \dot{\phi} + \beta_c\ddot{\phi} \tag{2.44}$$

and at the boundary

$$\frac{\partial}{\partial x}\phi = 2\pi f \tag{2.45}$$

which with the appropriate time scale is the continuous SGE. In contrast to the well studied SGE, the two dimensional generalization of the continuous mesh equation, has not been studied in any detail.

It is also possible to derive the equation for the vector potential in a bulk superconductor and the second London equation. In the continuum limit the phase invariant phase becomes

$$\phi = -\frac{1}{N}\nabla\theta - \frac{2\pi}{\Phi_0}A(r,t) \tag{2.46}$$

and substituting into the continuous governing equation, Eq. 2.41, while linearizing the $\sin\phi$ term and at steady state

$$\lambda\nabla \times \nabla \times A(r,t) \;=\; \phi$$

$$
\begin{aligned}
&= -\nabla\theta - \frac{2\pi}{\Phi_0}A(r,t) \\
\nabla \times B &= \mu_0 J_s. \qquad (2.47)
\end{aligned}
$$

J_s is the usual supercurrent equation with an appropriately scaled penetration depth. It follows that ϕ is analogous to the current in a bulk material and I^m is analogous to B. Note that the equation is only defined in the x-y plane. This is equivalent to considering a cylinder of infinite dimension in the $\hat{z}$-direction, confirming that diagonalizing the mesh inductance matrix is equivalent to studying self-fields for cylindrical geometries where magnetic fields extend to infinity in the $\hat{z}$-direction.

Since the second London equation allows singular solutions of circulating currents, called vortices [22], it is natural to consider if it useful to use the classical vortex picture when describing the dynamics of the discrete array. Though it should be possible to study the discrete system directly, the nonlinearity and high degree of coupling make it difficult. Instead, we find through phenomenological models that in the superconducting state, and in the flux-flow regime vortices are a convenient way of describing the dynamics. However, in the row-switched regime the vortex picture breaks down and the array dynamics can no longer be viewed in terms of vortices and must instead be viewed as coherent oscillations of junctions.

From the London equations we can derive the mathematical structure of these vortices. If we restrict the current to flow only in the x-y plane and allow the vector potential to vary in all of space, then we recover Pearl's thin film result for the structure of a two dimensional vortex. The solution is fundamentally different from the three dimensional bulk limit. In both, the current falls off as $1/r$ up to a distance $\lambda_\perp$. Subsequently, the two dimensional vortex has a current drop-off of $1/r^2$ [24] while in the bulk material it falls off exponentially [22]. Therefore two-dimensional vortices are expected to behave differently from their bulk three-dimensional counterparts [25].

It is also possible to investigate the nature Josephson array vortices directly from the Josephson arrays equations. For the $\lambda_\perp = \infty$ limit, mathematically it is more convenient to begin with mesh formalism instead of the nodal equations. If we used

the nodal equations, we would get terms involving the divergence of $\sin\phi$, which is not easily treated analytically. Instead, we can multiply M by the mesh equation, Eq. 2.27, and recall that $M\phi$ is a constant related to the applied flux. From there, one can easily derive the Poison equation that determines I^m. Together with the governing equation of the gauge invariant phase difference, Eq. 2.27, and the flux quantization, Eq. 2.26, the system is fully determined.

However, we can still use the continuous nodal formulation to verify the structure of Josephson array vortex. We will analyze the simplest case of an infinite array at steady state and $f = 0$. The equation is

$$\nabla \cdot \sin(\nabla\theta) = 0. \tag{2.48}$$

This equation describes the current distribution in the array. Because we know the current will fall to zero far from the vortex core we can linearize the sine term. Hence

$$\nabla^2\theta = 0. \tag{2.49}$$

This is Laplace's equation which is easily solved. By symmetry considerations θ depends on the azimuthal angle and is independent of the distance from the origin. The solution is the so called arctan approximation, $\theta = \tan^{-1}(y - y_0/x - x_0)$. We can get the approximate current distribution by noting that $I/I_c \approx \nabla\theta$, and hence the current has a $1/r$ dependence. Of course this result is only asymptotically correct at distances far away from the vortex core.

As expected from the above arguments, the vortex in the array does have a $1/r$ current dependence at distances smaller than $\lambda_\perp$. Similarly from the above analysis, if we take into account self-inductances we recover the result for a vortex in a three-dimensional bulk material and in the limit the magnetic field is dependent on (x, y, z) but the current is confined to the (x, y) plane, we recover Pearl's thin film result of an algebraic current drop-off. Therefore, a Josephson array supports vortex solutions of the same type as in two-dimensional thin films.

We have shown that governing equations of a square Josephson array can be

written in a continuous approximation. This formulation allows for singular vortex solutions. It will be shown in later chapters, that in certain regimes the dynamics of the discrete arrays can also be described in terms of propagating vortices.

2.4 Details of dynamic simulations

To compare the measurements with the derived governing equation for the Josephson array, we performed numerical integration of equations of the array in two regimes: $\lambda_\perp = \infty$ and $\lambda_\perp < 5$. In the former limit we use the nodal formulation described by Eq. 2.14 and a Landau gauge to describe the applied magnetic field. Using this nodal formulation, we can write the set of equations in a standard format that can be integrated using commercial numerical packages. The system of equation is thus

$$\begin{aligned} \dot{V} &= \frac{1}{\beta_c}\left(AA^{T^{-1}}(I_{ext} - A\sin(A^T\theta - \frac{2\pi}{\Phi_0}\Phi^b) - V\right) \\ \dot{\phi} &= V. \end{aligned} \tag{2.50}$$

We could have used the mesh formalism of Eq. 2.27 and Eq. 2.28. However, because they are no longer coupled through the mesh currents it is impossible to write them as a standard system of first order ODE's. The mesh formalism in the $\lambda_\perp = \infty$ case is more useful for analytical work than for numerical integration.

Numerically speaking, there are two issues when dealing with integrating systems of equations. One is evaluating the right hand side, RHS, while the other is the integrating algorithm to use. For the nodal formalism we evaluate the RHS, by factoring AA^T into its LU components and backsolving. This is an $O(n^2)$, where n is the number of nodes minus one. Depending on the computer system speed and size of the array, the cost may be prohibitive. In this case one can take advantage of the sparsity of AA^T. In particular AA^T represents a discrete two-dimensional Laplacian operator and there are many efficient numerical schemes that deal with optimally solving this problem [4].

For the finite $\lambda_\perp$ we can use the mesh formalism described by Eq. 2.27 and Eq. 2.28,

since we can solve for the mesh currents. A standard system of first order ODE's is easily constructed

$$\begin{aligned} \dot{V} &= \frac{1}{\beta_c}(M^T L^m - \sin\phi - V - I_s) \\ \dot{\phi} &= V \end{aligned} \tag{2.51}$$

$$L^m I^m = -\lambda_\perp(M\phi + 2\pi f) - ML^b I_s \tag{2.52}$$

For small arrays the above system of equations can be solved by performing an LU factorization of L^m and backsubstituting to solve for I^m at each evaluation of of the RHS. For n total of meshes, this is an $O(n^2)$ operation. For an array of size N, this is equivalent to an $O(N^4)$ problem. Hence for larger arrays performing the backsubstitution is prohibitively expensive. In this case, one can exploit the inherent symmetry of L^m. By analyzing the structure of the product $L^m I^m$, it can be derived that it represents a two dimensional convolution. It is possible to use an FFT algorithm to perform this dense product and reduce its cost from $O(n^2)$ to $O(n \log_2 n)$ [25]. However, in this thesis all the simulations were performed for arrays less than $N = 15$; hence no optimization was necessary.

The second numerical issue is the integration algorithm to use. In general, there are two types: explicit and implicit methods. Explicit integrators solve for new time steps in terms of the previous calculated time step. Therefore, the new time step is explicitly related to previous time steps. In implicit algorithms, the next time step to be evaluated is expressed in terms the both the previous time steps and the new step. Hence implicit algorithm require solving a system of equations, whereas explicit algorithms only require evaluating a RHS. Which method to use depends on the behavior of the solution and the required step size.

If the solution is well behaved and smooth, then an explicit integrator is most efficient. However, if the solution has very fast transients an explicit integrator can be used only if it has a small step size so that it can track the correct solution. In this case, the system is said to be stiff. If the problem is very stiff, the small time steps needed might be prohibitively expensive and an implicit scheme must used. In

general, the implicit schemes have better stability properties and can keep track of the solution even if the time step is larger than the transients.

From a qualitative view of the system of equations, a large RHS will occur when β_c is small. Therefore, a small β_c is more likely to make the problem stiff. Also, the RHS has an L_m^{-1} dependence. This can cause problems if the eigenvalues of L_m^{-1} are large. From forming several inductance matrices, we can empirically deduce that the maximum eigenvalue is proportional to $1/L_0$. Therefore, a small self-inductance produces large eigenvalues and makes the problem stiffer so that we are forced to use an implicit integrator if we want to take reasonably large step sizes. The self inductance, $1/L_0$, is of the oder of $\lambda_\perp$ and our arrays have a $\beta_c > 5$ and $\lambda_\perp < 3$ so that stiffness is not an issue. Hence it is advantageous to use an explicit method. In the simulations a variety of explicit integrators were used, including different orders of Runge-Kutta and a code that uses a variable order ADAMS formulas. In each case, the integration error in each step has been kept at less that 10^{-4} in the normalized units.

With our system of equations we can turn to Matlab [33] or other numerical packages and perform a simulation. The technical details of calculating the inductance matrix are described elsewhere [25, 28]. The goal is to reproduce a measured current voltage characteristic as closely as possible. For the finite $\lambda_\perp$ our procedure is as follows

1. Guess ϕ and v.
2. Calculate I_m using Eq. 2.52.
3. Integrate Eqs. 2.52 for a predefined time interval.
4. Throw away transient (first α time steps).
5. Average the rest of the solution to get a dc voltage.
6. Increment I_{ext}.
7. Go back to step 2.

In every cycle we are perturbing the problem slightly by increasing I_{ext}. By sweeping the current, we are able to calculate the *I–V* characteristic of the array. The procedure is similar for the $\lambda_\perp = \infty$ set of equations.

The current usually ranges from 0 to 1.2 by increments of 0.01 in units of I_c and the simulation is allowed to integrate for predefined time interval at each I_{ext} value. To calculate a dc value, the resulting voltage after discarding the transients is averaged over a fixed time. To reduce the complexity of the time averaging, the integration time steps remain constant.

The length of the both the transient and averaging times is difficult to gauge. We know that β_c is the ratio of the characteristic times of the system. Since our time is already normalized by ω_J, β_c provides a useful time scale. From qualitative experiments a time of $10\beta_c$ for the transients and $25\beta_c$ for the averaging seems to provide good results. However, if the array is in the normal state or a row-switched state, then the solution is periodic with a period that is inversely proportional to the applied current. Hence, in theory, the averaging time should decrease the higher one is in the *I–V* , but in practice it is difficult to determine when the array is in a periodic solution.

In this thesis we will compare measurements of fabricated Nb arrays with the simulations. The simulations will allow us to more fully characterize the dynamics of these devices. Also, since we use a full mutual inductance matrix it allows us to quantify the effects of induced fields on the dc properties of the arrays.

Chapter 3

The Superconducting State

In this chapter we study how self-induced fields affect the superconducting state of a Josephson arrays. We will study the pinning of vortices and the formation of commensurate states as a function of $\lambda_\perp$ using both experiments and simulations.

3.1 Experimental Landscape

A total of five different arrays were fabricated using a Nb-Al_2O_x-Nb trilayer process with varying critical current densities, J_c. Fig. 3-1 shows the physical layout of the arrays. The bottom electrode is represented by the hatched islands, the black squares represent both the vias and the etched counterelectrode of the trilayer that form the Josephson junction. These are connected by a metallic layer shown by the unhatched islands. We only consider square arrays where every inner island is connected to four neighbors. All the arrays have junctions arranged in a $N_x \times N_y$ square matrix, where N_x is the number of cells in the perpendicular direction of the injected current and N_y is the number of cells in the same direction as the injected current. In this chapter arrays with $N_x = N_y = N = 15$ with a cell spacing of p were studied. Array 1 was fabricated at Hypres [16] with $J_c = 1000\,\mathrm{A/cm^2}$. Arrays 2-5 were fabricated at MIT Lincoln Laboratory using a DSNAP process [3]. In this paper we report detailed measurements of array 1.

Array 1 consists of $3{\times}3\,\mu\mathrm{m}^2$ junctions with $p = 16.5\,\mu\mathrm{m}$. By injecting the current

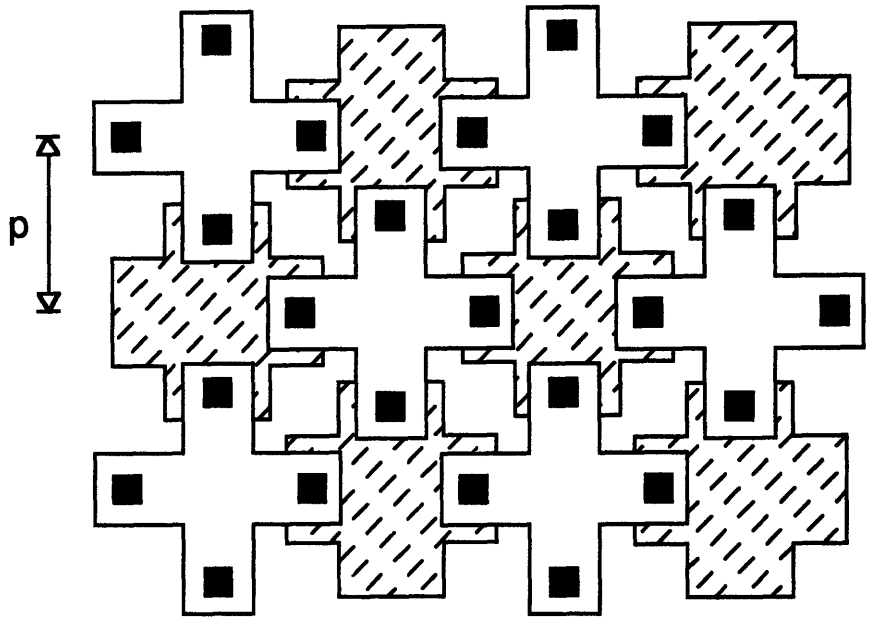

Figure 3-1: Geometry of two-dimensional Josephson-junction array.

through resistors of $0.5\,\Omega$ connected on each island of the top and bottom of the array, uniformity in bias current was achieved. The voltage was measured between the rightmost islands of the top and bottom row.

The junction normal state resistance, R_n, is determined from the measured array resistance, $R_{n,array}$, at $T \approx 8\,\mathrm{K}$ by the relation $R_n = R_{n,array}(N_x + 1)/N_y$. At $T = 0\,\mathrm{K}$ the $I_c R_n$ is equal to $1.9\,\mathrm{mV}$, so that the junction critical current, I_c, can be estimated. For array 1, the junction capacitance, C, is $300\,\mathrm{fF}$ and $R_{n,array} = 19.3\,\Omega$ so that R_n is calculated to be $20.6\,\Omega$. From the above values we can estimate $\beta_c = 2\pi R_n^2 C I_c/\Phi_0$ and the dimensionless penetration depth $\lambda_\perp = \Phi_0/2\pi\mu_0 p I_c$. Furthermore, by varying the temperature of the sample we can vary a junction's i_c and hence change its β_c and $\lambda_\perp$ by up to a factor 5 in a controlled way. For array 1, $6 < \beta_c < 30$ and $0.2 < \lambda_\perp < 1$.

We define I_{dep} as the current where there first occurs a nonzero voltage across the

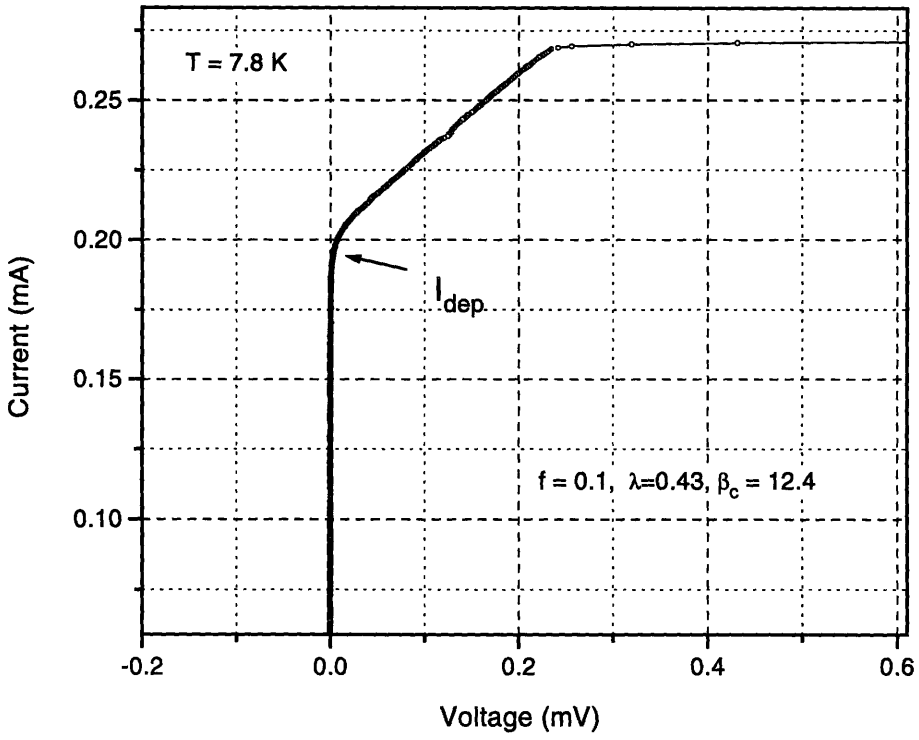

Figure 3-2: Typical I–V showing how the depinning current is defined.

array as shown in Fig. 3-2.

3.2 Depinning current vs. $\lambda_\perp$

In this section we present a study of the dependence of the depinning current, I_{dep}, with $\lambda_\perp$. An externally applied magnetic field, H_0, was used to inject vortices in the array. This field is characterized by the frustration $f = \mu_0 H p^2/\Phi_0$ which measures the fraction of flux quanta, Φ_0, in a cell. Fig. 3-3 shows I_{dep} for $f = 0.2$ for the various samples of 15×15 cells at various temperatures. We see that the depinning current increases strongly as $\lambda_\perp$ becomes less than 1.

To calculate a depinning current the motion of single vortex is modeled as a damped massive particle moving through a sinusoidal potential of amplitude $\Delta E/2$, with ΔE representing the intrinsic cell-to-cell energy barrier of the array. This equation of motion maps onto the same form as the RCSJ model of a single junction [30, 37] with a critical depinning current $I_{dep} = (\Delta E/2E_J)I_c$, where $E_J = \Phi_0 I_c/2\pi$ is

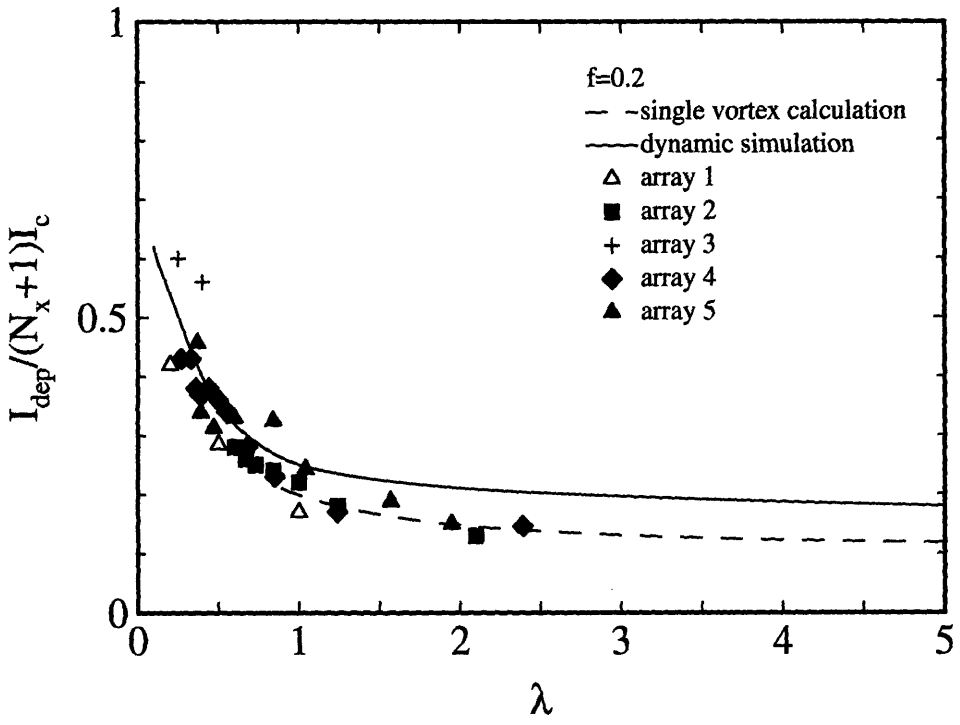

Figure 3-3: Depinning current as a function $\lambda_\perp$.

the Josephson energy.

From the Josephson relations one can derive the potential energy of a junction $E_J \cos(1-\phi)$. This is the free energy of the insulating barrier and it is analogous to the potential energy of a pendulum.

In the limit where $\lambda_\perp$ is larger than the array size, this barrier to vortex motion was first calculated by Lobb, Abraham, and Tinkham, (LAT) [20]. They considered the total static Josephson energy,

$$E/E_J = \sum(1-\cos\phi), \tag{3.1}$$

of the array when a single vortex is in the middle of a cell and when the vortex is on top of a junction. Since these represent respectively the minimum and maximum energy configurations, their difference is a barrier, ΔE, to vortex motion. The LAT result of $\Delta E = 0.2E_J$ yields an expected $I_{dep} = 0.1I_c$ which has been measured by various groups [30, 37] and our data does indeed approach $I_{dep} = 0.1I_c$ as $\lambda_\perp \gg 1$.

There is also a magnetic energy associated with the self-field effects generated by

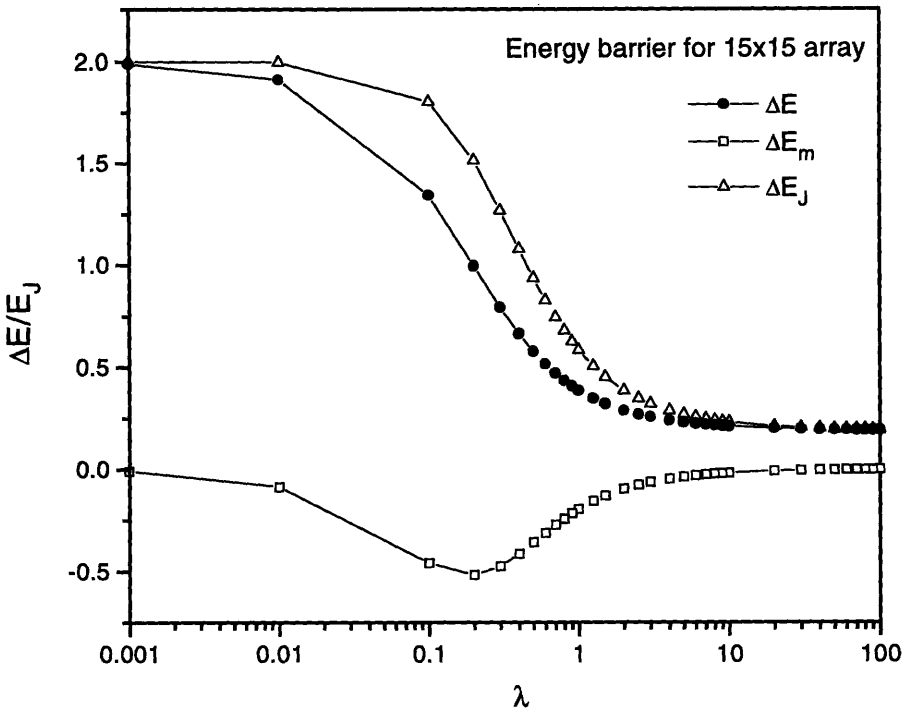

Figure 3-4: ΔE as a function $\lambda_\perp$ for a 15 × 15 array. Circles depict the total energy barrier, squares show the magnetic contribution to the barrier, while the triangles represent the Josephson contribution.

the circulating currents of a vortex. Phillips *et al.* have shown that as $\lambda_\perp$ decreases this stored magnetic energy,

$$E_m/E_J = \frac{1}{2\lambda_\perp} I^{m^T} L^m I^m, \tag{3.2}$$

must be included. Fig. 3-4 shows the energy barrier as a function of $\lambda_\perp$ with the different contributions from the magnetic fields and the Josephson energy explicitly shown.

In contrast to the Josephson energy, a vortex has a smaller magnetic field energy when it is on top of a junction than when it is in the middle of a cell. This is a direct consequence of the current distributions in a discrete array. When a vortex is in the middle of the cell, there are four junctions that carry the same current. When it is on top of the a junction, that junction carries no current and the four nearest junctions are farther away, hence they carry less current and the overall magnetic field energy

is lower. Also, it can be qualitatively inferred from the graph that the magnetic field energy can be neglected when $\lambda_\perp$ is of the order of the array size.

The value of $E/E_J = 2$ as $\lambda_\perp$ approaches to zero is easily understood in terms of the localization of the vortex. As the vortex decreases in size, the total energy of the array when the vortex is in the middle of the cell is zero. In essence, the vortex disappears. On the other hand, when the vortex is on top of a junction the phase difference of the junction is always π. Even though there are no currents in the array in the $\lambda_\perp = 0$ limit, the junctions will maintain the phase difference and the energy of the array will not be zero. In this respect, it is the localization of the vortex in the discrete array that plays a major role in the determination of the energy barrier. The inclusion of the magnetic energy provides an important correction.

The important conclusion from analyzing Fig. 3-4 is that a smaller $\lambda_\perp$, strong self-fields, produces an increase in ΔE [25] and hence I_{dep} also increases.

The dashed line of Fig. 3-3 represents the depinning current associated with ΔE calculated for a single vortex in a 127×127 array taking into account both the Josephson and magnetic field energy. This static calculation asymptotically approaches the LAT value of $0.1I_c$.

Although the static calculation appears to fit to our measurements, it assumes that there is only one vortex in the system. Therefore, to more closely approach our physical situation, we performed dynamical simulations that included all the mutual inductances [26] with $f = 0.2$ on an array of 15×15 and calculated I–V curves. (The mutual inductance matrix is calculated numerically from the actual sample layout.) With such a high applied field many vortices are present so that both vortex interactions and edge effects are included in our dynamic simulations. We extracted the depinning current using the same experimental criteria outlined in Section II. The result is shown in the solid line of Fig. 3-3 that lies above the dashed line. LAT showed that ΔE is inversely dependent on N. Since the dynamic simulation was made for a smaller array than the static calculation, one would expect the solid line of Fig. 3-3 to be lower than the dashed line. However, if the size of the array is small enough, depinning from the edge can affect the overall depinning current. This may account

for the fact that I_{dep} is a third larger than the static calculation even at $\lambda_\perp = 5$. To verify if the edge effects could cause an increase in I_{dep}, a dynamic simulation was performed for $\lambda_\perp = 5$ for a 15×15 array and a 31×31 array. As seen in Fig. 3-3, for the smaller array I_{dep}/I_c equals 0.17. For the larger array I_{dep}/I_c equals 0.13, so that edge effects account for most of the increase in I_{dep} and are thus more pronounced than vortex interactions for arrays 15×15 or smaller at $f = 0.2$. This is in direct contrast to the static calculations. When $\lambda_\perp > 1$, the energy barrier is smaller as the array decreases in size.

The measured data follows the same trend as the dynamic simulation except the values tend to be lower. This may be due to thermal noise introduced by the finite temperature. The simulations do not take thermal noise into account. Since these arrays have such large β_c's, thermal noise may easily cause vortices to depin at lower currents.

3.3 Depinning current vs. frustration

In Fig. 3-5 we show measurements of the depinning current versus frustration for array 1 with various values of $\lambda_\perp$. The data was taken at temperatures of 4.2 K, 7.9 K and 8.6 K. By increasing the temperature the individual junction's critical current decreases and hence change $\lambda_\perp$ from $0.2, 0.5$ to 1 respectively. We verified that the depinning current is symmetric about $f = 1/2$ and periodic with $f = 1$ as expected. The measured data has a large peak at $f = 0$ followed by a rapid decay to a saturation level. This saturation level contains a substructure when $\lambda_\perp > 0.2$ with clear peaks at $f = 1/2$, as well as some smaller peaks at $f = 1/4$ and $f = 1/3$. This substructure tends to be washed out as $\lambda_\perp$ decreases and disappears when $\lambda_\perp = 0.2$. Note also that the saturation level increases as $\lambda_\perp$ decreases.

For comparison a simulation taking into account all the mutual inductance interactions was performed for the same parameters of array 1. The trends are strikingly similar. The same substructure is seen and the saturation level increases as $\lambda_\perp$ becomes smaller, although the levels are lower in the measured data. Similar trends are

reported in recent numerical simulations in which the inductance matrix is calculated analytically [28].

We first focus on the $f = 0$ region of Fig. 3-5. For large $\lambda_\perp$ we expect the array to behave coherently as a single junction with a critical current scaled by $(N+1)$ and an R_n which is N times smaller. In this state every junction in the array is oscillating with the same frequency. So as expected, the superconducting region in the simulations extends to $I_{dep} = (N+1)I_c$. It has been shown that the in-phase solution of the junctions is neutrally stable so that the junctions may not necessarily be in-phase [40]. However, experimental measurements of the power emitted by junction arrays always indicate some degree of phase-locking. It is probable that an applied magnetic field, or the effects of $\lambda_\perp < N$ may provide a mechanism for weak phase locking in the array.

As $\lambda_\perp$ decreases more current begins to flow around the edges inducing a locally larger magnetic field. Since $f = 0$, only pairs of opposite-signed vortices may be induced by the current. These pinned vortices can lower the depinning current from the $\lambda_\perp = \infty$ case. Though vortex-antivortex creation is possible, it is more likely that the reduction of the depinning current is due to the nonuniformity of the current distribution in the array. It is known that inclusion of all the mutual interactions reduces this screening effect, however the junctions on the edges of the array would still have twice the current as the junctions in the middle, even for small values of $\lambda_\perp$. These outer junctions will switch to a voltage state at a lower value of the driving current than when the current is uniformly distributed for $\lambda_\perp = \infty$.

In both the simulations and the measurements we see the trend that the $f = 0$ peak decreases with decreasing $\lambda_\perp$. However, the measured levels are lower. This may be explained by two reasons. First, a truly zero applied field state is very difficult to obtain experimentally and secondly, thermal noise might depin the vortices prematurely.

The substructure is a result of a vortex superlattice forming a commensurate state with the underlying geometry of the array. These occur at values of $f = p/q$, where p and q are small prime integers. For instance, at $f = 1/2$ it is known that the ground

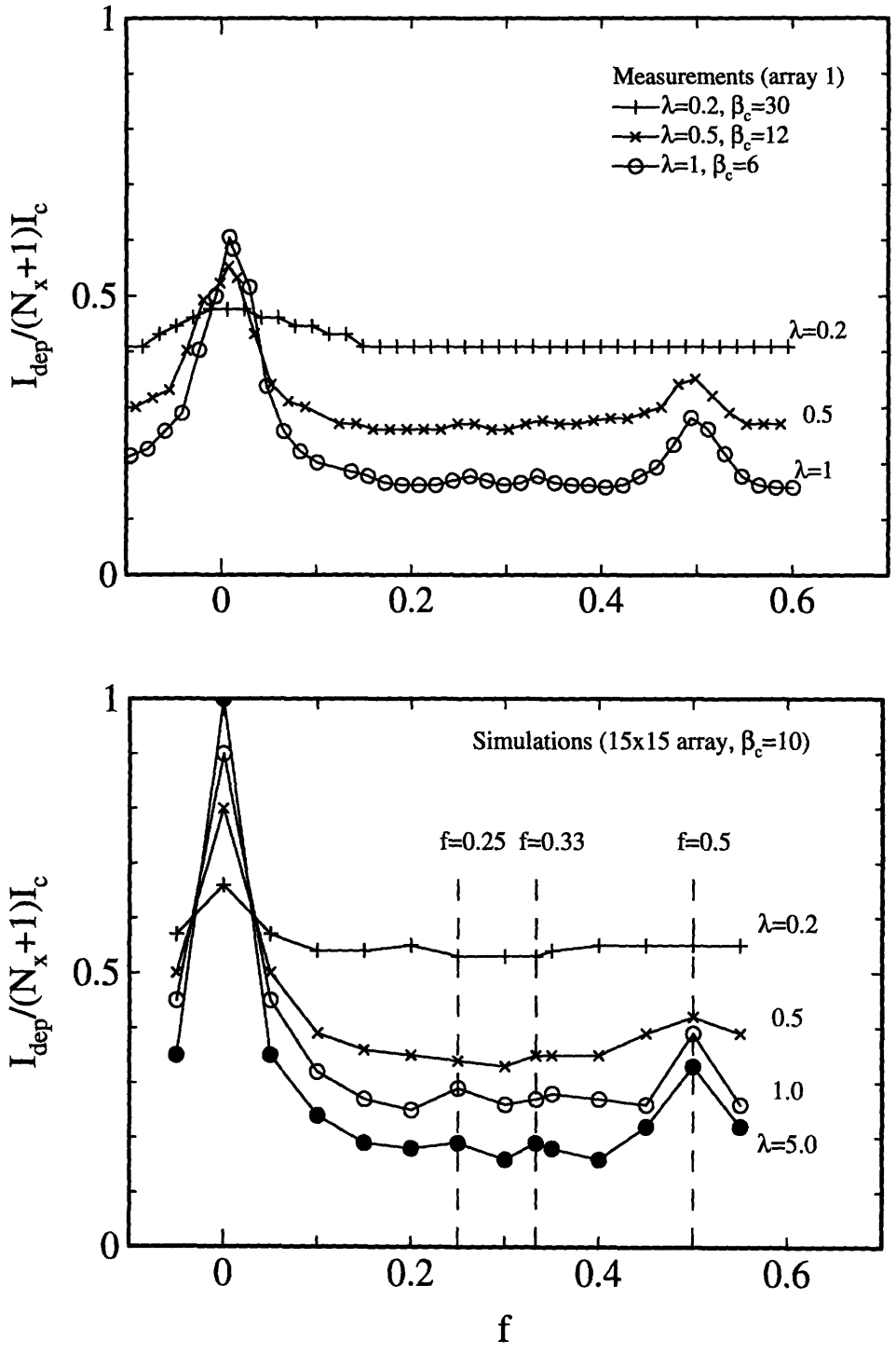

Figure 3-5: Top: Measured depinning current as a function applied field. Bottom: Simulated depinning current as a function applied field.

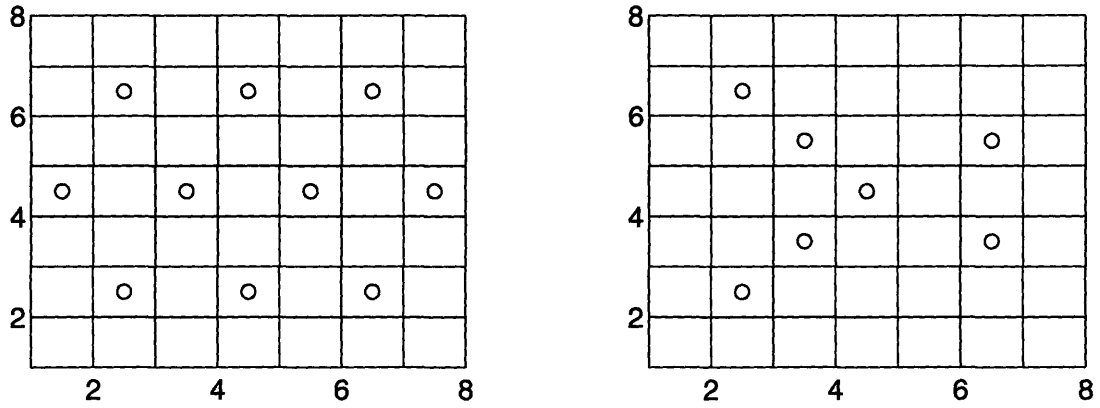

Figure 3-6: Dynamic formation of a vortex lattice for $\lambda_\perp = 0.3$ on the right and $\lambda_\perp = 5$ on the left with $f = 0.25$. This vortex distribution snapshot was taking just before the depinning current.

state for $\lambda_\perp = \infty$ is a checkered board pattern and that $I_{dep} = 0.41 I_c$ [30]. The large I_{dep} is a result of the depinning of the larger vortex ground state which requires more energy than the depinning of a single vortex. The peaks at those special values of f represent the formation of commensurate ground states which require higher energy to depin.

Fig. 3-6 shows the vortex configuration that is formed in dynamic simulations just before depinning for two different values of $\lambda_\perp$ at $f = 0.25$. The vortex location is defined in terms of the loop sum of the gauge invariant phases as in [27, 35]. The graph on the right shows a commensurate state at $f = 0.25$ for $\lambda_\perp = 5$. This is not the ground state for this magnetic field value, but a meta-stable state with a higher energy. In the dynamics simulations, it is difficult to form the ground state at small values of f since there are many other neighboring states that the array can converge to. Nonetheless, the graphs show that for larger $\lambda_\perp$ the vortices are uniformly distributed in the array and form a superlattice, while for smaller values of $\lambda_\perp$ the vortex lattice is no longer commensurate. As $\lambda_\perp$ decreases vortices become more screened and hence their interaction is diminished. It is likely that these ground state superlattices can no longer form and hence the substructures disappears.

3.4 Conclusions

A study of the effect of self-induced fields on the depinning current of a square Josephson array was presented. First, it was found in experimental measurements and dynamic simulation that as $\lambda_\perp$ becomes smaller than one, the depinning current is increased. In static simulation of a single vortex, the cell-to-cell energy barrier increased as $\lambda_\perp < 1$. Since the depinning current is proportional to the energy barrier, the effect of self-induced fields on the depinning current can be explained in terms of the energy of the array. In essence, the increase in the energy barrier is caused by the localization of the vortex. As the vortex becomes smaller the energy required to stay in the middle of a cell approaches zero, but the energy required for a vortex to be on top of a junction does not and hence the barrier increases as $\lambda_\perp$ decreases. Secondly, strong self-fields disturb the formation of commensurate vortex lattices on the array. It appears that the screening due to a small $\lambda_\perp$ prevents the vortices from forming these superlattices. As $\lambda_\perp$ decreases, the depinning current becomes independent of the frustration. Thirdly, for smaller arrays, edge-effects are important in describing the dynamics of the array depinning current, even for $\lambda_\perp$ that is of several lattice spacings. The exact mechanisms have not yet been determined.

Chapter 4

The Flux-Flow State

The understanding of vortex motion and pinning in bulk Type II materials is an important area of applied superconducting research. Phenomenological models have been successful in describing the vortex flow, but controlled experiments are difficult to undertake. Furthermore, high-T_c materials have been shown to act as stacked two-dimensional sheets of weakly coupled superconductors. However, it is difficult to fabricate homogeneous films and very difficult to vary the film parameters in a controlled fashion.

Two-dimensional arrays of Josephson junctions provide an ideal controlled environment for the study of vortex transport in superconductors. Vortices in the flux-flow region tend to flow in an incoherent way across the array and are most similar to the motion of vortices in thin films. For values of f that do not produce a commensurate state with the lattice, the flux-flow region is linear and it is possible to calculate a flux-flow resistance, R_{ff}. In this chapter will study the effects of temperature, induced fields and applied magnetic fields to R_{ff}.

4.1 The Experimental Landscape

Several different samples were fabricated and measured in order to investigate the flux-flow resistance in a large parameter range of β_c and $\lambda_\perp$. All of the samples were fabricated using Nb-Al_2O_x-Nb trilayer process with varying critical current densities.

parameter	H1	H2	H3	P
$R_J\,(\Omega)$	260	19	37.7	29.6
$A_J\,(\mu m^2)$	9	9	9	1
$C_J\,(fF)$	300	300	300	67
$\beta_c(0)$	450	33.3	64.3	10.2
$\lambda_\perp(0)$	2.17	0.17	0.31	0.45
$I_c(0)\,(\mu A)$	7.3	91.3	50.9	64.4
$J_c\,(A/cm^2)$	80	1100	570	7000
$p\,(\mu m)$	16.5	16.5	16.5	9
$L_s\,(pH)$	25.1	32.8	25.0	13.6
size (cells)	15x15	15x15	7x7	47x47

Table 4.1: The measured samples. R_J is the normal state resistance of the Josephson junction, A_J is the area of the junction and C_J the capacitance. L_s is the self-inductance of the loop and p is the lattice spacing of the array.

All had uniform current injection and none of the junctions was shunted. The relevant parameters are shown in Table 4.1.

Samples in group H were fabricated at Hypres [16]. Most of the results presented are measurements from this group. Arrays H1 and H2 were designed with a size of 15×15 in order to make the comparison to simulations easier. For larger arrays the simulation runs take a prohibitively long time. Sample P was fabricated at IBM with its planarized all-refractory technology (PARTS) [18]. This array has a small β_c range, so the effects of $\lambda_\perp$ can be studied more accurately.

The measurements were performed in a He^4 probe. Inside the vacuum can there is a μ-metal shield surrounding the sample as well as a small magnet that is used to apply a perpendicular magnetic field of 0 to 300 mG. To reduce high-frequency noise, the leads from the sample pass through π filters before measurements are taken. Data was recorded on a computer via the use of digital voltmeters and digital lock-in amplifiers with the use of standard four probe measurement techniques.

The junction normal state resistance, R_n, is determined from the measured array resistance, $R_{n,array}$ by the relation $R_n = R_{n,array}(N_x + 1)/N_y$, and is independent of temperature. N_y is the number of array cells in the direction of current flow, while N_x is the number of cells perpendicular to the injected current. The junction

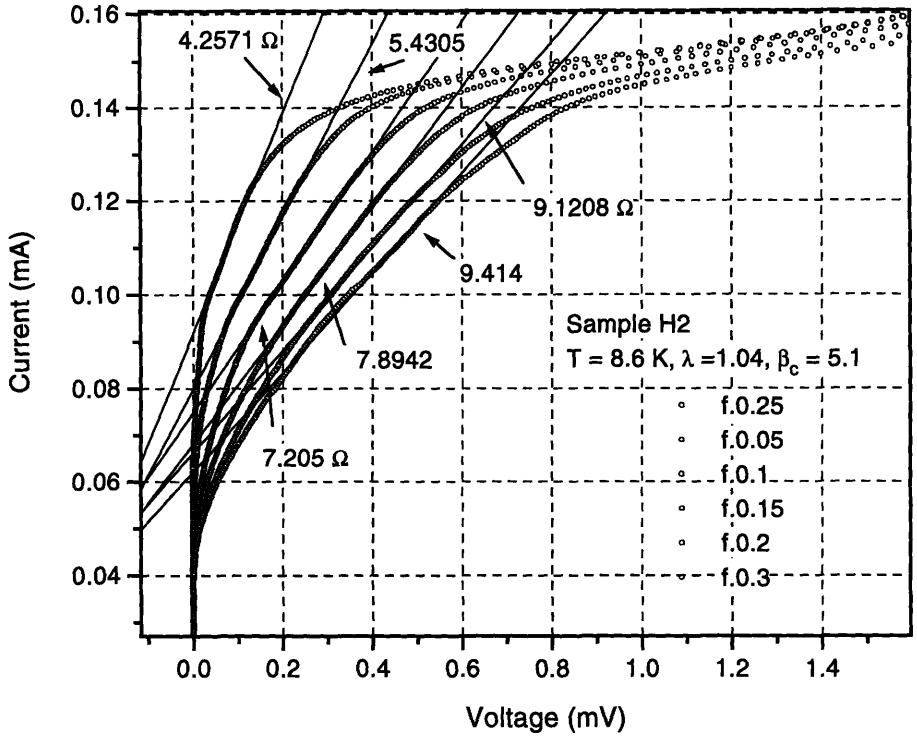

Figure 4-1: Typical set of *I–V* 's taken by varying the magnetic field from $f = 0.1$ to 0.3 at 8.6 K with $\lambda_\perp = 1.04$ and $\beta_c = 5.1$. The numbers indicate the resistance of the flux-flow.

critical current is assumed to follow the Ambegaokar-Baratoff [1] dependence $I_c = 0.86(\pi\Delta/2eR_n)\tanh(\Delta/2k_BT)$, where Δ is the temperature dependent quasiparticle excitation gap. The I_cR_n product of a junction is constant and equal to 1.9 mV. By measuring the normal state resistances of various samples on a single trilayer the critical current uniformity can be estimated to be 10%. The junction capacitance is calculated by measuring the Fiske steps of a one-dimensional array [39].

Typical current-voltage, *I–V* , characteristics vs. applied magnetic field are shown in Fig. 4-1. The depinning current, I_{dep}, indicates the onset of the flux-flow region which extends until the voltage switches. There is a transition part of the *I–V* curve from the depinning current to a linear region. The flux-flow resistance, R_{ff}, is defined as the slope of this linear region. The graph shows the assigned resistance values versus different applied magnetic fields.

Fig. 4-2 shows the temperature dependence of the flux-flow region. Since the depinning current varies with temperature, both the measured current and voltage

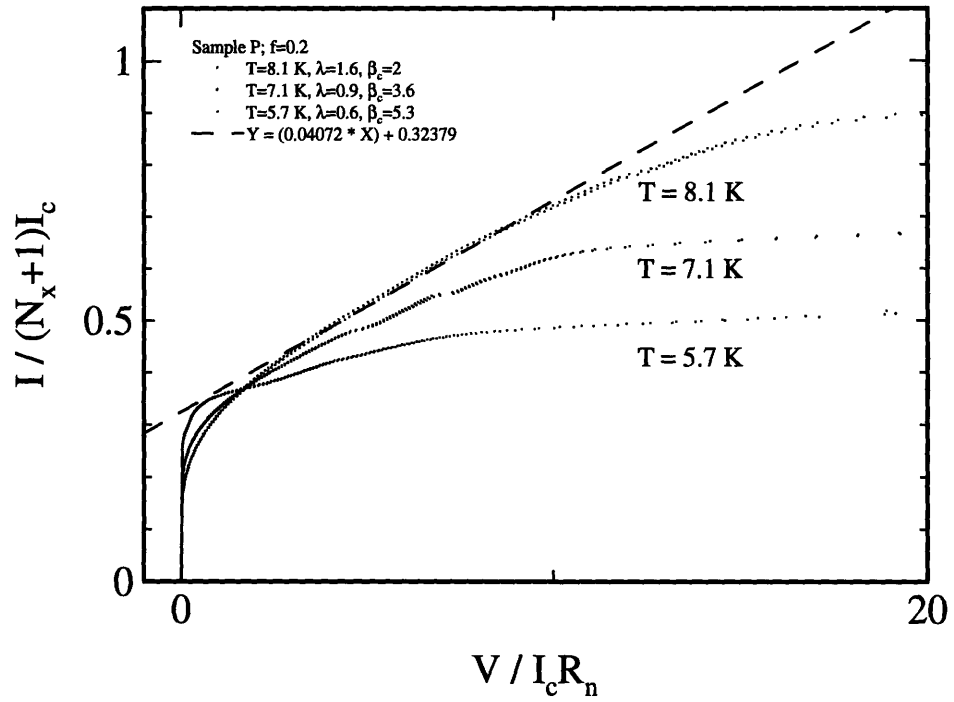

Figure 4-2: Typical set of I–V's taken by varying the temperature at $f = 0.2$. In this sample $\beta_c < 6$ so that only the parameter $\lambda_\perp$ affects the slope.

have been normalized by $(N_x + 1)I_c$ and I_cR_n respectively. This allows for a better comparison of the flux-flow slope. Even when the applied current is normalized, the depinning currents will not be equal since they depend on the value of $\lambda_\perp$ as well as temperature. In this particular measurement the resistance decreases with increasing temperature. For other arrays or even temperature ranges the flux-flow slope might have an opposite behavior. In general, it is not possible to describe how the flux-flow slope will change solely with respect to temperature.

However, by changing the temperature of the sample we can vary a junction's I_c and change its β_c and $\lambda_\perp$ by up to a factor 5 in a controlled way. It is therefore possible to map out the R_{ff} dependence on both β_c and $\lambda_\perp$. Recall that $\lambda_\perp$ is inversely proportional to I_c while β_c is proportional to I_c, therefore in the experiments $\lambda_\perp$ and β_c cannot be varied independently and, as will be shown below, affect the flux-flow slope in an opposite way and thereby make the interpretation of the measurements difficult. Instead of interpreting this temperature dependence directly, a phenomenological model will be presented that explains the slope of the flux-flow region in terms of the

junction parameters $\lambda_\perp$ and β_c.

It is also possible to measure the dynamic resistance, R_d, directly by the use of a lock-in technique. A small ac excitation current is mixed in with the dc bias current and the resulting voltage is measured with a lock-in amplifier. The ratio of the output voltage and input excitation current gives R_d. Care was taken to use a frequency high enough to avoid the $1/f$ noise of the amplifier while low enough to avoid cross-talk in the lead wires. A frequency of 237 Hz was used for most of the lock-in measurements. A small excitation amplitude was also used in order to avoid sample heating.

The top graph of Fig. 4-3 depicts a typical measurement of the R_d vs. dc bias current at different values of applied field. The peak at $f = 0.5$ is a consequence of the rising depinning current at the commensurate field. The taller peaks at the high bias current indicate switching of the I–V from the flux-flow state to row-switched state. To get a better perspective for this flux-flow 'surface' the R_d is re-plotted in the bottom graph of Fig. 4-3.

There are regions of constant resistance in Fig. 4-3 that are associated with flux-flow. This resistance is better defined for frustrations that are less than 0.3. For higher values of f the slope ceases to be linear and it is difficult to assign an R_{ff}. As will be shown in later sections, the applied current needs to be strong enough so that vortices do not feel the intrinsic pinning force of the array lattice before the I–V begins its linear region. For this reason R_{ff} is only well defined for a region well above I_{dep}. Hence, the measured R_{ff} values are collected by performing a least square fit on the most linear part of the flux-flow region.

4.2 Phenomenological theory

In this section, a phenomenological theory for the flux-flow resistance that will explain the experimental dependence of the flux-flow resistance on the applied magnetic field and temperature will be developed. The effects of self-induced fields will also be analyzed.

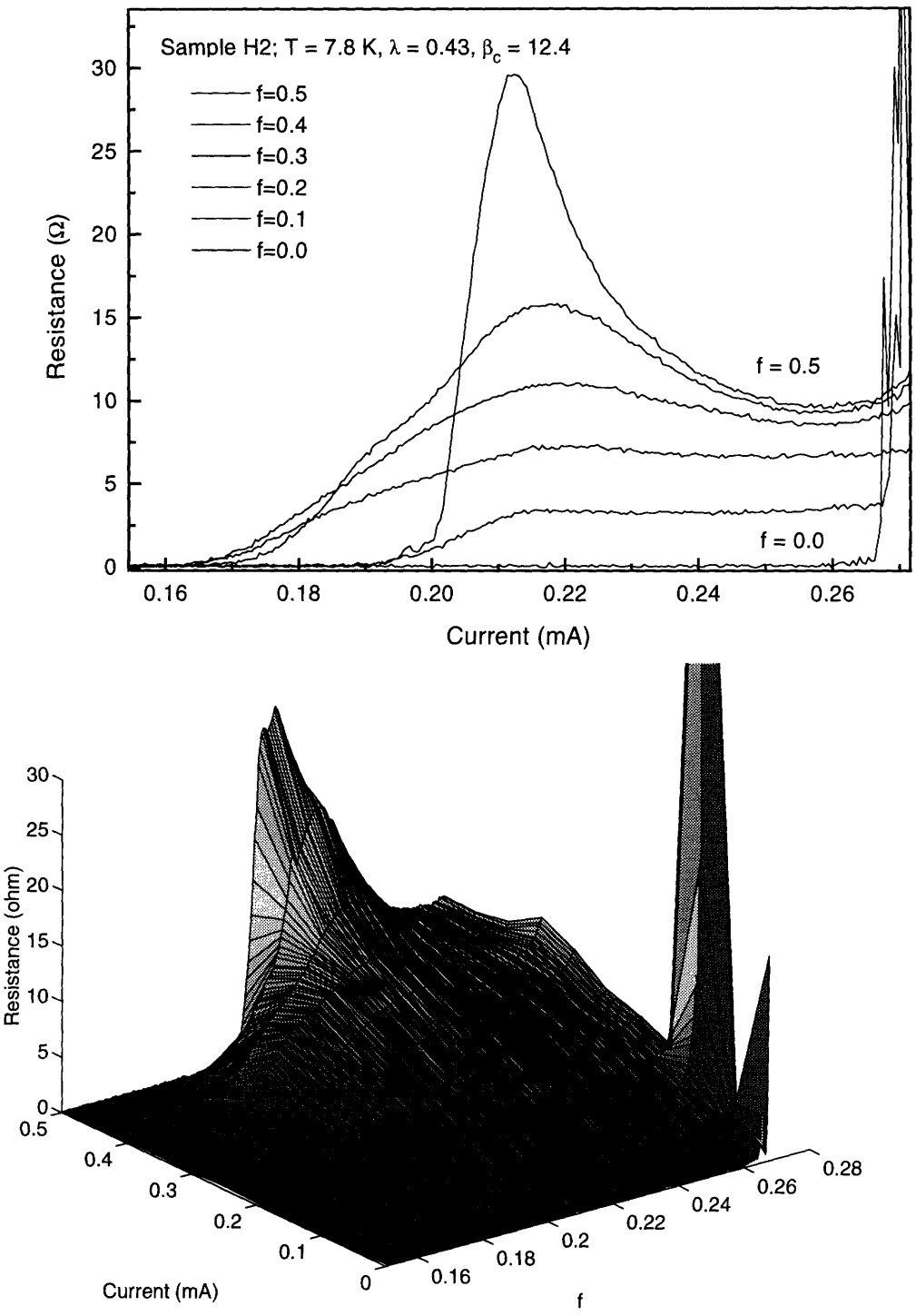

Figure 4-3: Top: typical set of R_d vs. bias current measurements taken by varying the magnetic field at T = 7.8 K. Bottom: same set of R_d measurements plotted to depict the flux-flow landscape.

4.2.1 Equation of motion

The essence of the phenomenological model is that a vortex can be treated as a massive independent particles. The justification for the model will rest on how well it can explain the experimental facts of flux flow. The basic assumptions are as follows:

- vortices are particles with mass $M(\beta_c, \lambda_\perp)$
- vortices do not interact
- vortices experience linear damping
- arrays are of infinite length

With these assertions a Bardeen-Stephen like model for flux-flow can be developed.

If the arrays are current biased in the $\hat{y}$-direction the vortices will experience a Lorentz force in the $\hat{x}$-direction. Let a vortex travel across an array with velocity $u(x)$, the equation of motion of the vortex becomes

$$M(\beta_c, \lambda_\perp)\ddot{x} + \eta\dot{x} = \frac{dU(x)}{dx} \tag{4.1}$$

where $U(x)$ includes the force of the driving current, $\Phi_0 I_{ext}/p$, and the cell-to-cell potential barrier to discussed in the previous chapter. The spatial properties of the barrier have been analyzed and for the $\lambda_\perp = \infty$ limit the potential due to the barrier can be schematically viewed as an egg carton. This is the two-dimensional version of the famous washboard potential of a Josephson junction. Since the vortices only travel in the $\hat{x}$-direction, the resulting slice of the "egg carton" potential is a cosine. The equivalent potential energy that describes the array is thus

$$U(x) = -\frac{1}{2}(\Delta E)E_J \cos\left(\frac{2\pi x}{p}\right) - \frac{\Phi_0}{p} I_{ext} x, \tag{4.2}$$

where ΔE is the value of the energy barrier.

4.2.2 Calculating the mass

In underdamped arrays, one cannot neglect the shunt capacitance of the RCSJ model. This capacitance creates an electrical energy that needs to be taken into account. This energy

$$\frac{1}{2}C\sum V^2 \tag{4.3}$$

can be calculated using a quasi-static approximation. In reality there is capacitive coupling between every superconducting island and to ground that need to be included to the electrical energy. However, this effect is much smaller than the inductance effects caused by the array loops. Hence, only nearest neighbor capacitances, the RCSJ shunt capacitance, have been used in the calculations.

In this calculation the voltage is approximated from the static current distribution of a vortex. As shown below, this energy is proportional to the square of the velocity of the vortex and can be viewed as kinetic energy. The coefficient of the squared velocity can in turn be interpreted as the vortex mass.

As a first approximate step, we assume that far from the vortex core we can linearize the basic Josephson current relation

$$J \approx J_c\phi \tag{4.4}$$

If we let u be the vortex velocity, d/dx, then for the $\hat{x}$-direction

$$\frac{d\phi}{dt} = \frac{d}{dt}\frac{J}{J_c} = \frac{u}{J_c}\frac{\partial}{\partial x}J_x \tag{4.5}$$

and similarly for the $\hat{y}$-direction. It is now possible to estimate the magnitude of $\dot{\phi}$,

$$\left|\frac{d\phi}{dt}\right| = \frac{u}{J_c}\left[\left(\frac{\partial J_x}{\partial x}\right)^2 + \left(\frac{\partial J_y}{\partial x}\right)^2\right]^{\frac{1}{2}}, \tag{4.6}$$

and the resulting magnitude of the voltage by using the Josephson voltage relation

$$|V| = \frac{\Phi_0}{2\pi}\left|\frac{d\phi}{dt}\right|$$

$$= \left(\frac{\Phi_0}{2\pi}\frac{u}{J_c}\right)\left[\left(\frac{\partial J_x}{\partial x}\right)^2 + \left(\frac{\partial J_y}{\partial x}\right)^2\right]^{\frac{1}{2}}. \tag{4.7}$$

From Eq. 4.7, the square of the voltage is proportional to the square of the vortex velocity. Hence, the electrical energy of the array can be equated to the kinetic energy of the vortex

$$\frac{1}{2}Mu^2 = \Gamma = \frac{1}{2}C\sum V^2 \tag{4.8}$$

where the sum is over all junctions in the array. In the continuum limit

$$\sum V^2 \approx \int\int V^2 \frac{dx}{p}\frac{dy}{p} \tag{4.9}$$

and the resulting double integral after substituting Eq. 4.7 is

$$\Gamma = \left(\frac{\Phi_o}{2\pi}\frac{u}{J_c p}\right)^2 \int_\xi^\infty \int_\xi^\infty \left[\left(\frac{\partial J_x}{\partial x}\right)^2 + \left(\frac{\partial J_y}{\partial x}\right)^2\right] dxdy \tag{4.10}$$

where ξ represents the cutoff at the vortex core.

By linearizing the Josephson relation and applying the chain rule to convert time derivatives into spatial ones, the voltage of a junction has been re-expressed from its phase difference to the local spatial current distribution. To calculate Γ all that needs to be determined is the current distribution of a vortex. Since the equations have been linearized, it seems appropriate to use the thin film results to derive J.

When the magnetic penetration depth is larger than the array size there are no induced fields and the vortex size is independent of the penetration depth. In this regime the arctan approximation can be used. For the linearized Josephson relations at $f = 0$ the surface current is $K = I_c\nabla\theta$, where θ represents the phase distribution in a thin film and K is the superconducting surface current. Let the superconducting thin film have a thickness of d. If the film is thin enough such that the current is uniformly distributed across its cross-section, then $K = dJ$ and for the arctan approximation

$$J\frac{d}{I_c} = \frac{1}{r}\hat{\theta} = \frac{1}{r}(-\sin\theta\hat{x} + \cos\theta\hat{y}). \tag{4.11}$$

Substituting J_x and J_y into the above double integral, Eq. 4.10, and converting into cylindrical coordinates, we find

$$\Gamma = \left(\frac{\Phi_o}{2\pi}\frac{u}{J_c p}\right)^2 \left(\frac{I_c}{d}\right)^2 \int_\xi^\infty 2\frac{\pi}{r^3} dr. \tag{4.12}$$

The critical current can be rewritten in terms of a current density, $I_c = A_J J_c$, and by letting the area of the Josephson junction, A_J, equal to dp, we get

$$\sum V^2 \approx \Gamma = \left(\frac{\Phi_0 u}{2\pi}\right)^2 \frac{\pi}{\xi^2}. \tag{4.13}$$

The coupling of the length scales of the thin film current distribution and lattice spacing of the arrays occurs through the area of the junction. In a sense the junction becomes a phenomenological window that allows this coupling since the equations have been linearized and no proper Josephson junction can exist.

It has been shown that the vortex core cut-off value is equal to $\xi = p/\sqrt{2\pi}$ [10]. Using this value, the expected form of vortex mass is derived,

$$M = \frac{\Phi_0^2}{2}\frac{C}{p^2}. \tag{4.14}$$

This value of the mass was derived in the $\lambda_\perp = \infty$ limit using the arctan approximation. As will be shown below, mutual inductances, or equivalently a small $\lambda_\perp$, have a considerable effect on the vortex mass.

4.2.3 The effective damping

With a Bardeen-Stephen-like model for flux-flow, we can equate the viscous energy dissipated by a vortex moving between adjacent cells to the power dissipated in each junction [37]. Even though our array is current biased, when a vortex crosses a junction, the junction behaves as if it were voltaged biased. Specifically in the quasi-static approximation the moving vortex imparts a voltage of $(\Phi_0/2\pi)\Delta\phi/\Delta t$, where $\Delta\phi = \pi$ and $\Delta t = p/u$. During this brief time the junction will behave as if it was voltaged biased. If the vortex is moving at a constant velocity then the power

dissipated by the viscous medium is equal to the power dissipated in all the junctions:

$$\eta_{bs} u^2 = \sum V^2 / R_e. \tag{4.15}$$

R_e represents the effective voltage bias resistance of the junction which depends on temperature and voltage, and the sum is over all the junctions in the array. For most of the measurements, the temperature is near to T_c and $R_e \approx R_n$.

Using the same approximations as when calculating the mass, it possible to estimate the sum of the squared voltages and calculate the damping coefficient,

$$\eta_{bs} = \frac{\Phi_0}{2p^2} \frac{1}{R_n}. \tag{4.16}$$

As expected from the voltage biased condition, the larger the resistance, the lower the dissipated power. This result is calculated for a steady-state motion of a vortex so that it is independent of β_c and does not include the effect of mutual inductances.

4.2.4 Dependence on f

When a vortex is driving at high currents and is at steady state we can simplify the equation of motion by neglecting the cell-to-cell energy barrier. In this limit the Lorentz driving force is much larger than the pinning force and the effect of the barrier can be ignored. For the vortex to be at steady state, the viscous drag force, ηu, must be balanced by the driving current. Hence at constant bias the vortices are traveling at a constant velocity $u = \Phi_0 I_{ext} / \eta p$.

Let the system have n_f independent vortices at this constant velocity. The frequency at which they pass along the array is $u/N_x p$. Hence the voltage is

$$\begin{aligned} V &= \frac{\Phi_0}{2\pi} \dot{\phi} = \frac{\Phi_0}{2\pi} \omega \\ &= \frac{\Phi_0}{2\pi} 2\pi u / (N_x p) n_f \\ &= \Phi_0 n_f / N_x p. \end{aligned} \tag{4.17}$$

When $\lambda_\perp > 1$ the free vortex density can be estimated by $n_f = fN_xN_y$. Substituting the corresponding f and the steady state value of the array driving current, $(N_x + 1)I_{ext}$

$$R_{ff} = 2f\frac{N_y}{N_x+1}R_n. \tag{4.18}$$

A linear resistance is expected at fixed values of f.

4.2.5 Dependence on β_c

It has been shown in simulations [35] and experiments [37] that underdamped arrays have an enhanced viscosity. This is due to spin-wave excitation created by moving vortices. These spin-waves are caused by the LC oscillations of the Josephson equivalent inductor, L_J, and the junction capacitance that resonate at a frequency of $\omega_p = 1/\sqrt{L_JC}$

Recall that a moving vortex imparts a voltage $V_{max} = (\Phi_0/2\pi)\Delta\phi/\Delta t = (\Phi_0/2\pi)\pi u/p$ when it crosses a junction. Therefore, when the vortex moves to the next cell, the junction in its wake will oscillate with a voltage of

$$V = V_{max}\cos(\omega_p t) \tag{4.19}$$

Using the Josephson voltage relation, it is possible to calculate the corresponding maximum amplitude of ϕ, D_{max}. In the quasi-static limit $D_{max} = (2\pi/\Phi_0)V_{max}/\omega_p$ and the energy per unit time becomes $D_{max}E_J/\Delta t$. Equating this energy to the dissipated power $\eta_{sw}u^2$ yields

$$\eta_{sw} = \frac{1}{2\pi}\frac{\Phi_0^2}{2p^2}\frac{1}{\sqrt{L_J/C}}. \tag{4.20}$$

Spin wave dissipation is independent of R_n. Though it might at first be counter-intuitive, it easily explained. When a passing vortex deposits some of it's energy in a junction, this energy will probably be dissipated in an RC time-scale. However, the equivalent array viscosity does not try to explain how long it takes for power to leave the array, but how much power a vortex losses to the array. In this regard, the power

lost by the vortex is only dependent on the amplitude that it can impart on the LC oscillations and that is mostly dependent on the value of C.

We can also rewrite the spin-wave damping in terms on the Bardeen-Stephen like damping,

$$\eta_{sw} = \frac{1}{2\pi}\sqrt{\beta_c}\,\eta_{bs}. \tag{4.21}$$

The more underdamped the array, the larger the dissipation due to spin-waves.

4.2.6 Dependence on $\lambda_\perp$

When calculating the mass and viscosity of the array, it was assumed that the $\lambda_\perp$ was larger than the array so that the effects of the mutual inductances could be neglected. If the penetration depth is smaller than the sample size, then the induced fields are important and the current distribution of a vortex is no longer described by the arctan expression. However, it can be approximated well by the equation due to Pearl [24]

$$\begin{aligned} K &= \frac{\Phi_0}{2\mu_0\pi\lambda_\perp}\frac{1}{r}\frac{1}{1+r/2\lambda_\perp}\hat{\theta} \\ &= I_c\frac{1}{r}\frac{1}{1+r/2\lambda_\perp}\hat{\theta}. \end{aligned} \tag{4.22}$$

Here, K is the surface current of a infinite thin film with one vortex. In the limit where $\lambda_\perp = \infty$, the arctan result is recovered. Also, $\lambda_\perp$ is the physical penetration depth and is not normalized to p.

Using the procedure outlined in Sec. 4.2.2 to estimate $\Gamma \approx \sum V^2$ and using the same vortex core cutoff of $p/\sqrt{2\pi}$, we find

$$\Gamma = 2\left(\frac{\Phi_0 u}{2p}\right)^2 G(\lambda_\perp) \tag{4.23}$$

where

$$G(\lambda_\perp/p) = 1 - \frac{1}{2}\frac{p}{\lambda_\perp}\sqrt{\frac{2}{\pi}} + \frac{1}{8}p^2\frac{\ln\alpha\sqrt{2\pi}/p}{\lambda_\perp^2\pi} + \frac{1}{4}\frac{p^2}{\pi\lambda_\perp\alpha} + \frac{1}{4}\frac{p^2}{\pi\alpha^2} - \frac{1}{3}\frac{p^2\lambda_\perp}{\pi\alpha^3} \tag{4.24}$$

and

$$\alpha = \frac{1}{2}p\sqrt{\frac{2}{\pi}} + 2\lambda_\perp. \tag{4.25}$$

This equation describes the effect on the sum of the junction voltages when the vortex size is decreased from the $\lambda_\perp = \infty$ case. Though it seems to depend on $\lambda_\perp$ and p separately, it actually only depends on the ratio of $\lambda_\perp/p$, which is the usual normalized definition of $\lambda_\perp$. This can be shown more clearly with the following equation that approximates Eq. 4.24 accurately

$$G(\lambda_\perp) \approx 1 - \frac{1}{2}\sqrt{\frac{2}{\pi}}\frac{1}{\lambda_\perp} + \frac{7 + 3\ln(8\pi\lambda_\perp^2)}{48\pi}\frac{1}{\lambda_\perp^2} \tag{4.26}$$

here $\lambda_\perp$ is the usual normalized penetration depth.

Therefore, the mass equals

$$M = \frac{C\Phi_0^2}{2p^2}G(\lambda_\perp) \tag{4.27}$$

and η becomes

$$\eta = \frac{\Phi_0^2}{2p^2}\frac{1}{R_n}G(\lambda_\perp). \tag{4.28}$$

To get an idea of this dependence on the mass and similarly on the viscosity, $G(\lambda_\perp)$ is plotted in Fig. 4-4. The solid circles represent a quasi-static calculation where the sum of the junction voltages was calculated numerically taking into account all of the mutual inductances in the array. M_0 is the expected mass for $\lambda_\perp = \infty$. Though not shown in the figure, the quasi-static calculation was performed for arrays as small as 7×7 and as large as 31×31 and the results were almost identical as for the 15×15 array. This is not surprising since in the mass is calculated by moving one vortex from one cell to the next and calculating the resulting voltage changes. Even if the size of the vortex, $\lambda_\perp$, is large the voltage differences are mostly localized to the nearest cells. The fit of $G(\lambda_\perp)$ to the quasi-static calculation is surprisingly good.

The reduction of both the vortex mass and array viscosity can be explained easily.

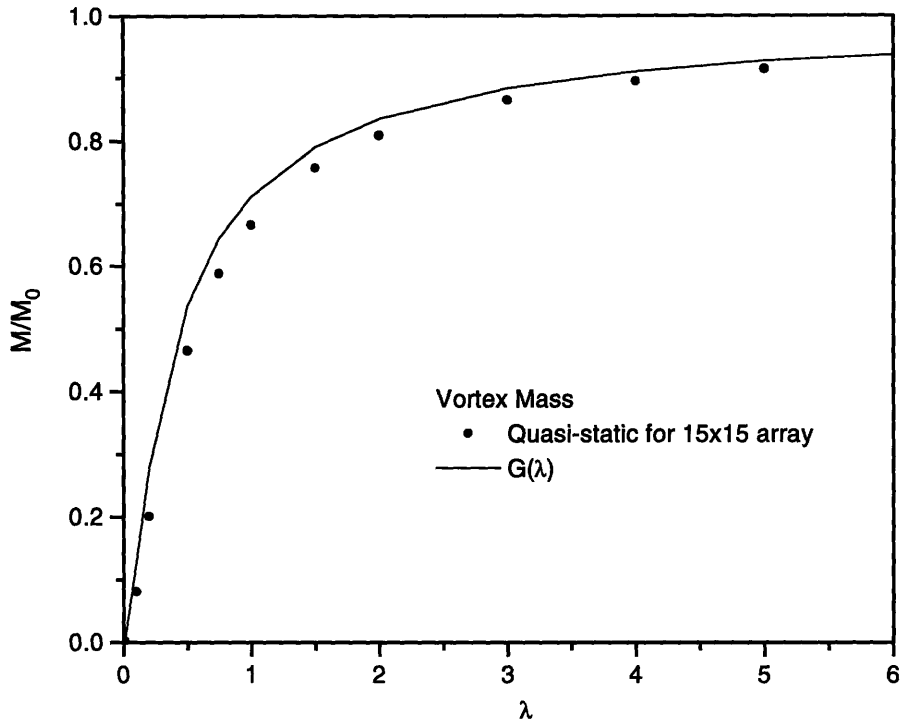

Figure 4-4: Vortex mass normalized to the vortex mass at $\lambda_\perp = \infty$ calculated using the quasi-static approximations for a continuous film, and a discrete Josephson array of 15×15 cells.

As $\lambda_\perp$ approaches zero, the mass decreases and the viscosity will also decrease. For strong mutual inductances, $\lambda_\perp < 1$, the extent of the vortex can still be modeled by a radius of $\lambda_\perp$. As $\lambda_\perp$ becomes smaller the vortex becomes physically smaller and as it moves across the array it crosses less junctions and it dissipates less energy. This is equivalent to reducing the viscosity of the array.

4.2.7 Flux-flow model with $\lambda_\perp$ and β_c dependence

To combine all of the above concepts into a comprehensive phenomenological picture of flux-flow in a square array, we need to make one last assumption. We will postulate that the damping is separable into the Bardeen-Stephen component and the spin-wave damping,

$$\eta = \eta_{sw}\eta_{bs}. \tag{4.29}$$

Using the calculated values of the appropriate damping, Eq. 4.21 and 4.28, it is possible to formulate the viscosity in terms of the array parameters

$$\eta = \frac{\Phi_0^2}{2p^2}\frac{1}{R_n}\frac{\sqrt{\beta_c}}{2\pi}G(\lambda_\perp) \tag{4.30}$$

Again, since the junctions are voltaged biased the viscosity is inversely proportional to the flux-flow resistance and

$$R_{ff} = 2f\frac{N_y}{N_x+1}R_n\frac{2\pi}{\sqrt{\beta_c}}\frac{1}{G(\lambda_\perp)} \tag{4.31}$$

as $\beta_c > 1$. With this result it is possible to interpret the experimental data.

4.3 Comparison with experiments and simulations

To verify the validity of the phenomenological model, a series of simulations and measurements was performed. Fig. 4-5 shows typical simulated I–V. Since we are trying to characterize inductance effects, our simulations use the consistent set of Maxwell's equations and take into account the inductive interaction between all the

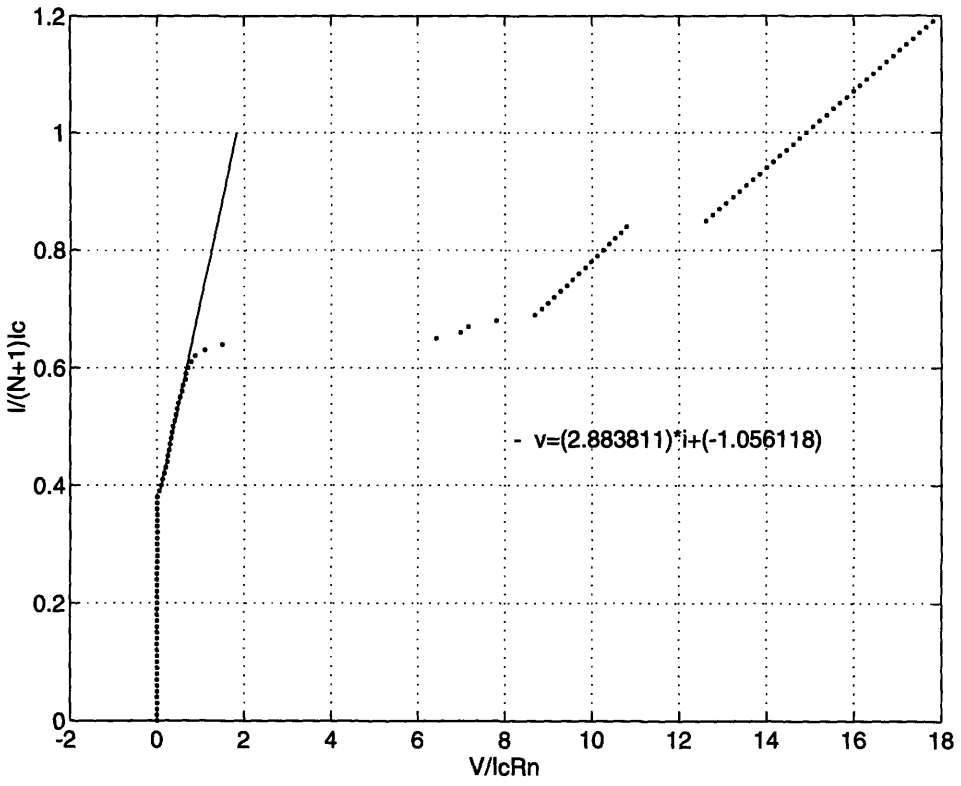

Figure 4-5: Simulated I–V's for a 15×15 array with $\lambda_\perp = 0.5$.

cells of the array. Further details of the simulations are described in Chapter 2.

The flux-flow region of both the experimentally measured I–V's, Fig. 4-1, and the simulated I–V's are examined in the same manner. Flux-flow is defined from the moment of depinning until the voltage jumps to a row-switched state. In this state the array dynamics can be described in terms of localized vortices. In simulations this region is linear when the applied magnetic field is not commensurate with the array lattice. At field values of 0.5 or 0.25, the depinning current raises slightly and the flux-flow region becomes linear only at the top part of the flux-flow step. For this reason, we always extract the flux-flow resistance using a least-square fit on the top part of the flux-flow region. A similar situation occurs in the measurements. Most of the measurements are taken at temperature that are close to T_c. This is because in this temperature range the critical current, and hence $\lambda_\perp$, has the largest variations. At higher temperatures there are smooth transitions from the superconducting state to a linear region. In this case we define our flux-flow resistance as the part of the

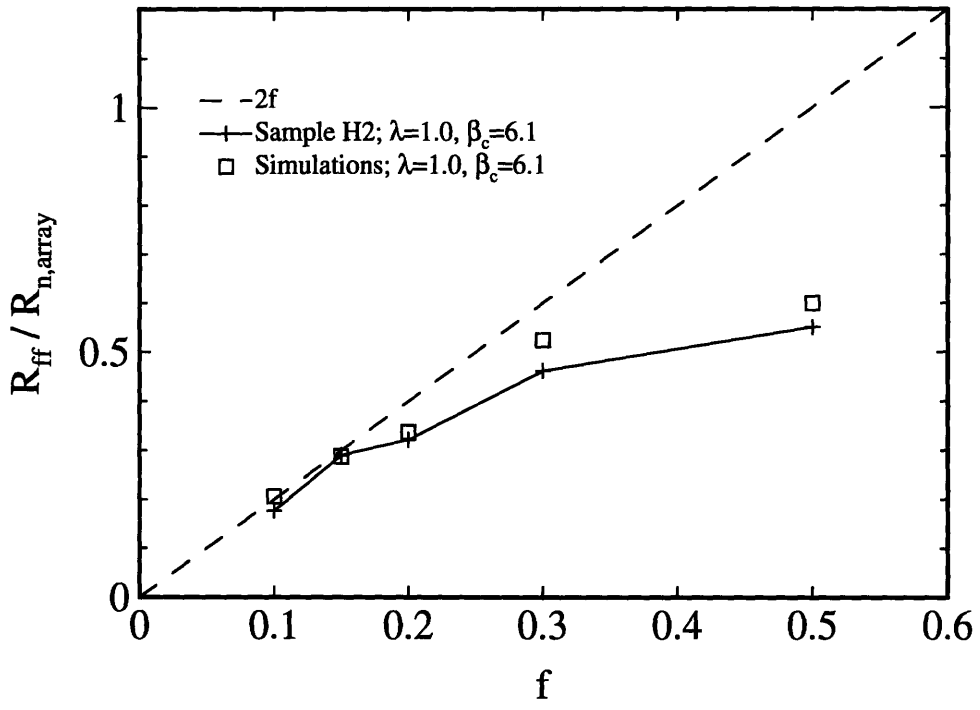

Figure 4-6: Comparison between measured R_{ff} vs. f for sample H2 and simulations.

I–V which is most linear shown in Fig. 4-1 and we extract the resistance using a least-square fit.

A direct comparison was performed between the measured data and the simulations. The crosses of Fig. 4-6 represent the measured data, while the open squares are simulations with the same parameters. The correspondence between simulation and experiment is very good for small values of f and deviates only slightly for larger values. Also for small values of f the data has a slope only slightly lower than the predicted $2f$.

First we will investigate the β_c dependence of the flux-flow resistance. Fig. 4-7 shows both measurements and simulations and the expected dependence of $1/\sqrt{\beta_c}$.

The simulations were performed in the limit of $\lambda_\perp = \infty$ and the aluminum measurements are for $\lambda_\perp \gg 1$. In this regime, where the self-induced fields can be neglected, the flux-flow resistance can be characterized in terms of spin-wave damping. At higher values of β_c there appear to be a reduction of the spin-wave damping in the simulations. It is likely this is due to the small size of the simulated array.

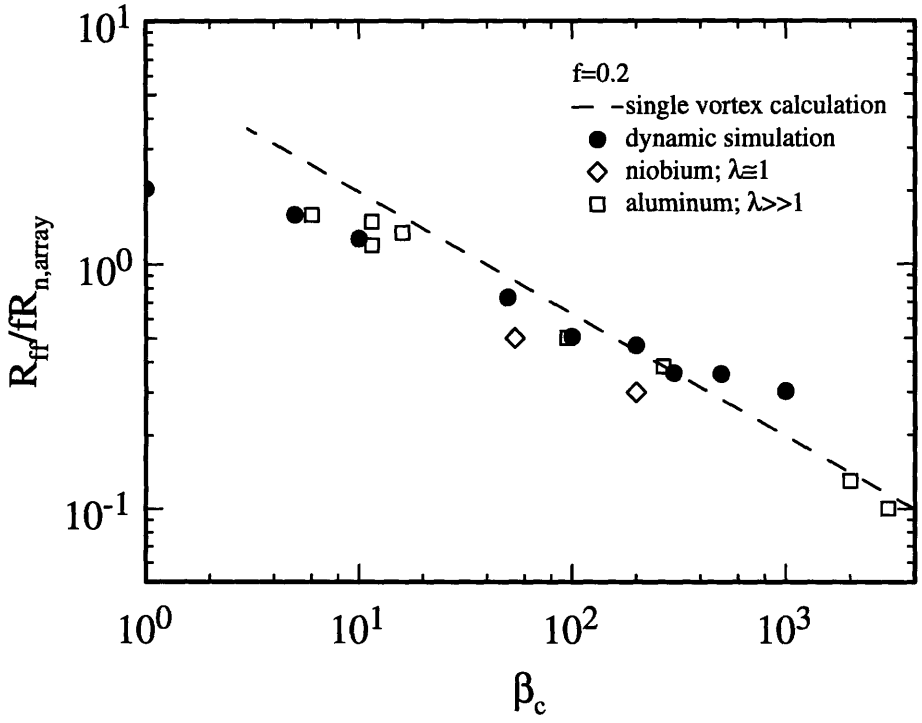

Figure 4-7: Measured R_{ff} vs. β_c for samples H1 and a large aluminum array. Filled-in circles are simulations with $\lambda_\perp = \infty$ for a 15×15 array with $f = 0.2$. Dashed line is spin-wave dependence.

Fig. 4-8 shows the compilation of the raw flux-flow resistance data for the samples and various values of the applied field. The filled-in circles represent data from dynamic simulation of a 15×15 array.

The simulations were performed with a β_c of 5 in order to reduce the effects of spin wave damping. The dashed line is the phenomenological dependence for a single vortex, Eq. 4.24. The measurements were taken for samples H1, H2 and P. Sample P has a β_c of less than 5. This data has very similar trend to the expected theoretical calculation because spin-wave damping is negligible. Sample H1 has β_c of the order of 300. Its flux-flow resistance is reduced significantly because of spin wave damping. Sample H2 has a moderate β_c value, ~ 30, and this may account for the deviation from the theoretical prediction. The simulations also lie slightly below the theoretical curve.

Since the data is normalized to f, one would expect all the curves for the respective sample to stack on top of each other. This is not the case and may just be a

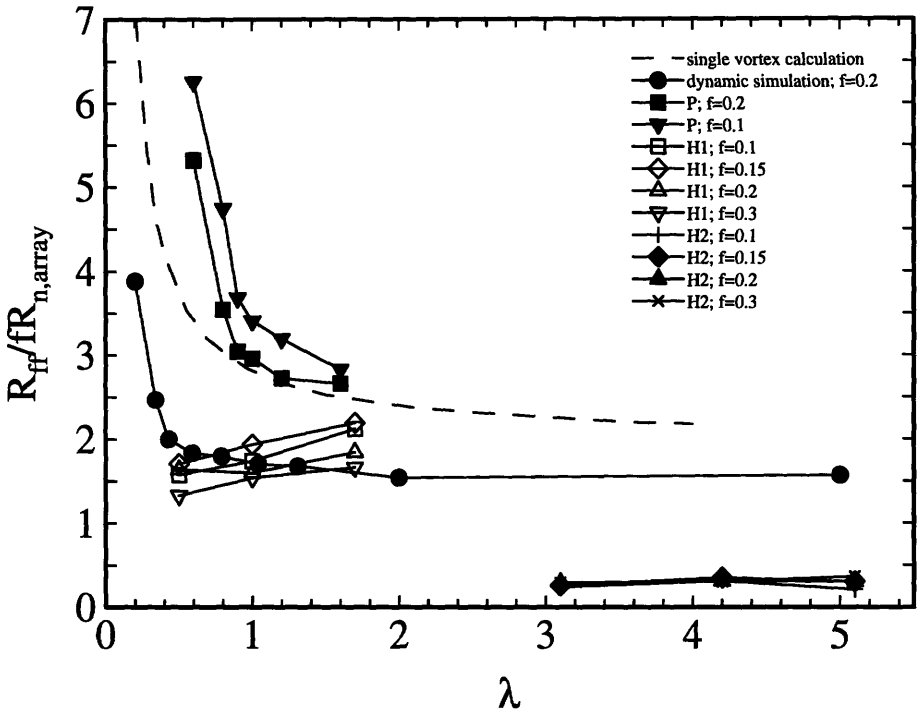

Figure 4-8: Measured R_{ff} vs. $\lambda_\perp$ for samples H1, H2 and P. Dashed line is single vortex approximation while the fill-in circles are points taken from dynamic simulations of 15×15 array with $\beta_c = 5$ and $f = 0.2$.

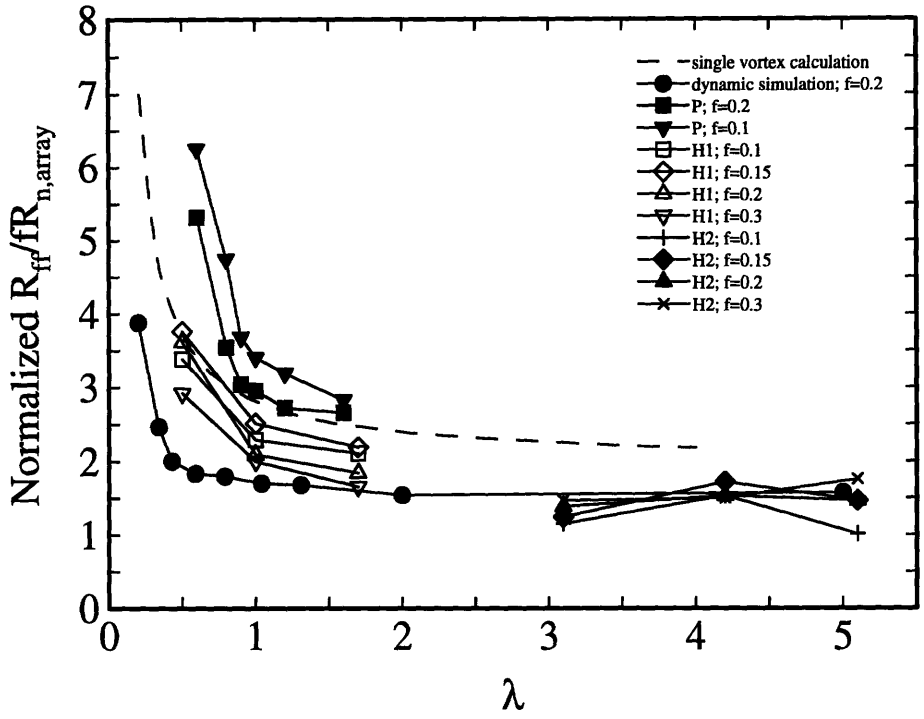

Figure 4-9: Normalized R_{ff} vs. $\lambda_\perp$ for samples H1, H2 and P.

limitation of the phenomenological model. The basic assumption that vortices do not interact probably breaks down as f becomes larger than 0.1 and may account for the displacements of the curves.

By assuming the damping is separable, the R_{ff} values can be renormalized using Fig. 4-7 and therefore made to show only the $\lambda_\perp$ dependence. The reduction of R_{ff} due to spin-wave damping can be estimated and the measured R_{ff} value adjusted accordingly. Fig. 4-9 shows the result. The dashed line represents the theoretical single vortex calculation, while the filled-in circles are the dynamic simulations. The group of data for H2 has an improved fit to the theoretical prediction and the measured data for the H1 follow the simulations closely. In general, the trend of an increased flux-flow slope as $\lambda_\perp$ decreases is apparent in both the measurements and the simulations.

Though the phenomenological theory does not explain all the aspects of the data, it does give a valid description of the $\lambda_\perp$ dependence on the perceived viscosity of a vortex. The result is that strong self-induced fields reduce the viscosity of the array.

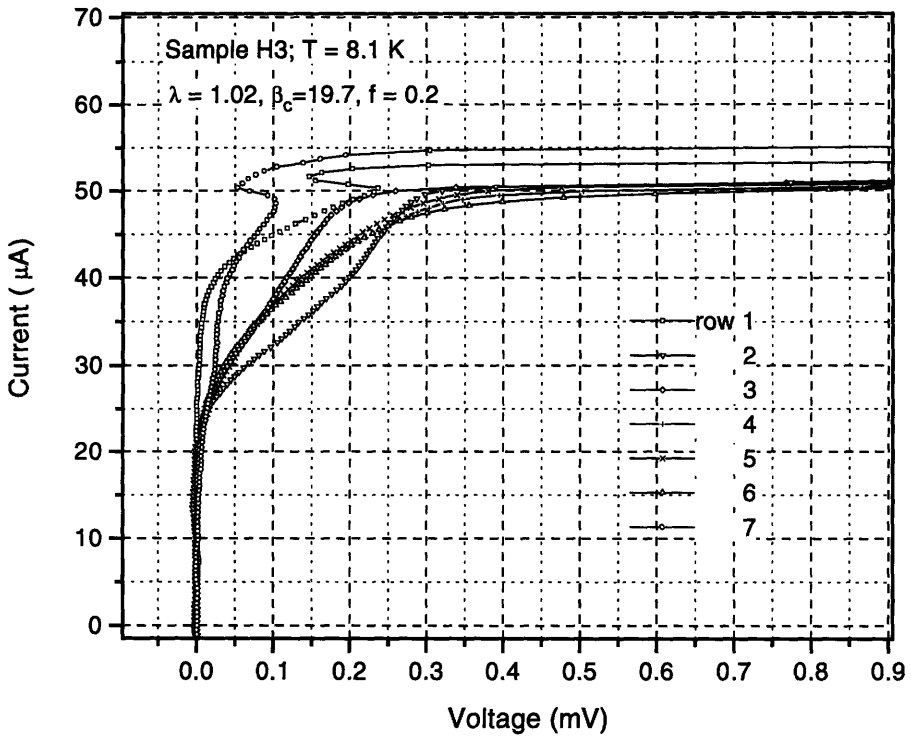

Figure 4-10: Measured I–V for every row of sample H3 at $T = 8.1\,\mathrm{K}$ and $f = 0.2$.

4.4 Deviation from phenomenological theory

Besides the differences between measurements and phenomenological theory pointed in the previous section, there are others that are worth noting.

Though the phenomenological model does not try to include edge effects that does not imply that they can usually be neglected. Sample H3 has voltage pads on every row and it was possible to measure edge effects in the flux-flow region. Fig. 4-10 shows the measured I–V for every row at $f = 0.2$. The first and last rows, the edge rows, have very little flux-flow. Most of the flow is through the center five rows. This was also observed in the simulations. Essentially, different rows have different flux-flow resistances. This spatial dependence may be caused by the edges or nonhomogeneity of the junction critical currents. In general for small array, less than 15×15, there is some row activation in the flux-flow region where some rows are mostly quiet and others have vortices flowing through them. This is visible in the I–V as substructure in the flux-flow region.

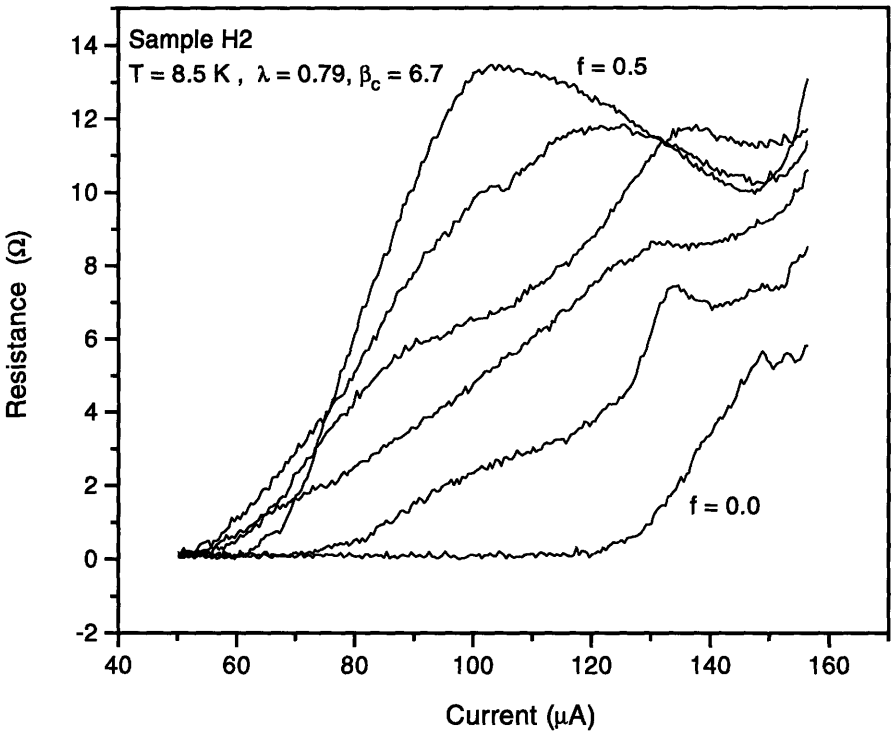

Figure 4-11: Measured R_{ff} for $f = 0, 0.1, 0.2, 0.3, 0.4$ and 0.5 for sample H2 at T= 8.5 K.

In order to define a R_{ff} we need to find a region of constant slope in the I–V. By measuring the dynamic resistance, R_d, directly, one expects to see plateaus of the R_d as in Fig. 4-3. This is due to the linear dependence of the vortex speed with the driving current. However, most measurements do no have this constant resistance. Fig. 4-11 shows a dynamic resistance measurement at T= 8.5 K. In this measurement it is difficult to assigns a single R_{ff} value to an I–V. In fact it seems as though the resistance is linearly dependent on the driving current. Though it is still possible to average all the resistances to assign an R_{ff}, the basic assumption of the phenomenological model of linear dependence of the driving force breaks down.

Experimentally it is possible to measure the slope of the f dependence on the array resistance directly. Biasing the array at a current level in the flux-flow region and continuously changing the applied magnetic field while reading the resistance with a lock-in amplifier will produce graphs such as the one shown in Fig. 4-12. The different curves correspond to different measurements at the indicated bias currents.

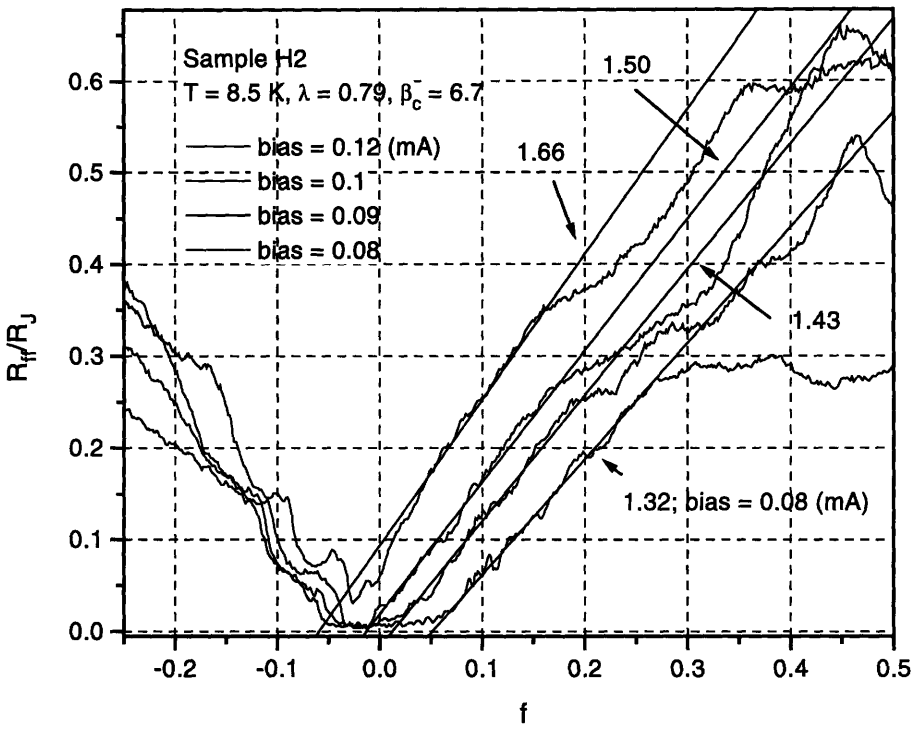

Figure 4-12: Measured R_{ff} vs. f at different current biases. Numbers indicate slope of the line.

There does seem to be a mostly linear dependence for small values of f as expected, but the linear fit is dependent on the bias current. From the phenomenological theory we expect the slope to be of order two and independent of the driving current. Though the order of magnitude is correct these slopes have a relatively large range of values and it is difficult to make quantitative comparisons between measurements at different temperatures. If the flux-flow region were truly linear then for a range of bias currents the f dependence on the flux flow resistance should be constant. This is not observed in most measurements. The lack of linearity in the flux-flow slope may be an indication that the effective array damping is not truly linear but of some other functional form as has been suggested elsewhere [13].

These issues only appear when one tries to quantify the flux-flow resistance very precisely. By taking derivative of the I–V, instead of performing a linear fit on the I–V directly, any deviations will be amplified. However, it is always possible to do a least square fit on the original I–V, even if the flux-flow region is not truly linear

and extract some estimates for the flux-flow that are explained qualitatively by the phenomenological model.

4.5 Conclusions

Josephson arrays represent a complex coupled system. However, in the flux-flow regime the $I-V$ characteristics can be mostly explained in terms of a simple phenomenological theory of vortex transport. These vortices represent a bundle of magnetic flux that are linearly driving by the applied current. Furthermore, vortices in the flux-flow region are localized and, because of the electrical energy in the junctions, can be treated as massive particles. It was assumed that the applied field specifies the density of vortices present in the array. Knowing this density, the driving force, and the viscosity of the array allows for the calculation of the dependence of the flux-flow resistance in terms of the array parameters and applied magnetic field and linear dependence to the applied field is found.

It has also been shown that R_{ff} is dependent on both $\lambda_\perp$ and β_c. The dependence on β_c follows from spin-wave damping while the $\lambda_\perp$ dependence is a result of a reduction of the viscosity caused by the decreasing physical size of traveling vortices as $\lambda_\perp$ decreases. This simple phenomenological theory gives a qualitative as well as a semi-quantitative description of the dynamics. The effects can also be modeled accurately in simulations that take into account all the mutual inductances between cell pairs.

However, the flux-flow region appears to be richer in its dynamics than the presented model can account for. It has been shown that for small arrays, there is a spatial dependence of the flux-flow region. Different rows have different flux-flow slopes and the outer rows closest to the edge appear to have almost no flux-flow associated with them. Also, the effective linear damping of the array appears be an over-simplification. Though these deviations do not diminish the useful and intuitive results from the phenomenological theory, they do point the way for further research.

Chapter 5

Beyond Flux-Flow

When the flux-flow state of an underdamped Josephson junction array becomes unstabilized, the *I–V* curve jumps to a resistive step. It is known from both experiments [38, 34] and simulations [41, 26] that these resistive steps correspond to coherent oscillations of all the junctions in a single row. It is precisely this type of spontaneous coherent oscillation of junctions that makes two-dimensional arrays technologically attractive as high frequency rf devices.

At those resistive steps, the array is usually referred to as being in the row-switched state and every junction in the switched row will be oscillating at the junction gap voltage. The location of the step corresponds to the voltage gap which is temperature dependent. Higher resistive steps in the *I–V* correspond to the switching of more than one row in the array and we do not expect to see more than N_y steps, where N_y is the number of rows in the array. At low temperatures this row-switching behavior was observed and the first part of this chapter is devoted to the characterization of the row-switched steps and how they are affected by self-fields.

At higher temperatures there is a transition between row-switched states and a new type of resonant step. This resonant step differs from the row-switched steps in that the voltage position of the resonant step is temperature independent and self-induced fields play an important role in its formation. The second part of this chapter will characterize some of the properties of the novel step.

5.1 Row-switched states

Row-switched states have been known to exist in underdamped arrays for several years. In this section we review some of those results, and provide some preliminary studies of the ordering of row-switching events. Though the position of these steps is independent of the strength of self-fields, it will be shown below that the inter-row phase-locking of switched rows is affected by strong self-fields. This is an important result because any reduction in the overall phase-locking of the junctions will increase the line-width and reduce the power of the output high frequency rf signal. To build effective devices it is important to find a parameter range where the inter-row phase locking is maximized.

5.1.1 Experiments

In this chapter, measurements from sample H3 are presented. This sample is a 7×7 array, with uniform current injection. It has voltage pads on every superconducting island on the right edge of the array. This array design allows us to measure the voltage across any combination of rows. By varying the temperature we can change the junction parameters from $15 < \beta_c < 60$ and $0.3 < \lambda_\perp < 1.2$. The experimental techniques and equipment are described in previous chapters.

Figure 5-1 shows typical measured data for row-switched steps for sample H3 at a temperature of 6.0 K. At each recorded I–V the amplitude of the sweep current was increased slightly so as to allow retracing of each row-switched step and record the typically hysteretic behavior of these underdamped arrays. The data is normalized to seven times the measured array gap voltage. This measured array gap voltage corresponds to seven times the predicted individual junction temperature dependent gap. As expected, there are seven row-switched steps corresponding to each of the individual rows switching. No flux-flow region is observed at this temperature. This is due to a combination of a small applied magnetic field and the large subgap resistance. The small field produces a very small flux-flow resistance. Furthermore, since β_c is proportional to the square of the effective resistance, it is going to be the square of

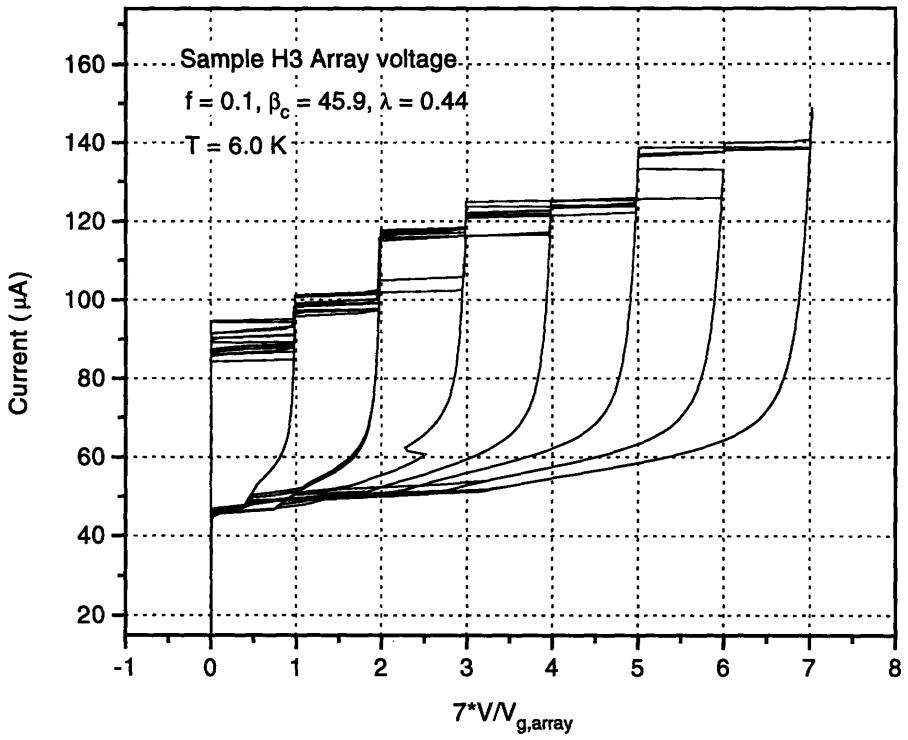

Figure 5-1: Row-switched steps measured by slowing stepping the amplitude of sweep current. Data recorded at 6.0 K and $f = 0.1$.

the large subgap resistance. Thereby β_c is very large and as shown in the previous chapter the flux-flow resistance will be very small because of the losses due to spin-wave damping. Hence no flux-flow slope is expected at temperatures.

Row-switched behavior was observed in sample H3 for $40 < \beta_c < 60$ and $0.5 < \lambda_\perp < 0.3$. Van der Zant *et al.* [38] have also observed row-switched steps in underdamped aluminum arrays. In those measurements, $\lambda_\perp$ was large enough so that self-induced fields could be neglected. Several arrays were measured with β_c's ranging from 7 to 2000. In the classical arrays, where the Josephson energy is much greater that the capacitive energy needed to tunnel, row-switched behavior was observed. It can be concluded from these measurements that there is no β_c or $\lambda_\perp$ dependence of the position of the row-switched steps, but instead only a dependence on temperature through the temperature dependence of the gap.

Having studied the step locations in the array I–V , it is natural to ask if there are any spatial patterns in the switching of rows. By concurrently measuring the

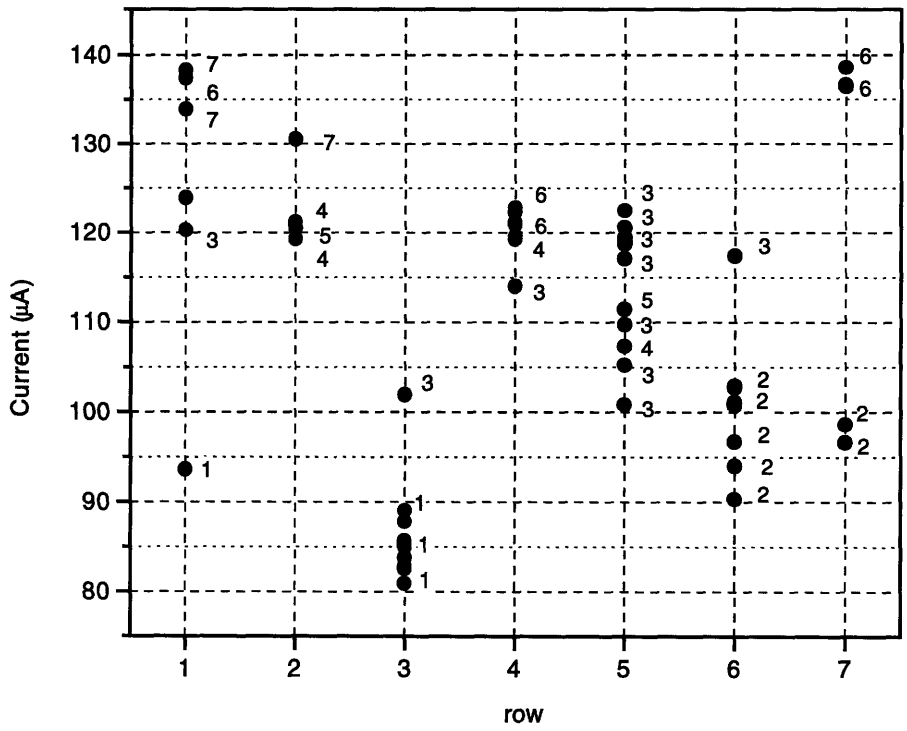

Figure 5-2: Order of row-switching steps. Each dot represents the current value when the indicated row switched. The numbers indicate the corresponding step number in the total I–V of the array. Data recorded at 6.0 K and $f = 0.1$.

voltage across the whole array and the voltage across an individual row, it is possible to deduce at what voltage step a row will switch. If we repeat the measurement for all seven rows of sample H3, we can map the current values that individual rows switched and the corresponding voltage step in the array I–V.

In Fig. 5-2 each dot marks the current value a row switches and the number indicates the sequential order that that row switched. Each dot represents one simultaneous I–V measurement of the total array voltage and the corresponding row voltage. Therefore, Fig. 5-2 is the result of about 50 I–V's and represents a statistical measure of the order of row switching.

In general, there is no definite switching order and a single row may correspond to several different voltage steps in different measurement runs. For instance, row three switched first in all but one measurement, when it was the third row. Statistically we can infer that the third row is likely to switch first, followed by the sixth row. The first and last rows are most likely to switch last.

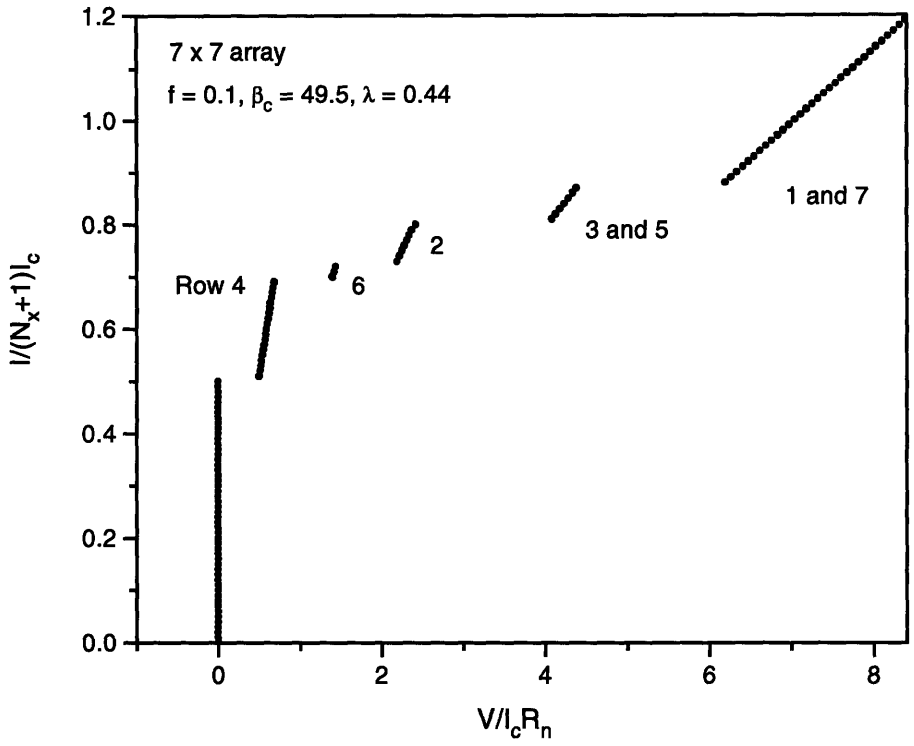

Figure 5-3: Simulated I–V with $\lambda_\perp = 0.44$ and $\beta_c = 49.5$, the critical currents in the simulations had a uniform random distribution of 10%.

Though it is generally believed that the order of row switching is related exclusively to nonhomogeneity of critical currents in the array, it has never been shown experimentally. From this preliminary study, it is clear that there are some edge effects and symmetry in this switching. These effects are probably inherent to the array dynamics but may depend weakly on the applied field, $\lambda_\perp$, or other array parameters as well as the array uniformity of critical currents.

5.1.2 Comparison to simulation

Simulations for both $\lambda_\perp = \infty$ and finite $\lambda_\perp$ show row-switching behavior. Typically for homogeneous arrays where the critical current of every junction is the same, row switching is symmetric about the center row. Since all rows other than the center row switch in pairs, it is impossible to see every expected step in the I–V.

Introducing disorder in the simulations by varying the critical currents of the junctions breaks this symmetry, and rows begin to switch individually. Fig. 5-3

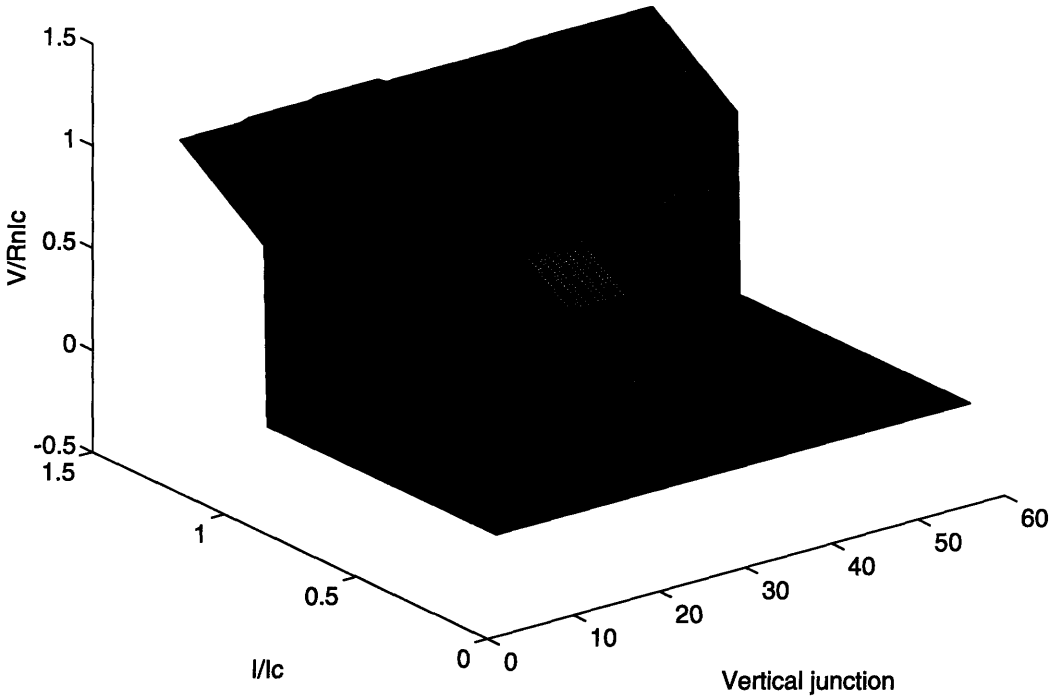

Figure 5-4: Simulated I–V of each vertical junction with $\lambda_\perp = 0.44$ and $\beta_c = 49.5$.

shows a simulated $I - V$ with the same parameters as Fig. 5-1 and a 10% uniformly distributed random variation of the critical currents. The first step corresponds to the switching of the center row while the second smaller step correspond to the switching of row six. Afterwards, row two switches, and this symmetric step is stable for a larger range of current biases until rows three and five switch simultaneously and finally the two rows on the edges switch. This type of ordering of the rows is similar to what was observed in the experiments.

Fig. 5-4 further demonstrates the spatial dynamics of row-switching. In the figure, the I–V of every vertical junction is plotted. Row one contains junctions one through eight. Row two is represented by junctions nine through sixteen and similarly for all other rows. In this parameter range, where the array I–V has no flux-flow state, every junction is either in its superconducting state or in the normal state.

The simulations do not include a subgap resistance; hence when a row switches it will switch to the IR_n part of the $I - V$. However, since the critical currents are

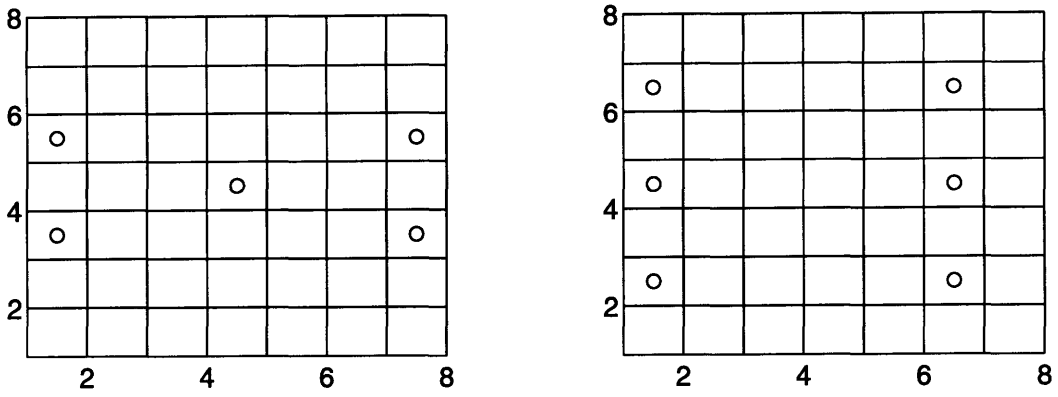

Figure 5-5: Instantaneous vortex configurations for 7×7 arrays with three rows switched. Left graph is $\lambda_\perp = 0.44$ and the vortices in the rows are out of phase, while the graph on the right for $\lambda_\perp = \infty$ and all the vortices in the rows are in phase.

randomly distributed but the $I_c R_n$ product of all the junctions is constant, the R_n of individual junctions is also randomly distributed in the same way as the junction's critical currents. Nonetheless, at a row switched state all the junctions in a switched row have the same I–V characteristic. This is a collective effect of a row. It can phase-lock all the junctions such that they are oscillating at the same frequency even in the presence of inhomogeneities.

In the actual experiments, the temperature is sufficiently low that there is a very large subgap resistance. If we include this subgap resistance in the simulations, then the resistive steps would have a steeper slope and the simulations would be almost indistinguishable from the experimental data [26].

The two-dimensional nature of these arrays provides for two types of phase-locking mechanism: intra-row, and inter-row. The locking between junctions in a row, inter-row phase-locking, is determined mostly by the flux quantization condition and appears very robust in both the simulations and experiments. The inter-row phase-locking appears to be much weaker. It is in the interaction between rows that self-fields play an important role. In essence, strong self-fields tend to disturb the phase locking between switched rows.

Fig. 5-5 shows the instantaneous vortex configuration for an array with three rows switched. The vortex location is defined in terms of the loop sum of the gauge invariant phases as in [27, 35]. Vortices only move through the switched rows. These

vortices provide the strong coupling need for the junctions in a row to be phase-locked. The other rows have no voltage associated with them. For $\lambda_\perp = \infty$, switched rows are in phase and vortices travel across the array in columns. As $\lambda_\perp < 1$ the in-phase stability of the rows begins to weaken, and vortices no longer travel through the switched rows in columns. The in-phase stability of the inter-row vortex configuration appears to weaken from the $\lambda_\perp = \infty$ as $\lambda_\perp$ becomes smaller than 1. It is possible that there is an optimum $\lambda_\perp$ value that maximizes the ability of rows to phase locked, or it may be that maximum phase-locking occurs at the $\lambda_\perp = \infty$ limit.

To get a better understanding of the behavior of the junctions we can plot their phase portrait. Fig 5-6 shows the phase portrait of a vertical, (b) and (d), and horizontal, (a) and (c), junction in an active row for both the beginning, (c) and (d), and top, (a) and (b), of a step. The first obvious conclusion is that the junctions are behaving periodically. The vertical junctions rotate in an almost sinusoidal way and their average value is the measured junction voltage. In contrast, the horizontal junctions librate around a fixed point of zero voltage and a small negative phase. Their librating magnitude is four orders smaller than the vertical junctions. This implies that the horizontal junctions conduct a small dc current. We can conjecture that the row-switched state is a periodic solution of the governing equations. The non-linearity of the horizontal junctions is probably important in the coupling of rows though their librations seem almost negligible. Since the horizontal junctions virtually have zero phase, the flux quantization condition, $M\phi = -\Phi^m$, will strongly couple the vertical junctions of the row and may account for the robustness of the intra-row phase-locking.

Fig. 5-7 shows the phase portrait of a vertical and a horizontal junction of non switched-rows in the array. We can draw similar inferences as above. Like in the row-switched states, horizontal junctions librate at very small amplitudes around a fixed point of zero voltage and a small positive phase. The same can be said for the vertical junction, though the vertical junction supports much more current. Most of the applied current will flow through the vertical junctions, but there is a small circulating current in the horizontal junctions. From the simulations, it is difficult to

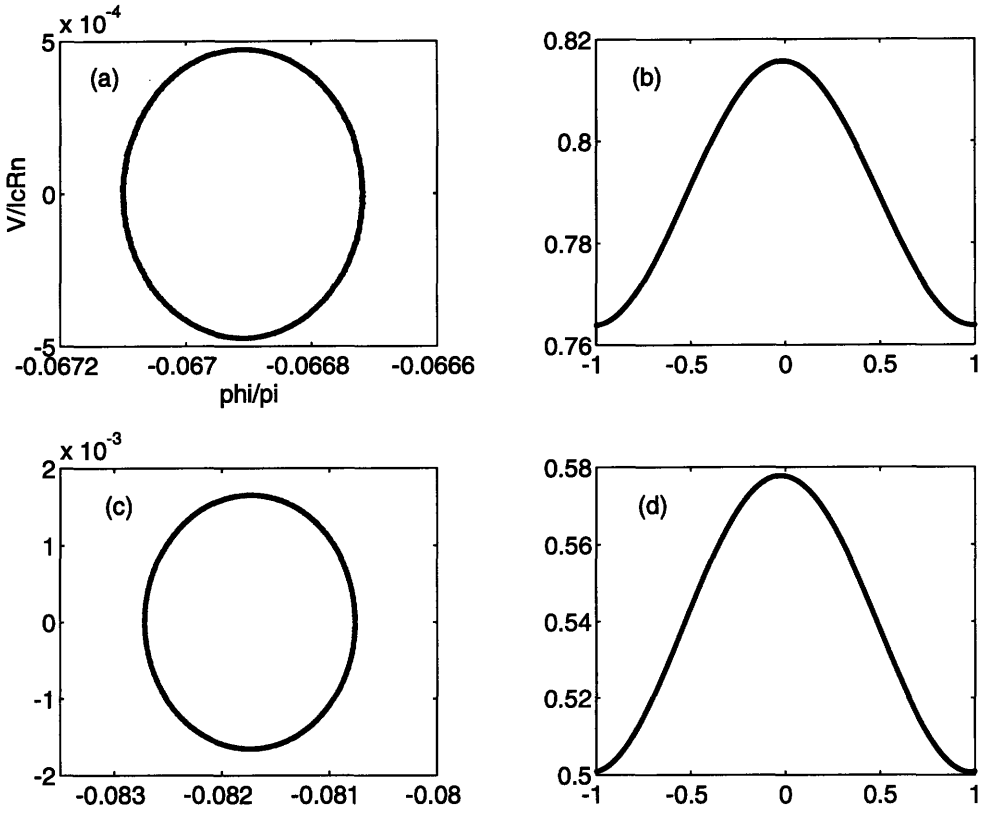

Figure 5-6: Phase portrait of a horizontal and vertical junction in an active row of the array. Graphs (a) and (c) depict the the first horizontal junction in row four on the right side of the array. While the graphs (b) and (d) are for the first vertical junction on row four of the right side of the array. Bottom graphs show the dynamics at the beginning of the step, and top graphs at the top of the step.

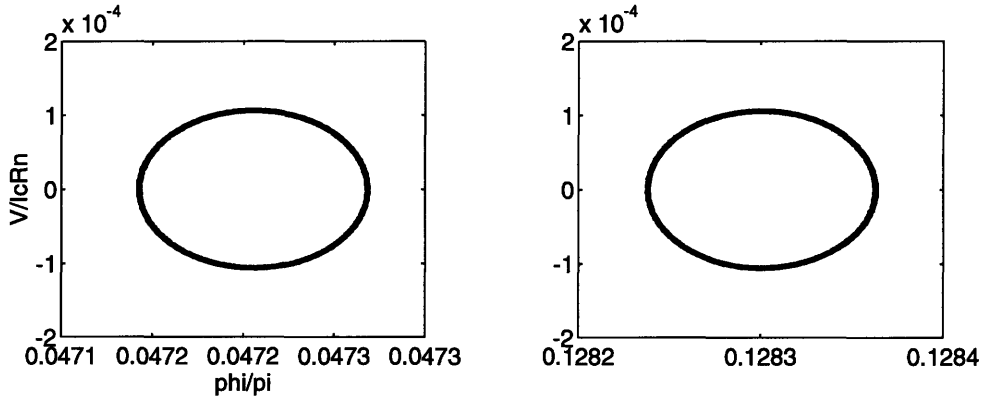

Figure 5-7: Phase portrait of a horizontal and vertical junction in a quiet row of the array. The graph on the left depicts the first horizontal junction in the first row of the left side of the array. While the graph on the right shows the first vertical junction on the first row of the left side of the array.

discern any patterns of the small horizontal current flows.

5.1.3 Conclusions

Several qualitative conclusions can be drawn from both simulations and experiments. Row-switching steps are related to coherent oscillations of individual rows. Once a row is switched it behaves as if it were a single junction that has jumped to its gap. Therefore, these voltage steps only depend on temperature in the same way that the junction gap depends on temperature. The location of the steps is independent of $\lambda_\perp$ and β_c.

However, there is a $\lambda_\perp$ dependence; strong self-fields disturb the phase-locking between switched rows, inter-row coupling. Once a row has switched it will remain in that state and different steps in the I–V correspond to the switching of more rows. Center rows tend to switch first, while rows near the edges are the last to be triggered.

The dynamics of horizontal junctions and vertical junctions of quiescent rows are very similar. They both have very small librations. Vertical junctions of switched-rows rotate periodically and all other junctions just support small currents with small parametric effects. The nature of the inter-row coupling is not fully understood, and needs further study.

5.2 Array resonances

In this section we report preliminary findings of novel resonant steps present in all the measured H samples. These steps are fundamentally different from the row-switched steps and seem to depend on both self-fields and horizontal cross junctions for their existence.

5.2.1 Experiments

The distinguishing feature of these steps is the temperature independence of the position of the step voltage as shown in Fig. 5-8. The step is located at $V \sim 2\,\mathrm{mV}$

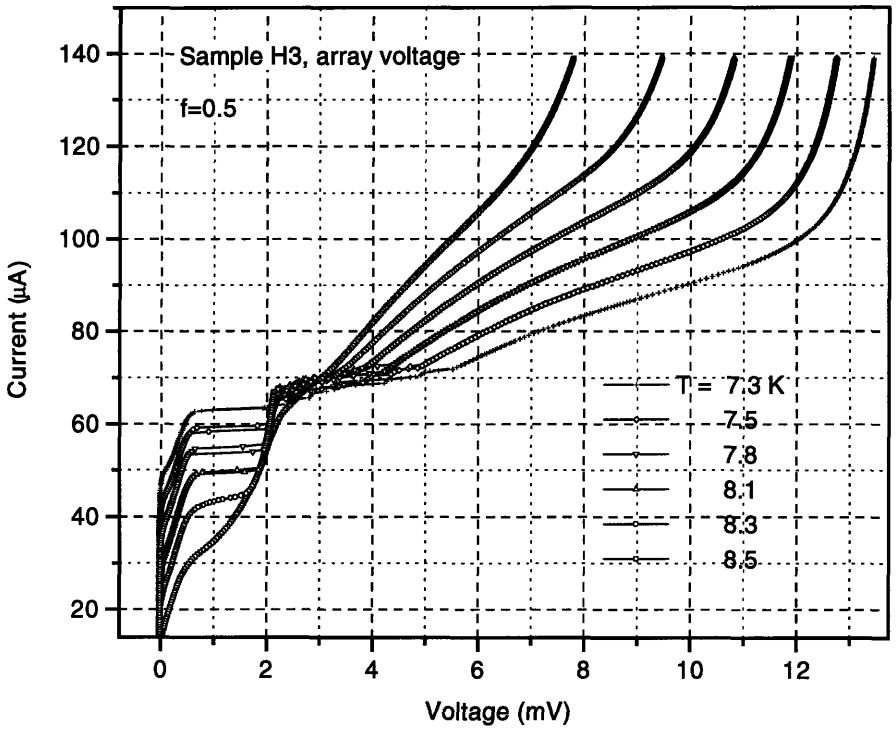

Figure 5-8: Temperature dependence of resonant step at $f = 0.5$. The step is located at $\sim 2\,\mathrm{mV}$, and the gap is shown in the upper right-hand corner as it varies with temperature.

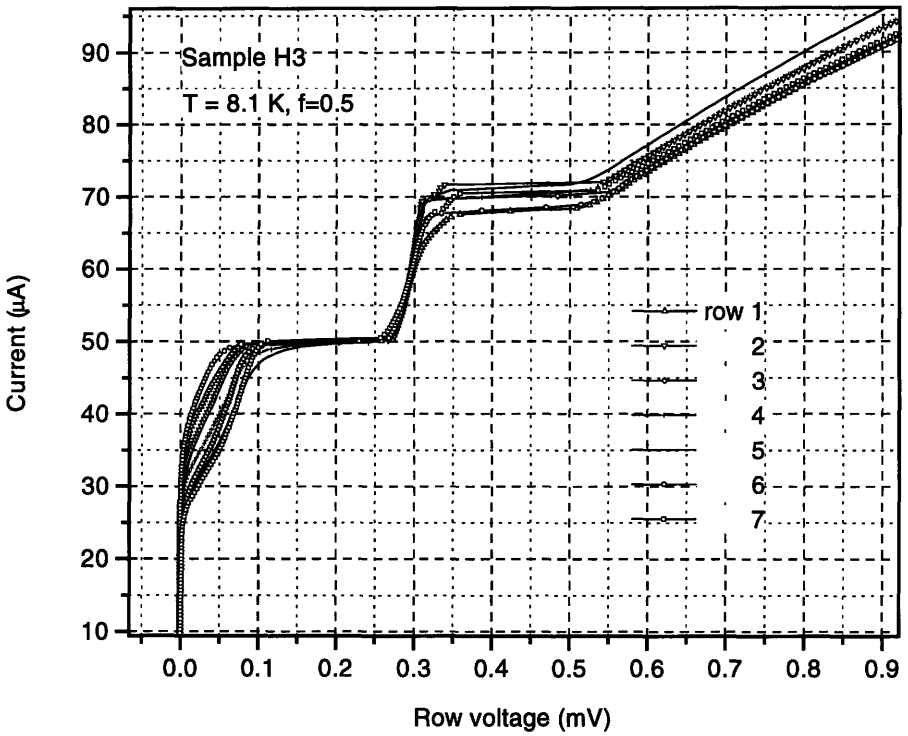

Figure 5-9: Measured I–V's of each individual row showing resonant step at $T = 8.1\,\mathrm{K}$ and $f = 0.5$.

and the gap can be seen to vary with temperature at the right of the figure. It is evident that the step height varies with temperature, but the step location remains constant in terms of voltage. The depinning current and flux-flow regions vary in accordance with the material presented in earlier chapters.

Since these steps are not dependent on the gap, they become fundamentally different from the row-switched steps. This also implies that these steps originate from geometric resonances of the array since the array geometry is naturally temperature independent.

Though the step was observed for the three H samples, only measurements for the H3 sample will be presented. This sample allowed a detailed study of the dynamics of the array because measurement of the I–V characteristic of each individual row was possible. Fig. 5-9 shows the measured $I-V$'s for each row in the array. We can deduce that all the rows are oscillating at the same frequency and this step corresponds to a coherent motion of vortices throughout every row of the array. Notice that edge

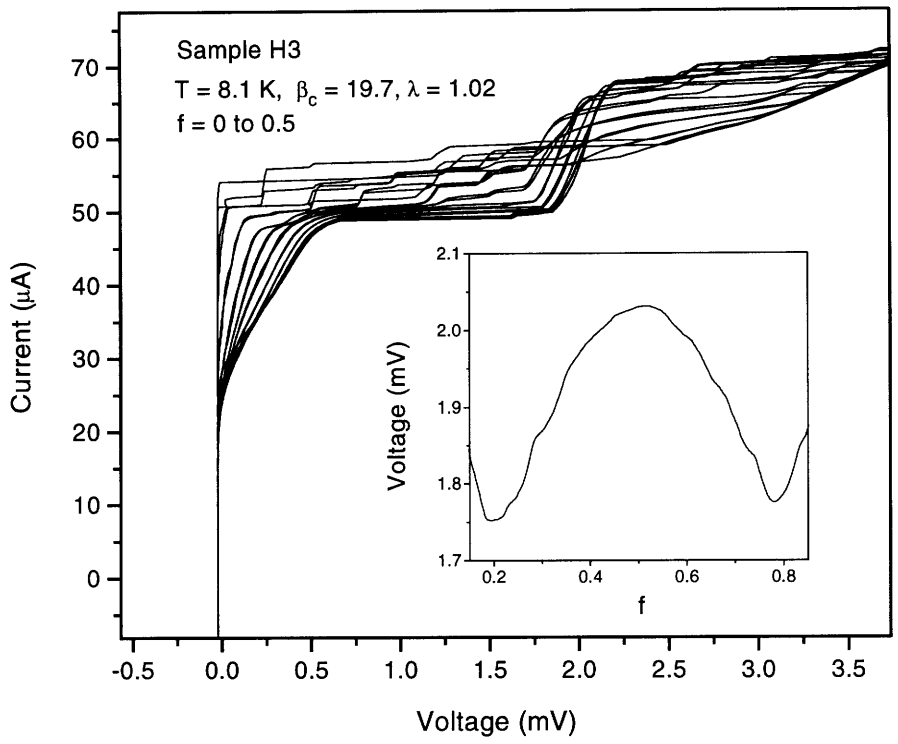

Figure 5-10: Measured I-V's vs. applied magnetic field at $T = 8.1$ K. Inset: Measured voltage vs. applied field at the same parameters at a current bias of 58 μA

effects are very visible in the flux-flow region but only affect the resonant step at its top, just before switching to the subgap resistance. There clearly is a large current range where every row of the array is oscillating at exactly the frequency.

The magnetic field dependence of the step is shown in Fig. 5-10. There is an f dependence on the large resonant step. To quantify the magnetic field dependence of this step we biased the array at its center and continuously varied the applied field while measuring the output voltage. The inset of Fig. 5-10 shows the result. In the region $0.2 < f < 0.8$, the f dependence seems sinusoidal with some subtle substructure. As the step changes position with respect to its voltage its height is also changing. For $f < 0.2$ the step disappears and the array is now biased at the subgap resistance.

At $f = 0.2$, a sequence of I-V was measured for every row. The step was still clearly visible. However, only the five middle rows had the same voltage and therefore were oscillating at the same frequency. The outer two rows, one and seven, had a

slightly higher voltage. It is important to note that the resonance is not a consequence of the special symmetry at $f = 0.5$, but appears for a large range of frustration.

As shown in Fig. 5-10, other steps become visible as f is varied. The nature of these smaller steps has not been studied yet, but it seems possible that there are other resonant modes in the array just as in one-dimensional arrays there are different resonant Fiske steps.

In summary, this novel step may be a geometric resonance because its position is independent of temperature. However, the step is more than just a standing wave mode in the array because it has a magnetic field dependence. At $f = 0.5$, the step correspond to coherent oscillations of all the vertical junctions in the array. As f is lowered only the center rows oscillate coherently, while the two outer rows begin to oscillate at a different voltage.

5.2.2 Comparison to simulation

To get a better understanding of the dynamics of this resonant step, simulations were performed and compared to the measurements. These simulations produce a resonance step with properties that agree well with the measurements. In contrast to the row-switching states, it appears as though self-fields and the horizontal junctions are crucial to the formation of the step.

Fig. 5-11 compares two $I - V$'s with different $\lambda_\perp$'s. The circles represent a simulation with the same junction parameters as in Fig. 5-10 at $f = 0.5$ while the dots correspond to an $I - V$ with the same parameters except $\lambda_\perp = \infty$. The difference in I_{dep} can be explained in terms of the increase of the cell-to-cell energy barrier for a vortex. The difference of the flux-flow slope can be explained in terms of the reduced viscosity of a small $\lambda_\perp$. There are no row switching events in the $I - V$ for $\lambda_\perp = \infty$ because the applied field of $f = 0.5$ injects enough vortices in the array so that the first step has all of its rows switched. On the other hand, for the $\lambda_\perp = 1.02$ there is a large voltage step. This step has been observed in the simulations for $\lambda_\perp$ as large as 2, but no detail study has been performed. Fig. 5-12 shows the $I - V$ characteristics of all the vertical junctions of the array. This step clearly represents

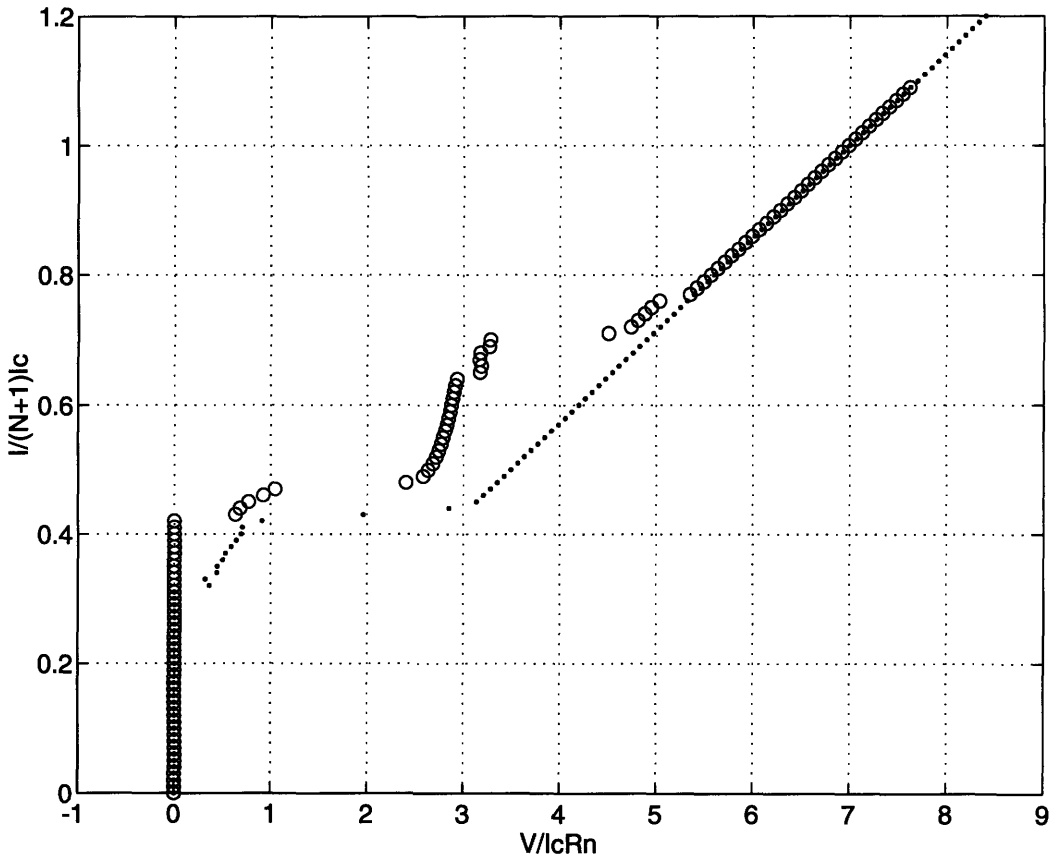

Figure 5-11: Simulated I–V's comparing $\lambda_\perp$ dependence of the resonant step at $f = 0.5$ and $\beta_c = 19.7$ for a 7×7 array. Dots represent an I–V with $\lambda_\perp = \infty$, while circles have a $\lambda_\perp = 1.02$. Though there are no resonances for the $\lambda_\perp = \infty$ a clear step is seen at $\lambda_\perp = 1.02$.

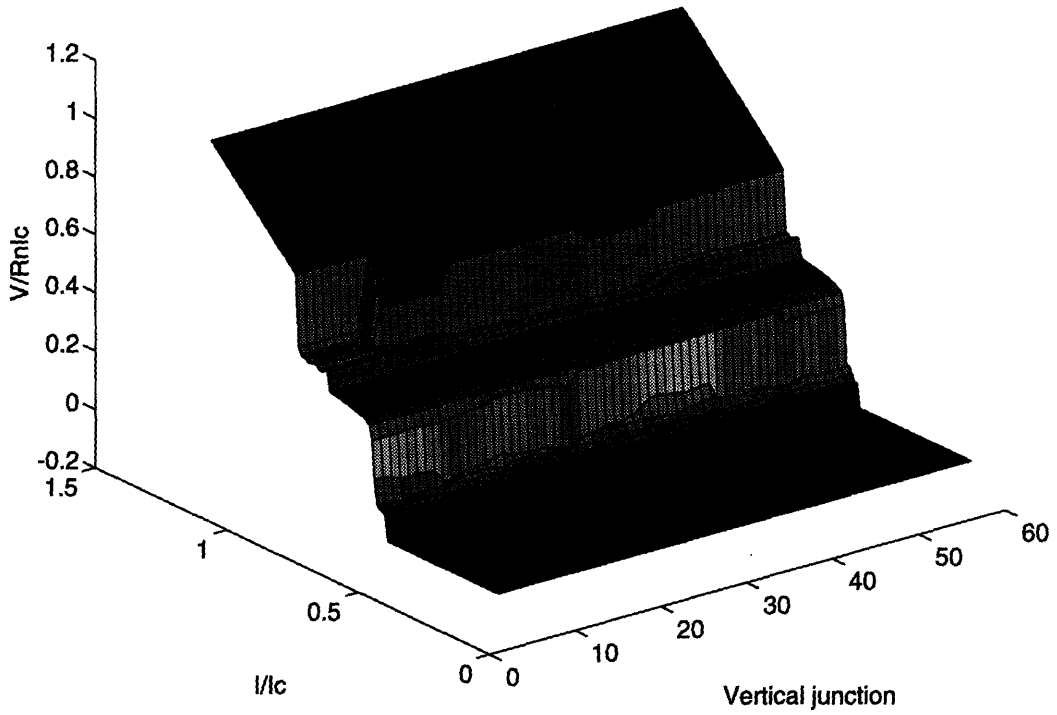

Figure 5-12: Simulated I–V of each vertical junction with $\lambda_\perp = 1.02$, $\beta_c = 19.7$, and $f = 0.5$.

coherent oscillations of all the vertical junctions. These simulations agree very well with the measurements. In terms of $I_c R_n$, the resonant step was measured at ~ 3.5, qualitatively similar to the simulations value of 2.9.

A sequence of I–V's was calculated to determine if there is a similar magnetic field dependence. Fig. 5-13 shows the I–V's for $f = 0.5, 0.4$ and 0.3. Similar to the measurements, there is a slight f dependence: as the magnetic field is decreased the step voltage is decreased. Also the step height is reduced and more structure is seen in the I–V as the magnetic field is decreased.

Since all of the vertical junctions seem to be oscillating coherently at the same frequency, it is natural to ask if the rows can be decoupled. For instance, in the row-switched steps, the dynamics could be interpreted in terms of independent rows where the vertical junctions of a row were either oscillating or quiet.

To answer that question, a series of I–V's was performed for a 7×1 ladder array.

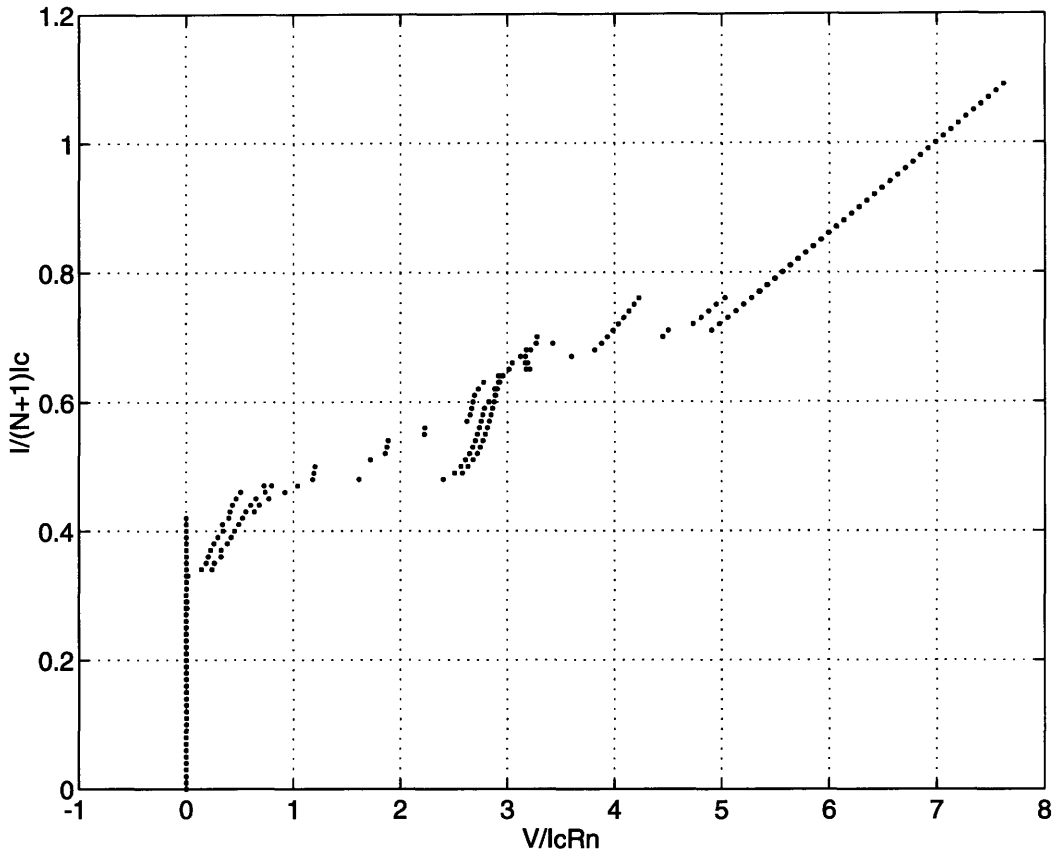

Figure 5-13: Simulated I–V 's comparing f dependence of resonant step at $\lambda_\perp = 1.02$ and $\beta_c = 19.7$ for $f = 0.5, 0.4$ and 0.3.

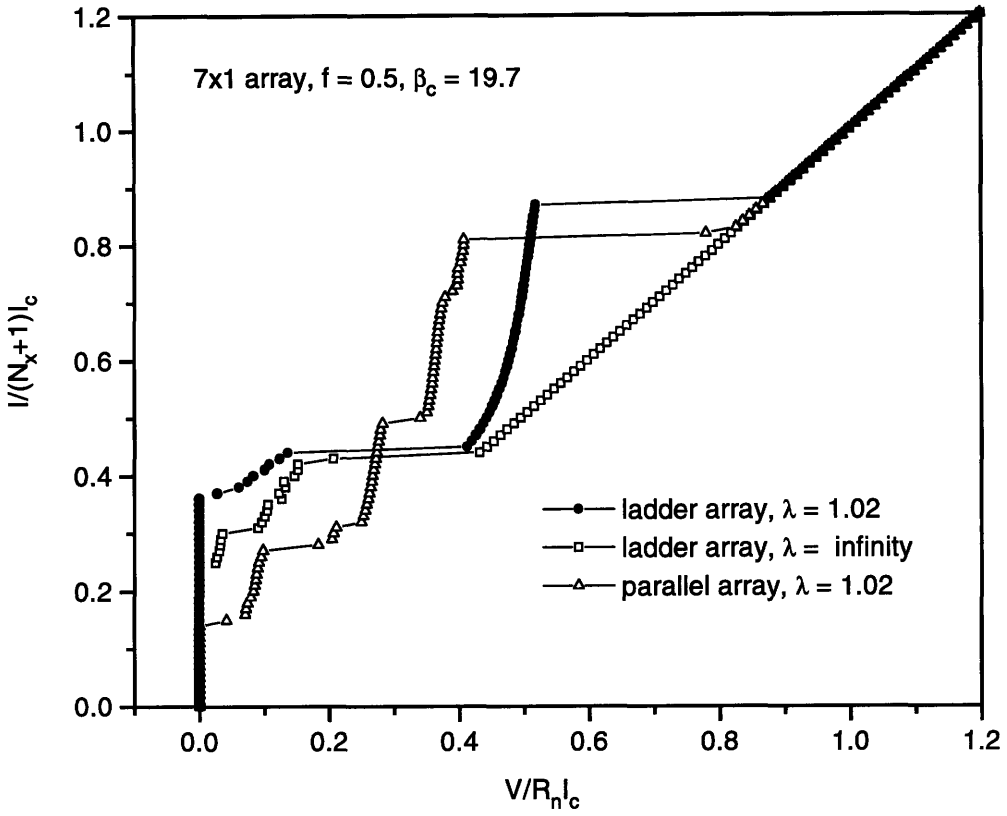

Figure 5-14: Simulated *I–V* 's for 7×1 ladder and parallel array comparing dependence of the step at $f = 0.5$ and $\beta_c = 19.7$.

For comparison, a simulation was also performed for a 7×1 parallel array. The difference in geometry between a parallel array and a ladder array is that the former has junctions in the horizontal links while the latter has superconducting wires. The *I–V* denoted by the solid circle in Fig. 5-14 is a simulation for a 7×1 ladder array with $f = 0.5$ and $\beta_c = 19.7$ and $\lambda_\perp = 1.02$. The open squares represent an *I–V* with the same parameters and geometry except with $\lambda_\perp = \infty$. The diamonds are an *I–V* for a parallel array with the same parameters.

These *I–V* 's are essentially one row of the two-dimensional array. A large resonant step appears for the finite $\lambda_\perp$ but it is not present when self-fields are neglected. The same conclusion can be reached as when the full 7×7 array was simulated: self-fields are necessary to produce the resonant step. We can also deduce that these resonances are not due to the coupling of rows, since it appears in a one-dimensional ladder array.

To further investigate the mechanisms of the step we can compare the *I–V* to a

7×1 parallel array. Fig. 5-14 shows this comparisons. As expected, the array without cross junctions (diamonds) behaves as a discrete long Josephson junction. We see the general I–V structure of this type of geometry including the several Fiske steps. On the other hand, when cross junctions are included in the array (solid circles), the $I-V$ characteristics change substantially. The depinning current is increased and there are no visible Fiske steps, and only the large resonant step appears. A slight f dependence was observed in the 7×1 ladder array, but a more detailed study is needed to verify if the experimentally measured f dependence is due to the coupling between rows, or can be attributed solely to the dynamics of a ladder array.

Since it appears the the cross junctions are important in the dynamics of this step, a phase portrait of both a vertical and horizontal junction in the middle row of the 7×7 array is plotted in Fig. 5-15. The vertical junctions are graphs (b) and (d) while the horizontal ones are graphs (a) and (c). The beginning of the step is plotted on the bottom two graphs while the top of the step, just before the jump to the normal state, is plotted on the top two graphs.

We see that at the beginning of the step, the solution for both the vertical and horizontal appears to have more than one frequency, and it is not periodic. At the top of the step the horizontal junctions librates periodically and the vertical junctions rotate nonuniformly. It appears as though all of the fast oscillations decay away and only the dominant slower frequency remains as the current is increased through the step. Also the horizontal junctions are librating at a fairly large amplitude, almost of the same order as the vertical junctions, and they support a small horizontal current. Though it seems possible to characterize this horizontal current flow, it does not appear trivial in the simulations. Some rows have half the horizontal junctions flowing in one direction and the other half flowing in the opposite, while other rows have some junctions that support no current. For the 7×1 ladder array the behavior is very similar, vertical junctions rotate with an average voltage and horizontal junctions librate at almost the same magnitude voltage.

The simulations very closely match the experimental measurements and provide a tool for further study of the dynamics of this resonant step.

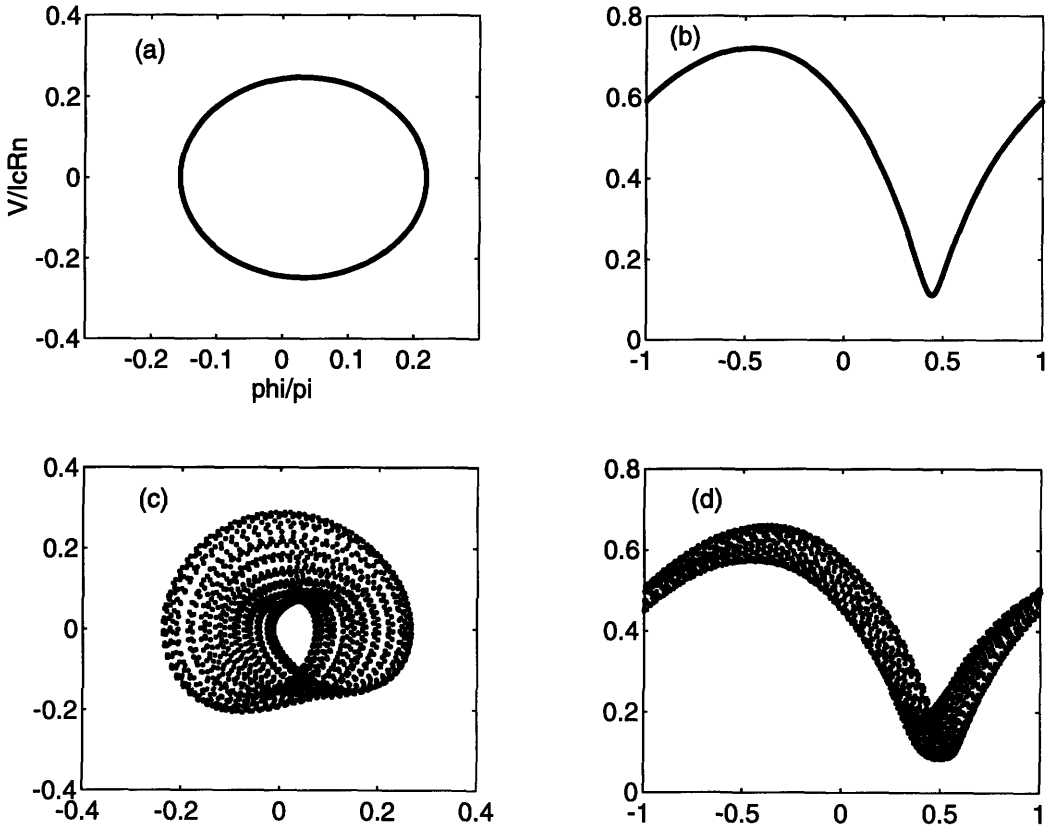

Figure 5-15: Graphs (a) and (c) phase portraits of the first horizontal junction in row four on the right side of 7×7 array. While (b) and (d) are for the first vertical junction on row four of the right side of the array. Bottom graphs show the dynamics at the beginning of the step, and top graphs at the top of the step.

5.2.3 Conclusions

A resonant step has been observed in the I–V characteristics of several arrays that, among other possible factors, would not exist without induced self-fields. These steps are independent of temperature, therefore they are geometric resonances of the array. At $f = 0.5$, the step correspond to coherent oscillations of all the vertical junctions of the array. A magnetic field dependence was observed for both the height and voltage location of the step hinting that the steps are more than just standing wave modes in the array.

From the simulations it has been shown that the resonant step requires at least a self-inductance in the governing equations and so self-fields are important. It has also been shown that the step is not a fundamentally two-dimensional phenomenon since it appears in 7×1 ladder arrays, though it is possible that the magnetic field dependence might be due to the coupling of rows. Also, the nonlinearity of horizontal junctions appear to provide a parametric inductance that is crucial in the dynamics of the step. Without the horizontal junctions the step does not form. Further research is needed to determine the full dynamics of these resonant steps.

Chapter 6

Conclusions

6.1 Summary

The role of self-induced fields in two-dimensional arrays of Josephson junctions has been studied in both simulations and experiments.

Several different arrays were fabricated using a Nb-Al_2O_x-Nb trilayer process with critical currents ranging from 100 to 7000 A/cm^2. Along with varying the critical currents, it was possible to change the area of the junction and the lattice spacing of the array. This allowed for a large experimental exploration of the parameter space. The range of $\lambda_\perp$ was between 0.17 to 5 and β_c ranged between 2 and 400. Most of the arrays were 15×15, but a 47×47 and 7×7 array were also measured. The small size allowed for comparison to simulation and for the measurement of individual rows in the array.

The experiments focus on the dc current-voltage, *I–V* , characteristics of the array. Though these electrical properties are averaged both in space and time, the dynamics of the array can be inferred. In this thesis the experiments have been classified into four regions of the dc I–V curve: the superconducting state, the flux-flow regime, row-switching events, and resonant steps.

For the superconducting state, it was found that strong self-fields increase the energy barrier of vortex motion. It was also found that strong self-fields reduce the ability of vortices to from a commensurate states with the array and thereby make

the depinning current independent of the applied field.

In the flux-flow region, it was found that self-fields reduce the mass of the vortex. This is equivalent to a reduction of the array viscosity coefficient. The effect can be explained terms of the localization of the vortex. The dissipation of a vortex is proportional to the number of resistors that it encloses. The stronger the self-fields, the smaller the vortex becomes and the smaller the number of resistors it must travel through. This decrease of the dissipation results in an increased flux-flow resistance.

The localized vortex picture was found to adequately explained most of the observation in both the superconducting state and the flux-flow region. Deviations from this phenomenological theory were found, but the overall effects of self-fields observed in both simulation and experiments can be accounted for.

In the flux-flow region, the most interesting deviation was the spatial structure in the small arrays. It was found that rows have different flux-flow slopes. This may be accounted for by a combination of edge effects and disorder of the array.

In the row-switching state the vortex as a particle picture can no longer be used. Instead entire rows of the array oscillate coherently at the temperature dependent gap voltage of a single junction. It was found that self-fields affect the coupling between rows. Strong self-fields seem to destroy this coupling. Also it was found that there is some symmetry in the ordering of row switching. In the simulations this symmetry exists even in the presence of disorder of the critical currents of the junctions. Horizontal junctions play a role in the dynamical formation of a row-switched states, but their voltages are orders of magnitude smaller than the vertical junctions.

A new type of resonant step was observed at temperature close to T_c. It was measured for a range of applied fields, and at $f = 0.5$ it corresponds to coherent oscillations of all the junctions of the array. From simulations, it was deduced that the step differs from row-switched states in that self-fields are essential to its formation. Another difference is that horizontal junctions have voltages that are of the same order of magnitude as the vertical junctions.

In summary, self-fields are important in niobium arrays where the penetration

depth can be of the order of a cell size. These effects can be accurately modeled in simulations by taking into account all of the inductive interactions between cells.

6.2 Future directions

There are many theoretical as well as experimental unanswered questions that remain to be explored.

In the superconducting state, the ground state formation for $\lambda_\perp = \infty$ is well understood. It is not known how the ground states change as self-fields become important. Also the mechanism that affect vortex depinning through the edges are not well understood.

In the flux-flow regime, the simulation and measurements show fine structure that may be due to the small array size. These type of discreteness effects could lead to further understanding of vortex motion in two-dimensional discrete system. The essential question is how relevant is the vortex picture in the presence of discreteness. Also, it would be interesting to investigate how edges affect two-dimensional vortices.

It is generally assumed that the flow-flow state ceases to exist when a vortex reaches a limiting velocity. There is evidence that instead that the creation of other stable states, such as a row-switched states, limit the span of the flux-flow. The question of how the flux-flow state becomes unstabilized remains open.

The most pressing issue in the row-switched regime is the determination of the inter-row coupling mechanism. It is hoped that this mechanism is related to the dynamics of Josephson series arrays, but may instead be an intrinsic mechanism in the two-dimensional system. Another issue of interest is the determination of the ordering of switching events and how they depend on the array dynamics and disorder. Understanding how arrays behave in the presence of disorder is important in future device applications.

On the experimental side, it would be interesting to measure the line-widths of the row-switched states versus the junction parameters. This would provide a direct measure of the phase-locking strength of the state. Understanding the phase-locking

mechanism of two-dimensional arrays is important if they are ever to become viable as high frequency devices.

A new type of resonant step was found. Horizontal junctions as well as self-induced fields play an important role in the dynamics of the step. It would be interesting to determine the physical mechanisms. There is also no current theory of the magnetic dependence of the step. Since the step appears in ladder arrays, it may provide more insights into the cross-over from one-dimensional to two-dimensional Josephson systems.

Experimentally, it would be exciting to find other resonant steps and to map out the dependence on applied field and temperature.

If low temperature Josephson technology is going to produce a marketable device it will be made with niobium junctions because of their high critical temperature and their electrical and thermal stability. Self-induced fields play a major role in the dynamics of arrays of niobium junctions and their effects can not be neglected.

Appendix A

Published papers

The following published paper is summarized in this thesis:

E. Trías, J.R. Phillips, H.S.J. van der Zant, and T.P. Orlando, "Self-field Effects in Two-dimensional Nb Josephson-junction Arrays," Appl. Supercond. Conf., Boston 1994; to appear in *IEEE Trans. Appl. Supercond.,* Sept. 1995.

Self-field Effects in Two-dimensional Nb Josephson-junction Arrays

E. Trías, J.R. Phillips, H.S.J. van der Zant and T.P. Orlando
Massachusetts Institute of Technology, Cambridge, MA 02139

Abstract—**We have measured two-dimensional niobium Josephson junction arrays in which self induced fields are important. We find an increase of the depinning current when $\lambda_\perp$, the penetration depth in the array, is of the order of one. There is evidence for a destruction of commensurate vortex states in the arrays as the depinning current becomes almost independent of the applied magnetic field. Our data also show that self-field effects change the array flux-flow dynamics and decrease the effective array viscosity.**

I. Introduction

There is a long standing interest in Josephson devices as microwave sources in the millimeter and submillimeter range. Two-dimensional arrays of Josephson junctions are of particular importance because by phase locking, they overcome the problems of low impedances and power when using single junctions. For example, an array with N cells perpendicular to the current direction and M parallel, the phase-locking of the array implies the power delivered to a load scales with $M(N+1)$ and at the same time the linewidth with $1/M(N+1)$. Coherent emission and power levels in the microwatt range have been detected [1] in niobium arrays with 9 by 10 cells. In that paper it was suggested that the 2D array itself might provide a mechanism for phase locking through quasi-long-range interactions between its junctions.

Generally speaking, the delivered power is proportional to the critical current i_c so that the demand of high power stipulates the use of junctions with large critical currents. High critical currents, however, may destroy the internal locking mechanism in the arrays [2], [3]. In 2D arrays, the penetration depth for perpendicular applied magnetic fields, $\lambda_\perp$, is inversely proportional to i_c. A small $\lambda_\perp$ weakens the range of the vortex interactions thereby reducing the the ability of the whole array to mutually phase lock. Clearly, an engineering compromise must be made for optimal performance.

Manuscript received October 18, 1994.

E. Trías, e-mail etrias@mit.edu, phone 617-253-4213;

This work was supported in part by the National Science Foundation under Grant DMR-9402020 and a Graduate Research Fellowship; and in part by Advanced Research Projects Agency through the Consortium for Superconducting Electronics. We thank MIT Lincoln Laboratory for fabricating our samples.

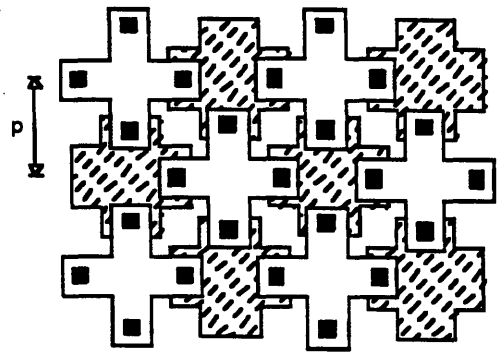

Fig. 1. Geometry of two-dimensional Josephson-junction array.

Although the effects of self-fields have been calculated for various array properties, there have been no detailed measurements of these effects. In this paper, we present an experimental study of the self-field effects on the depinning currents and the flux-flow resistance in the array. We find that these self-field effects are important in practical niobium arrays which have $\lambda_\perp \sim 1$ and that these effects can be modeled well by numerical simulation.

II. Array Measurements

A total of 5 different arrays were fabricated and measured using a Nb-Al_2O_x-Nb trilayer process with varying critical current densities, J_c. Fig. 1 shows the physical layout of the arrays. The bottom electrode is represented by the hatched islands, the black squares represent both the vias and the etched counterelectrode of the trilayer that form the Josephson junction. These are connected by a metallic layer shown by the unhached islands. We only consider square arrays where every inner island is connected to 4 neighbors. All the arrays have junctions arranged in a 15×15 square matrix, where $N = 15$ is the number of cells on the edge of the array spaced by a lattice spacing of p. Array 1 was fabricated at Hypres Inc. with $J_c = 1000\,\mathrm{A/cm^2}$. Arrays 2-5 were fabricated at MIT Lincoln Laboratory using a DSNAP process. In this paper we report detailed measurements of array 1.

Array 1 consists of $3\times3\,\mu\mathrm{m}^2$ junctions with $p = 16.5\,\mu\mathrm{m}$. By injecting the current through resistors of $0.5\,\Omega$ connected on each island of the top and bottom of

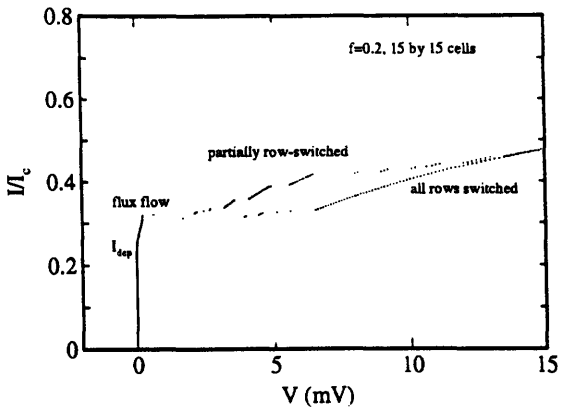

Fig. 2. Typical $I-V$, indicating the depinning current, flux flow region, partially-row switched, and fully row switched states. The data was taken at 7.4K with $\lambda_\perp = 0.73$ and $\beta_c = 46$.

the array, uniformity in bias current was achieved. The voltage was measured between the rightmost islands of the top and bottom row.

The array critical current I_c is defined as $I_c = (N+1)i_c$, where i_c is the critical current of a single junction. The junction normal state resistance, r_n, is determined from the measured array resistance, R_n, at $T \approx 8$K by the relation $r_n = R_n(N+1)/N$. At $T = 0$K the $i_c r_n$ is equal to 1.9mV, so that the junction critical current can be estimated. For array 1, the junction capacitance, C, is 300fF and $R_n = 19.3\Omega$ so that r_n is calculated to be 20.6Ω. From the above values we can estimate $\beta_c = 2\pi R_n^2 C i_c/\Phi_0$ and the dimensionless penetration depth $\lambda_\perp = \Phi_0/2\pi\mu_0 p i_c$. Furthermore, by varying the temperature of the sample we can vary a junction's i_c and hence change its β_c and $\lambda_\perp$ by up to a factor 5 in a controlled way. For array 1, $6 < \beta_c < 30$ and $0.2 < \lambda_\perp < 1$.

A typical current-voltage ($I-V$) is shown in Fig. 2. There are three distinct regions in the $I-V$: a superconducting state at zero voltage, a flux-flow region, and a row-switched region. In this paper we will discuss the depinning current, I_{dep}, that indicates the onset of the flux-flow region and comment on the $\lambda_\perp$ and β_c dependence of the flux-flow resistance region. We define I_{dep} as the current where there first occurs a nonzero voltage across the array. The partially and fully row switched states have been investigated elsewhere [4].

III. Depinning current vs. $\lambda_\perp$

In this section we present a study of the dependence of the depinning current, I_{dep}, with $\lambda_\perp$. An externally applied magnetic field H_0 was used to inject vortices in the array. This field is characterized by the frustration $f = \mu_0 H p^2/\Phi_0$ which measures the fraction of flux quanta, Φ_0, in a cell. Fig. 3 shows I_{dep} for $f = 0.2$ for the various samples of 15×15 cells at various temperatures. We see that the depinning current increases strongly as $\lambda_\perp$ becomes less than 1.

To calculate a depinning current the motion of single vortex is modeled as a damped massive particle moving through a sinusoidal potential of amplitude $\Delta E/2$, with ΔE representing the intrinsic cell-to-cell energy barrier of the array. This equation of motion maps onto the same form as the RCSJ model of a single junction [5], [6] with a critical depinning current $I_{dep} = (\Delta E/2E_j)I_c$, where $E_j = \Phi_0 I_c/2\pi$ is the Josephson energy.

In the limit where $\lambda_\perp$ is larger than the array size, this energy barrier was first calculated by Lobb, Abraham, and Tinkham, (LAT) [7]. They considered the total static Josephson energy of the array when a single vortex is in the middle of a cell and when the vortex is on top of a junction. Since these represent respectively the minimum and maximum energy configurations, their difference is a barrier,ΔE, to vortex motion. The LAT result of $\Delta E = 0.2E_j$ yields an expected $I_{dep} = 0.1I_c$ which has been measured by various groups [5],[6] and our data does indeed approach $I_{dep} = 0.1I_c$ as $\lambda_\perp \gg 1$.

Phillips et al. have shown that as $\lambda_\perp$ decreases the stored magnetic energy, $E_m = (1/2\lambda_\perp) I_m^T L_m I_m$, must be included. Here, L_m is the dimensionless mesh inductance matrix and I_m, the mesh currents. For smaller $\lambda_\perp$, ΔE increases [8] and hence I_{dep} also increases.

The dashed line of Fig. 3 represents the depinning current associated with ΔE calculated for a single vortex in a 127×127 array taking into account both the Josephson energy and E_m. This static calculation asymptotically approaches the LAT value of $0.1I_c$.

Although the static calculation appears to fit to our measurements, it assumes that there is only one vortex in the system. Therefore to more closely approach our physical situation, we performed dynamical simulations that included all the mutual inductances [4] with $f = 0.2$ on an array of 15×15 and calculated $I-V$ curves. (The mutual inductance matrix is calculated numerically from

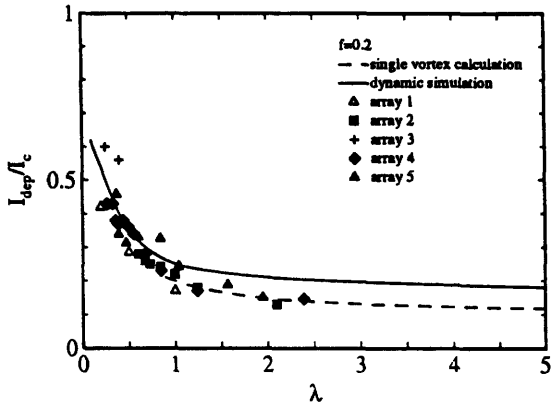

Fig. 3. Depinning current as a function $\lambda_\perp$.

the actual sample lay-out.) With such a high applied field many vortices are present so that both vortex interactions and edge effects are included in our dynamic simulations. We extracted the depinning current using the same experimental criteria outlined in Section II. The result is shown in the solid line of Fig. 3 that lies above the dashed line.

LAT showed that ΔE is inversely dependent on N. Since the dynamic simulation was made for a smaller array than the static calculation, one would expect the solid line of Fig. 3 to be lower than the dashed line. However, if the size of the array is small enough, depinning from the edge can affect the overall depinning current. This may account for the fact that I_{dep} is a third larger than the static calculation even at $\lambda_\perp = 5$. To verify if the edge effects could cause an increase in I_{dep}, a dynamic simulation was performed for $\lambda_\perp = 5$ for a 15×15 array and a 31×31 array. For the smaller array $I_{dep}/I_c = 0.17$ as seen in Fig. 3. For the larger array $I_{dep}/I_c = 0.13$. So that edge effects account for most of the increase in I_{dep} and are thus more pronounced than vortex interactions for arrays 15×15 or smaller at $f = 0.2$.

The measured data follows the same trend as the dynamic simulation except the values tend to be lower. This may be due to thermal noise introduced by the finite temperature. The simulations do not take thermal noise into account. Since these arrays have such large β_c's, thermal noise may easily cause vortices to depin at lower currents.

IV. Depinning current vs. frustration

In Fig. 4 we show measurements of the depinning current versus frustration for array 1 with various values of $\lambda_\perp$. The data was taken at temperatures of 4.2 K, 7.9 K and 8.6 K. By increasing the temperature the individual junction's critical current decreases and hence change $\lambda_\perp$ from 0.2, 0.5 to 1 respectively. We verified that the depinning current is symmetric about $f = 1/2$ and periodic with $f = 1$ as expected. The measured data has a large peak at $f = 0$ followed by a rapid decay to a saturation level. This saturation level contains a substructure when $\lambda_\perp > 0.2$ with clear peaks at $f = 1/2$, as well as some smaller peaks at $f = 1/4$ and $f = 1/3$. This substructure tends to be washed out as $\lambda_\perp$ decreases and disappears when $\lambda_\perp = 0.2$. Note also that the saturation level increases as $\lambda_\perp$ decreases.

For comparison a simulation taking into account all the mutual inductance interactions was performed for the same parameters of array 1. The trends are strikingly similar. The same substructure is seen and the saturation level increases as $\lambda_\perp$ becomes smaller although the levels are lower in the measured data. Similar trends are reported in recent numerical simulations in which the inductance matrix is calculated analytically [9].

We first focus on the $f = 0$ region of Fig. 4. For large $\lambda_\perp$ we expect the array to behave coherently as a single

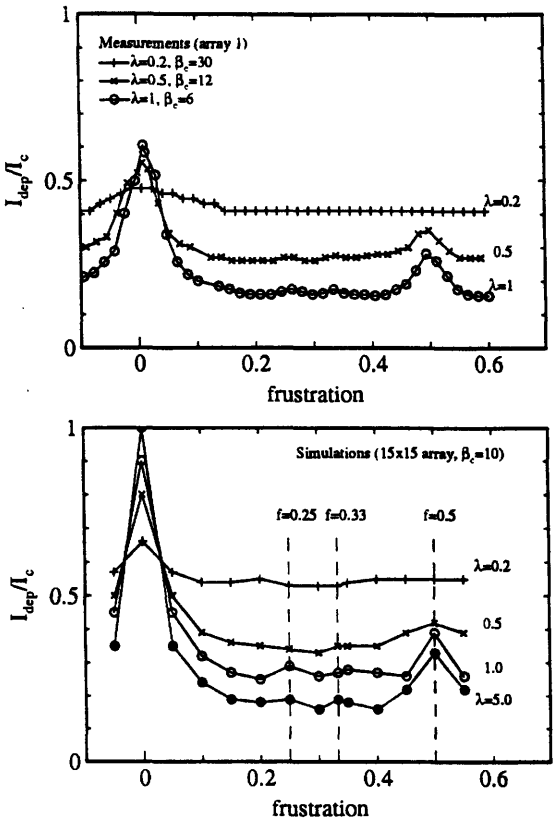

Fig. 4. Top: Measured depinning current as a function applied field. Bottom: Simulated depinning current as a function applied field.

junction with a critical current scaled by $(N + 1)$ and an R_n which is N times smaller. In this state every junction in the array is oscillating with the same frequency. So as expected, the superconducting region in the simulations extends to $I_{dep} = (N + 1)i_c$. It has been shown that the in-phase solution of the junctions is neutrally stable so that the junctions may not necessarily be in-phase [10]. However experimental measurements of the power emitted by junction arrays always indicate some degree of phase-locking. It is probable that an applied magnetic field, or the effects of $\lambda_\perp < N$ may provide a mechanism for weak phase locking in the array [11].

As $\lambda_\perp$ decreases more current begins to flow around the edges inducing a locally larger magnetic field. If the field is sufficiently strong it may produce pinned vortices near the edges. These pinned vortices can lower the depinning current from the $\lambda_\perp = \infty$ case. In both the simulations and the measurements we see the trend that the $f = 0$ peak decreases with decreasing $\lambda_\perp$. However, the measured levels are lower. This may be explained by two reasons. First a truly zero applied field state is very difficult to obtain experimentally and secondly thermal noise might depin the vortices prematurely.

The substructure is a result of a vortex superlattice

forming a commensurate state with the underlying geometry of the array. These occur at values of $f = p/q$, where p and q are small prime integers. For instance, at $f = 1/2$ it is known that the ground state for $\lambda_\perp = \infty$ is a checkered board pattern and that $I_{dep} = 0.41 I_c$ [5]. The large I_{dep} is a result of the depinning of the larger vortex ground state which requires more energy than the depinning of a single vortex. The peaks at those special values of f represent the formation of commensurate ground states which require higher energy to depin. As $\lambda_\perp$ decreases vortices become more screened and hence their interaction is diminished. It is likely that these ground state superlattices can no longer form and hence the substructures disappears.

V. Dynamic properties

In this section we will consider the flux-flow region shown in Fig. 2. Vortices in this region tend to flow in an incoherent way across the array and are most similar to the motion of vortices in thin films. For values of f that do not produce a commensurate ground state the flux-flow region is linear and hence it is possible to calculate a flux-flow resistance, R_{ff}.

With a Bardeen-Stephen-like model for flux flow, we can equate the viscous energy dissipated by a vortex moving between adjacent cells to the power dissipated in each island [6]. The resulting expression is $R_{ff} = 2fR_n$. This result is calculated for a steady-state motion of a vortex so that it is independent of β_c and does not include the effect of mutual inductances. However, we have observed a β_c and $\lambda_\perp$ dependence of R_{ff}; therefore we generalize to $R_{ff} = \alpha f R_n$ and now explain how α is dependent on β_c and $\lambda_\perp$.

When $\lambda_\perp = \infty$, we can model the effect of a finite β_c. At the singular value of $\beta_c = 0$ there is no equivalent mass and hence the vortex has a constant velocity. In this regime $\alpha = 2$ and we recover the Bardeen-Stephen-like result. It has been observed that a large β_c causes R_{ff} to become smaller [6]. This can be explained by an additional viscosity term caused by the coupling of the vortex to the spin-wave excitations of the array. Simulations [12] have shown that $\alpha = 2\pi/\sqrt{\beta_c}$ as $\beta_c \gg 1$.

We find that it is also possible to include the effect of mutual inductances on α. For strong mutual inductances, $\lambda_\perp < 1$, the extent of the vortex can sill be modeled by a radius of $\lambda_\perp$. As $\lambda_\perp$ becomes smaller the vortex becomes physically smaller. As it moves across the array it crosses less junctions and hence it dissipates less energy. This is equivalent to reducing the viscosity of the array. Since R_{ff} is inversely proportional to the viscosity, we expect R_{ff} to increase as $\lambda_\perp$ becomes smaller. We have observed this result in both the simulations and in experiments. However in the experiments $\lambda_\perp$ and β_c depend on temperature, and so cannot be varied independently.

VI. Conclusion

Strong self fields affect both the static properties and dynamic properties of a Josephson junction array. The cell-to-cell energy barrier of the array increases as $\lambda_\perp$ decreases and hence I_{dep} increases. We have also shown that R_{ff} is dependent on both $\lambda_\perp$ and β_c. The dependence on β_c follows from spin-wave damping while the $\lambda_\perp$ dependence is a result of a reduction of the viscosity caused by the decreasing physical size of traveling vortices as $\lambda_\perp$ decreases. Practical arrays for high-J_c niobium tunnel-junctions operate with $\lambda_\perp \sim 1$ where the self-field effects greatly influence the device performance and modeling. Further research is underway to explore the effects of self-fields on the full range of dynamics in these arrays.

Acknowledgment

We thank Shinya Watanabe, Mauricio Barahona, Steven Strogatz and Amy Duwel for useful discussions.

References

[1] S. P. Benz, C. J. Burroughs, "Coherent emission from two-dimensional Josephson junction arrays," *Appl. Phys. Lett.*, vol. 58, pp. 2162-2164, May 1991.

[2] J. R. Phillips, H. S. J. van der Zant, J. White and T. P. Orlando, "Influence of induced magnetic fields on Shapiro steps in Josephson junction arrays," *Phys. Rev. B*, vol. 50, October 1994.

[3] D. Domínguez and J. V. José, "Giant Shapiro Steps with Screening Currents," *Phys. Rev. Lett.*, vol. 69, pp. 514-517, July 1992.

[4] J. R. Phillips, H. S. J. van der Zant, and T. P. Orlando, "Dynamics of row-switched states in Josephson-junction arrays," *Phys. Rev. B*, vol. 50, October 1994.

[5] M. S. Rzchowski, S. P. Benz, M. Tinkham, and C. J. Lobb, "Vortex pinning in Josephson-junction arrays," *Phys. Rev. B*, vol. 42, pp. 2041-2050, August 1990.

[6] H. S. J. van der Zant, F. C. Fritschy, T. P. Orlando, J. E. Mooij, "Vortex dynamics in two-dimensional underdamped, classical Josephson-junction arrays," *Phys. Rev. B*, vol. 47, pp. 295-304, January 1993.

[7] C. J. Lobb, David W. Abraham, and M. Tinkham, "Theoretical interpretation of resistive transition data from arrays of superconducting weak links," *Phys. Rev. B.*, vol. 27, pp. 150-157, January 1983.

[8] J. R. Phillips, H. S. J. van der Zant, and T. P. Orlando, "Influence of induced magnetic fields on the static properties of Josephson-junction arrays," *Phys. Rev. B*, vol. 47, pp. 5219-5229, March 1993.

[9] D. Reinel, W. Dieterich, and T. Wolf, "Flux-flow phenomena and current-voltage characteristics of Josephson-junction arrays with inductances," *Phys. Rev. B*, vol. 49, pp. 9118-9124, April 1994.

[10] K. Wiesenfeld, S. P. Benz and P. A. A. Booi, "Phase-locked oscillator optimation for arrays of Josephson junctions," preprint.

[11] S. Watanabe, M. Barahona, S. Strogatz, private communication, 1994.

[12] U. Geigenmüller, C. J. Lobb, and C. B. Whan, "Friction and inertia of a vortex in an underdamped Josephson array," *Phys. Rev. B*, vol. 47, pp. 348-358, January 1993.

Bibliography

[1] V. Ambagaokar and A. Baratoff. Tunneling between superconductors. *Phys. Rev Lett.*, 10:486–489, 1963.

[2] S.P. Benz and C.J. Burroughs. Coherent emission from two-dimensional Josephson junction arrays. *Appl. Phys. Lett.*, 58:2162–2164, 1991.

[3] M. Bhushan and E.M. Macedo. $Nb/AlO_x/Nb$ trilayer process for the fabrication of submicron Josephson junctions and low-noise de squids. *Appl. Phys. Lett.*, 58:1323, 1991.

[4] William L. Briggs. *A multigrid tutorial.* Society for Industrial and Applied Mathematics, Philadelphia, 1987.

[5] J.S. Chung, K.H. Lee, and D. Stroud. Dynamical properties of superconducting arrays. *Phys. Rev. B*, 40:6570–6580, 1989.

[6] C.A. Desoer and E.S. Kuh. *Basic circuit theory.* McGraw-Hill, New York, 1969.

[7] Daniel Domínguez and Jorge V. José. Giant Shapiro steps with screening currents. *Phys. Rev Lett.*, 69:514–517, 1992.

[8] Daniel Domínguez and Jorge V. José. Non-equilibrium coherent vortex states and subharmonic giant Shapiro steps in Josephson-junction arrays. *Mod. Phys. B*, 8:3749–3793, 1994.

[9] Ulrich Eckern and Albert Schmid. Quantum vortex dynamics in granular superconducting films. *Phys. Rev. B*, 39:6441–6454, 1989.

[10] Ulrich Eckern and Edouard B. Sonin. Vortex mass and viscosity in Josephson-junction arrays. *Phys. Rev. B*, 47:505–508, 1993.

[11] F. Falo, A.R. Bishop, and P.S. Lomdahl. I-V characteristics in two-dimensional frustrated Josephson-junction arrays. *Phys. Rev. B*, 41:10983–10993, 1990.

[12] P. Hadley, M.R. Beasley, and K. Wiesenfeld. Phase locking of Josephson-junction series arrays. *Phys. Rev. B*, 38:8712–8719, 1988.

[13] T.J. Hagenaars, P.H.E. Tiesinga, J.E. van Himbergen, and Jorge V. Jose. Non-linear viscous vortex motion in two-dimensional Josephson junction arrays. *Phys. Rev. B*, 50:1143, 1994.

[14] Thomas C. Halsey. Josephson-junction arrays in transverse magnetic fields: ground states and critical currents. *Phys. Rev. B*, 31:5728–5745, 1985.

[15] J. Binslev Hansen and P.E. Lindelof. Static and dynamic interactions between josephson junctions. *Rev. Mod. Phys.*, 56:431, 1984.

[16] Inc. Hypres. Elmsfort, ny 10523.

[17] H.D. Jallen, R. Seshadri, A.M. Chang, R.E. Miller, L.N. Pfeiffer, K.W. West, C.A. Murray, and H.F. Hess. Direct spatial imaging of vortices in a superconducting wire network. *Phys. Rev Lett.*, 71:3007–3010, 1993.

[18] M.B. Ketchen et al. Sub-μm, planarized, Nb-Al_2O_x-Nb Josephson process for 125 mm wafers developed in partnership with Si technology. *Appl. Phys. Lett.*, 59:2609–2611, 1991.

[19] S.G. Lachenmann, T. Doderer, D. Hoffmann, R.P. Huebener, P.A.A. Booi, and S.P. Benz. Observation of vortex dynamics in two-dimensional Josephson-junction arrays. *Phys. Rev. B*, 50:3158–3164, 1994.

[20] C.J. Lobb, David W. Abraham, and M. Tinkham. Theoretical interpretation of resistive transition data from arrays of superconducting weak links. *Phys. Rev. B*, 27:150–157, 1983.

[21] K. Nakajima and Y. Sawada. Numerical analysis of vortex motion in two-dimensional array of Josephson junctions. *J. Appl. Phys.*, 52:5732–5743, 1981.

[22] T.P. Orlando and K.A. Delin. *Foundations of Applied Superconductivity.* Addison-Wesley, 1991.

[23] T.P. Orlando, J.E. Mooij, and H.S.J. van der Zant. Phenomenological model of vortex dynamics in arrays of Josephson junctions. *Phys. Rev. B*, 43:10218–10228, 1991.

[24] J. Pearl. *Vortex theory of superconductive memories.* PhD thesis, Polytechnic Institute of Brooklyn, 1965.

[25] J.R. Phillips, H.S.J. van der Zant, and T.P. Orlando. Influence of induced magnetic fields on the static properties of Josephson-junction arrays. *Phys. Rev. B*, 47:5219–5229, 1993.

[26] J.R. Phillips, H.S.J. van der Zant, and T.P. Orlando. Dynamics of row-switched states in Josephson-junction arrays. *Phys. Rev. B*, 50:9380–9386, 1994.

[27] J.R. Phillips, H.S.J. van der Zant, J. White, and T.P. Orlando. Influence of induced magnetic fields on Shapiro steps in Josephson junction arrays. *Phys. Rev. B*, 50:9387–9396, 1994.

[28] D. Reinel, W. Dieterich, T. Wolf, and A. Majhofer. Flux-flow phenomena and current-voltage characteristics of Josephson-junction arrays with inductances. *Phys. Rev. B*, 49:9118–9124, 1994.

[29] A.E. Ruehli. Inductance calculations in a complex integrated circuit environment. *IBM J. Res. Develop.*, 16:470–481, 1972.

[30] M.S. Rzchowski, S.P. Benz, M. Tinkham, and C.J. Lobb. Vortex pinning in Josephson-junction arrays. *Phys. Rev. B*, 42:2041–2050, 1990.

[31] S. Teitel and C. Jayaprakash. Josephson-junction arrays in transverse magnetic fields. *Phys. Rev Lett.*, 51:1999–2002, 1983.

[32] S. Teitel and C. Jayaprakash. Phase transitions in frustrated two-dimensional XY models. *Phys. Rev. B*, 27:598–601, 1983.

[33] Inc. The Math Works. Natick, ma 01760.

[34] T. S. Tighe, A. T. Johnson, and M. Tinkham. Vortex motion in two-dimensional arrays of small, underdamped Josephson junctions. *Phys. Rev. B*, 44:10286–10290, 1991.

[35] U.Geigenmüller, C.J. Lobb, and C.B. Whan. Friction and inertia of a vortex in an underdamped Josephson array. *Phys. Rev. B*, 47:348–358, 1993.

[36] H.S.J. van der Zant, F.C. Fritschy, T.P. Orlando, and J.E. Mooij. Ballistic vortices in Josephson-junction arrays. *Europhys. Lett.*, 18:343–348, 1992.

[37] H.S.J. van der Zant, F.C. Fritschy, T.P. Orlando, and J.E. Mooij. Vortex dynamics in two-dimensional underdamped, classical Josephson-junction arrays. *Phys. Rev. B*, 47:295–304, 1993.

[38] H.S.J. van der Zant, C.J. Muller, L.J. Geerligs, C.J.P.M. Harmans, and J.E. Mooij. Cohernet phase slip in arrays of underdamped Josephson tunnel junctions. *Phys. Rev. B*, 38:5154, 1988.

[39] H.S.J. van der Zant, R.A.M. Receveur, T.P. Orlando, and A.W. Kleinsasser. One-dimensional parallel Josephson-junction arrays as a tool for diagnostics. *Appl. Phys. Lett.*, 65:2102–2104, 1994.

[40] K. Wiesenfeld, S.P. Benz, and P.A.A. Booi. Phase-locked oscillator optimization for arrays of Josephson junctions. *J. Appl. Phys.*, 76:3835–3846, 1994.

[41] Wenbin Yu and D. Stroud. Resistance steps in underdamped Josephson-junction arrays. *Phys. Rev. B*, 46:14005–14009, 1992.